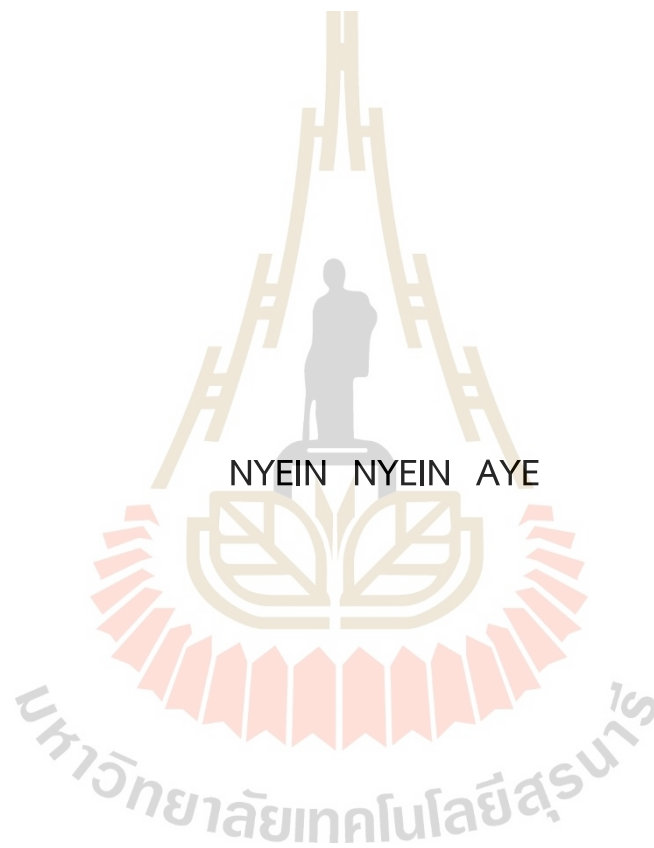


NUMERICAL STUDY OF PRINTED CIRCUIT HEAT EXCHANGER
(PCHE) APPLYING IN CRYOGENIC APPLICATION



A Thesis Submitted in Partial Fulfillment of the Requirements for the
Degree of Doctor of Philosophy in Mechanical
and Process System Engineering
Suranaree University of Technology
Academic Year 2023

การศึกษาเชิงตัวเลขของเครื่องแลกเปลี่ยนความร้อนแบบวงจรมัด (PCHE)
ประยุกต์ใช้กับงาน CRYOGENIC



วิทยานิพนธ์นี้เป็นส่วนหนึ่งของการศึกษาตามหลักสูตรปริญญาวิศวกรรมศาสตรดุษฎีบัณฑิต
สาขาวิชาวิศวกรรมเครื่องกลและระบบกระบวนการ
มหาวิทยาลัยเทคโนโลยีสุรนารี
ปีการศึกษา 2566

NUMERICAL STUDY OF PRINTED CIRCUIT HEAT EXCHANGER (PCHE)
APPLYING IN CRYOGENIC APPLICATION

Suranaree University of Technology has approved this thesis submitted in partial fulfillment of the requirements for the Degree of Doctor of Philosophy.

Thesis Examining Committee



.....
(Assoc. Prof. Dr. Bundit Krittacom)

Chairperson



.....
(Asst. Prof. Dr. Chalothorn Thumthae)

Member (Thesis Advisor)



.....
(Assoc. Prof. Dr. Veena Phunpeng)

Member



.....
(Asst. Prof. Dr. Teetut Dolwichai)

Member



.....
(Asst. Prof. Dr. Withun Hemsuwan)

Member



.....
(Assoc. Prof. Dr. Yupaporn Ruksakulpiwat)

Vice Rector for Academic Affairs

and Quality Assurance



.....
(Assoc. Prof. Dr. Pornsiri Jongkol)

Dean of Institute of Engineering

นีย์ นีย์ อาย : การศึกษาเชิงตัวเลขของเครื่องแลกเปลี่ยนความร้อนแบบวงจรมีพิมพ์ (PCHE) ประยุกต์ใช้กับงาน CRYOGENIC (NUMERICAL STUDY OF PRINTED CIRCUIT HEAT EXCHANGER (PCHE) APPLYING IN CRYOGENIC APPLICATION)
อาจารย์ที่ปรึกษา : ผู้ช่วยศาสตราจารย์ ดร.ชโลธร ธรรมแท้, 146 หน้า.

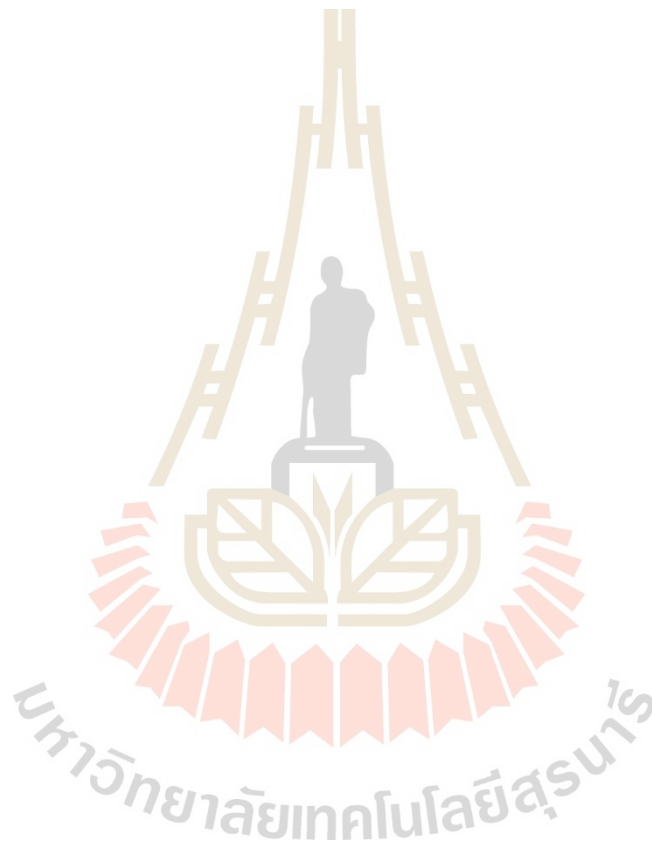
คำสำคัญ: เครื่องแลกเปลี่ยนความร้อนแบบวงจรมีพิมพ์/ช่องการไหลขนาดเล็ก/ของไหลเย็นยิ่งยวด/
การทำให้ช่องการไหลซิกแซกเหมาะสมที่สุด/การระเหย.

เครื่องแลกเปลี่ยนความร้อนวงจรมีพิมพ์ (PCHE) ได้รับการยอมรับในด้านประสิทธิภาพ ความกะทัดรัด ความน่าเชื่อถือ ความสามารถในการจัดการของไหลเย็นยิ่งยวด (cryogenic fluids) โดยเฉพาะในงานสำคัญอย่างการเปลี่ยนก๊าซธรรมชาติเหลว (LNG) ให้กลับมาเป็นสถานะก๊าซ การศึกษานี้ ใช้พลศาสตร์ของไหลเชิงคำนวณ (CFD) เพื่อวิเคราะห์และประเมินสมรรถนะของ PCHE

วัตถุประสงค์แรกคือ การประเมินสมรรถนะของ PCHE แบบช่องการไหลซิกแซก การวิเคราะห์ เน้นทั้งสมรรถนะการไหลและความร้อนภายใต้สภาวะการไหลคงตัว ตรวจสอบตัวแปร ประสิทธิภาพ (effectiveness) สัมประสิทธิ์การถ่ายเทความร้อน (heat transfer coefficients) และการสูญเสีย ความดัน ผลลัพธ์จากการเปลี่ยนมุมการดัด (bending angle) แสดงให้เห็นถึงสมรรถนะของช่อง การไหลซิกแซกเปลี่ยนแปลงอย่างสำคัญเมื่อมุมการดัดถึงค่าวิกฤตค่าหนึ่ง เพื่อเข้าใจถึงปรากฏการณ์ นี้ดีขึ้น จึงได้นิยามตัวแปรไร้มิติตัวเลขการดัด (Bending number : β) ซึ่งนิยามด้วยอัตราส่วน ระหว่างความกว้างของช่องการไหลต่อความโตของการดัดโค้งของช่องการไหล ผลลัพธ์จากการแปรผันค่ามุมและขนาดของช่องการไหลแสดงให้เห็นถึง ค่าอัตราส่วนระหว่าง ตัวเลขนัสเซลท์ (Nusselt number) ต่อสัมประสิทธิ์ความเสียดทาน (Nu/f) มีค่าสูงสุดที่ค่าตัวเลขการดัด β ประมาณ 0.5 จึงได้พัฒนาสมการความสัมพันธ์สำหรับ ตัวเลขนัสเซลท์ สัมประสิทธิ์ความเสียดทาน ต่อ มุมการดัด และ ตัวเลขการดัด

วัตถุประสงค์ที่สองคือการประเมินตัวแปรที่เกี่ยวข้องกับการระเหยใน PCHE แบบช่องการไหลขนาดเล็ก ตรวจสอบการถ่ายเทความร้อนว่าส่งผลอย่างไรต่อคุณลักษณะการระเหยของก๊าซมีเทน ในสภาวะเย็นยิ่งยวด การใช้ CFD ร่วมกับการจำลองการไหลด้วย volume of fluid (VOF) สามารถประเมินการทั้งการเดือดแบบพาความร้อน (convective boiling) และ การเดือดนิวเคลียต (nucleate boiling) ศึกษาผลกระทบของความดันของไหล อุณหภูมิทางเข้า และเส้นผ่านศูนย์กลางของช่องการไหลต่อการเพิ่มความสามารถของการระเหย ผลลัพธ์แสดงให้เห็นว่าอัตราการระเหยเพิ่มขึ้นตามความดันของเหลวที่ลดลง อุณหภูมิขาเข้าที่ลดลง และเส้นผ่านศูนย์กลางของช่องการไหลที่ใหญ่ขึ้น ได้ออกแบบเครื่องแลกเปลี่ยนความร้อนแบบช่องการไหลซิกแซกชิ้นใหม่ บนพื้นฐานของการวิจัยก่อนหน้าซึ่งให้การระเหยที่มากขึ้น จากการปั่นป่วน การผสม และการถ่ายเทความร้อนที่สูงขึ้น

งานวิจัยนี้ให้ข้อมูลเชิงลึกที่มีคุณค่าเกี่ยวกับสมรรถนะทางการไหลและความร้อน ของเครื่องแลกเปลี่ยนความร้อน PCHE ชนิดช่องการไหลเล็ก (MHXs) ซึ่งใช้ในงานของไหลเย็นยิ่งยวด ผลลัพธ์จากการวิจัยนี้สามารถใช้เป็นแนวทางในการออกแบบเครื่องแลกเปลี่ยนความร้อนสำหรับการเปลี่ยนก๊าซธรรมชาติเหลว (LNG) ให้กลับมาเป็นสถานะก๊าซ



สาขาวิชา วิศวกรรมเครื่องกล

ปีการศึกษา 2566

ลายมือชื่อนักศึกษา.....*ujin*.....

ลายมือชื่ออาจารย์ที่ปรึกษา.....*[Signature]*.....

NYEIN NYEIN AYE : NUMERICAL STUDY OF PRINTED CIRCUIT HEAT EXCHANGER (PCHE) APPLYING IN CRYOGENIC APPLICATION.

THESIS ADVISOR : ASST. PROF. CHALOTHORN THUMTHAE, Ph.D., 146 PP.

Keywords: Printed circuit heat exchanger/Minichannels/Cryogenic fluids/Zigzag channel optimization/ Evaporation.

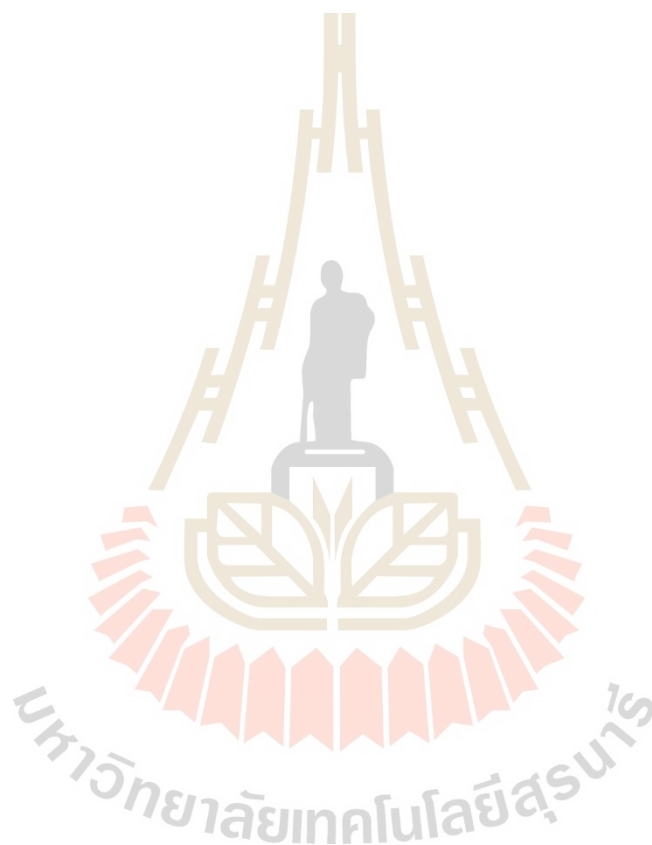
Printed Circuit Heat Exchangers (PCHEs) are prized for their efficiency, compactness, and reliability, especially in critical applications like LNG regasification and cryogenic fluid handling. This study employed Computational Fluid Dynamics (CFD) to analyze and evaluate the performance of PCHEs.

The first objective was to assess the performance of zigzag PCHEs, focusing on both thermal and hydraulic performance under steady-state conditions. Key parameters such as effectiveness, heat transfer coefficients, and pressure drop were examined. The analysis revealed that the performance of the zigzag channel varies significantly when the bending angle reaches a critical value. To better understand this phenomenon, a dimensionless parameter, the Bending Number (β) defined as the ratio of channel width to bending amplitude was introduced. Results indicated that the ratio of the Nusselt number to the friction factor (Nu/f) is maximized at bending numbers around 0.5. New correlations for the Nusselt number and friction factor were developed based on bending angles and Bending Numbers.

The second objective was to evaluate evaporation parameters in minichannel PCHEs. The study investigated how heat transfer affects the evaporation characteristics of cryogenic methane. Using CFD with volume of fluid (VOF) simulation, both convective and nucleate boiling were predicted. The study explored the effects of fluid pressure, inlet temperature, and channel diameter on evaporation enhancement. Results showed that the evaporation rate increases with decreasing fluid pressure, decreasing inlet temperature, and increasing channel diameter. Additionally, new zigzag channel designs, based on previous research, were proposed to enhance evaporation due to their higher turbulence, mixing, and heat transfer rates.

This research provides valuable insights into the thermal-hydraulic performance of PCHEs as mini heat exchangers (MHXs) in cryogenic applications, facilitating improved

predictions of both steady-state and transient performance for zigzag and straight channel designs.



School of Mechanical Engineering

Academic Year 2023

Student's Signature

Advisor's Signature

ACKNOWLEDGEMENT

The author would like to thank Suranaree University of Technology for their financial support of this study.

The author is sincerely grateful to her academic supervisor, Assistant Professor Dr. Chalothorn Thumthae, for his invaluable supervision, patient guidance, and enthusiastic encouragement throughout this research. His mentorship has not only helped me develop logical thinking and research skills but has also provided essential insights into my thesis work.

The author extends sincere gratitude to the committee members for their insightful comments and assistance. Additionally, heartfelt thanks are expressed to all the instructors and staff at Suranaree University of Technology for their support and guidance throughout the research process.

Finally, the author would like to express heartfelt gratitude to her family and her beloved Mr. Myat Thu Maung. She extends her deepest thanks for their unwavering encouragement, support, and love throughout this journey.

Nyein Nyein Aye

มหาวิทยาลัยเทคโนโลยีสุรนารี

TABLE OF CONTENTS

	Page
ABSTRACT (THAI).....	I
ABSTRACT (ENGLISH).....	III
ACKNOWLEDGEMENT.....	V
TABLE OF CONTENTS.....	VI
LIST OF TABLES.....	XI
LIST OF FIGURES.....	XII
LIST OF ABBREVIATIONS.....	XVII
CHAPTER	
I INTRODUCTION.....	1
1.1 Background and Motivation.....	1
1.2 Research Objective.....	3
1.3 Scope of this Study.....	3
1.4 Expected Outcomes.....	4
II LITERATURE REVIEWS.....	5
2.1 Review on Printed Circuit Heat Exchanger (PCHE).....	5
2.1.1 Compactness and Selection of Minichannels PCHE.....	7
2.2 Applications of Printed Circuit Heat Exchangers in Cryogenic Fluid Handling.....	8
2.2.1 Cryogenic Fluids.....	8
2.2.2 PCHE technology and its application in cryogenic environments.....	10
2.3 Effects of Geometric and Operational Parameters on Minichannels PCHE Thermal Hydraulic Performanc.....	12
2.3.1 Effects of Bending-Angle on Thermal Hydraulic Performance of Zigzag Channels PCHEs.....	13

TABLE OF CONTENTS (Continued)

	Page
2.3.2 Effects of Various Geometric Parameters on Thermal Hydraulic Performance of PCHEs	15
2.3.3 Operational Parameters of Zigzag PCHEs.....	17
2.4 A Review on Phases Transition Process in Minichannels of PCHEs	18
2.5 An Overview of the Literature Review	20
III RESEARCH METHODOLOGY AND NUMERICAL MODEL VALIDATION.....	24
3.1 Geometrical Configurations and Boundary Condition of the Zigzag Channel.....	24
3.2 Equations Governing Flow and Heat Transfer in Zigzag Channel Simulation	26
3.3 PCHEs Performance Parameters.....	27
3.4 Mesh Convergence Study for Zigzag Channel PCHEs Analysis.....	30
3.5 Model Validation for Zigzag Channel PCHEs Analysis.....	31
3.5.1 Circular Channel Validation.....	32
3.5.2 Semicircular Channel Validation	33
3.5.3 Zigzag Channel Validation	34
3.6 Model Preparation and Boundary Conditions for PCHE Evaporation	35
3.7 Numerical Simulation Method of Multiphase Flows.....	36
3.7.1 Mass Source Term.....	39
3.7.2 Heat Source Term.....	41
3.8 Mesh Grid Sensitivity Test for PCHE Evaporation Model.....	41
3.9 Numerical Model Verification for PCHE Evaporation Model.....	42
3.9.1 Steady State Condition	43
3.9.2 Transient State Condition.....	43
3.10 Case Study Simulation of Channel Structure Effects on Thermal Hydraulic Performance of PCHE	44
3.10.1 Setting up Numerical Models and Simulation Method.....	45

TABLE OF CONTENTS (Continued)

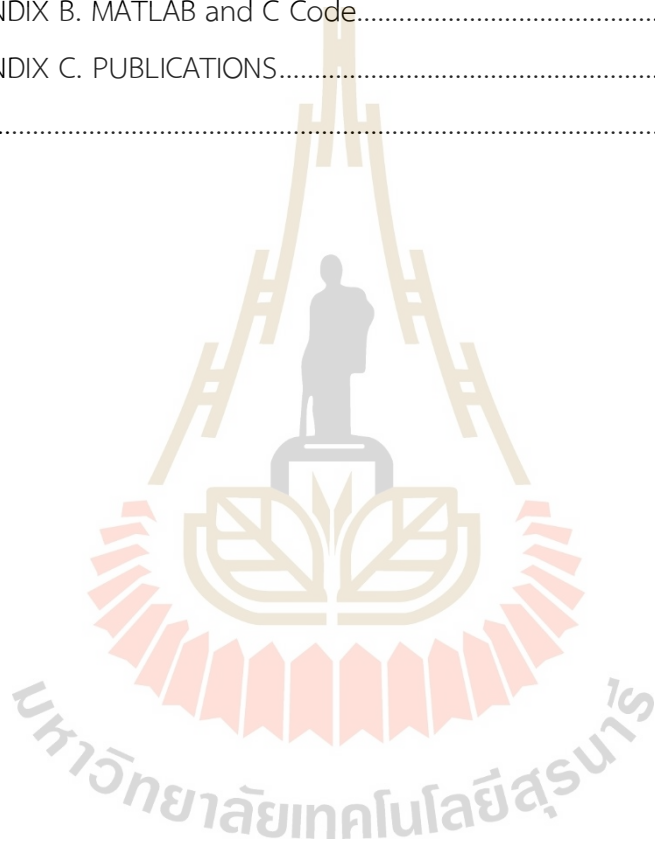
	Page
3.10.2 Grid Independence and Model Validation.....	46
3.10.3 Relation Between Channel Structure and Thermo-Physical Properties.....	47
3.10.4 Mass Flow Rate Effect on the Channels.....	51
3.10.5 Mass Flow Rate Effect on the Channels Effect of Zigzag Channel Diameter on The PCHE Performance	54
3.10.6 Comparison Between Present Study and Other Research of 15° Bending Zigzag Channel	55
3.10.7 Challenges in Geometry Optimization from Case Study of Channel Structure Analysis	56
3.11 Case Study Simulation of Evaporation Effect on Heat Transfer Characteristics and Mass Transfer Multiphase Flow Channels.....	56
3.11.1 Numerical Methodology and Mesh Convergence Study	57
3.11.2 Model Validation.....	58
3.11.3 Analysis of Evaporation Process Within Multiphase Flow Channel.....	59
3.11.4 Summary of Evaporation Process Within Multiphase Flow Channel.....	60
IV OPTIMIZING THE ZIGZAG CHANNEL DESIGN CONFIGURATIONS WITHIN PRINTED CIRCUIT HEAT EXCHANGERS (PCHES).....	61
4.1 Analysis of The Thermal Hydraulic Characteristics of the Different Zigzag Bending Angles.....	61
4.2 Correlation Analysis for Friction Factor and Nusselt Number in Optimal Angle Zigzag Channel PCHes.....	66
4.3 Effect of Channel Bending Angles on Local Internal Flow and Heat Transfer Characteristics.....	68

TABLE OF CONTENTS (Continued)

	Page
4.4 Analysis The Effect of Geometric Parameters and Compare with Other Correlation Results.....	72
4.5 Overview of The Bending Number Effect on PCHE in Zigzag Channels..	74
4.6 Impact of Bending Number Variations on Flow and Heat Transfer Distribution.....	78
4.7 Analysis of Local Performance with Different Bending Number	84
4.8 Development of Nusselt Number and Friction Factor Correlation	86
4.8.1 Development of Nusselt Number Correlation.....	87
4.8.2 Development of Friction Factor Correlation.....	91
4.8.3 Verification of Correlations for Friction Factor and Nusselt Number..	93
V EVAPORATION PARAMTERS IN PTINTED CIRCUIT HEAT EXCHANGERS (PCHEs) FOR CROYGENIC FLUID APLPLICATION.....	96
5.1 Cross-Sectional Local Analysis of Two-Phase Flow in Printed Circuit Heat Exchangers During Cryogenic Fluid Evaporation	96
5.2 The Effect of Inlet Temperature and Pressure on Cryogenic Fluid Evaporation in Minichannels	99
5.2.1 Analysis of Evaporation Temperature Distribution in Minichannels	100
5.2.2 Analysis of Evaporation Pressure Distribution in Minichannels	100
5.2.3 Evaporation Flow and Heat Transfer Mechanisms in Minichannel.....	102
5.3 Effect of Channel Diameter on Evaporation	106
5.4 Effect of Channel Shaper on Evaporation.....	108
VI CONCLUSION AND RECOMMENDATION.....	112
6.1 Conclusion.....	112
6.2 Recommendation	113

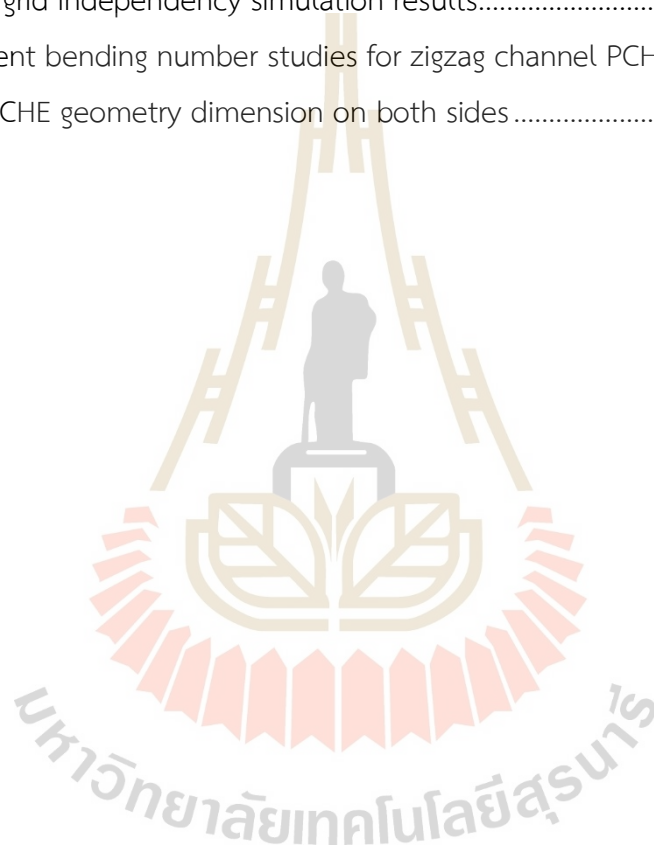
TABLE OF CONTENTS (Continued)

	Page
REFERENCES	114
APPENDICES	
APPENDIX A. VALIDATION EXPERIMENT INFORMATION.....	126
APPENDIX B. MATLAB and C Code.....	132
APPENDIX C. PUBLICATIONS.....	144
BIOGRAPHY	146



LIST OF TABLES

Table	Page
2.1	Chemical composition of natural gas9
3.1	Mesh grid independency simulation results..... 46
4.1	Different bending number studies for zigzag channel PCHEs..... 76
4.2	The PCHE geometry dimension on both sides 77



LIST OF FIGURES

Figure	Page
2.1	Capabilities of Pressure and Temperature.....5
2.2	Structure of printed circuit heat exchangers.....6
2.3	The area densities of a range of compact heat exchangers.....7
2.4	The test schematic of liquefied gas vaporization process 11
2.5	Different kinds of PCHE flow channels..... 13
2.6	Structural parameters of a zigzag channel 15
3.1	Physical model of the zigzag channel PCHE with counter flow arrangement..... 25
3.2	Mesh independency study..... 30
3.3	Mesh generation (3.678 million) of the computational domain 31
3.4	A simple flow analysis for a straight circular channel PCHE 32
3.5	Analysis for a straight semicircular channel PCHE..... 33
3.6	Comparison of global Nusselt number 34
3.7	Comparison of global pressure loss factors 35
3.8	A single-channel PCHE geometry and boundary conditions 36
3.9	A cross-sectional view of the channel's polyhedral mesh for the PCHE model..... 39
3.10	Shows the grid sensitivity test for CFD simulation convergence 41
3.11	Comparison between experimental and simulation results under steady state condition (hot side)..... 43
3.12	Comparison between experimental and simulation results under transient condition (cold side)..... 44
3.13	(a) 3D models of zigzag and straight channels. (b) Cross-sectional view of simulation domain..... 45

LIST OF FIGURES (Continued)

Figure	Page
3.14 Global Fanning friction factor (f) comparison, and global Nusselt number (Nu) comparison	47
3.15 Velocity distribution of straight and zigzag channels at pitch number ($N = 8$).....	48
3.16 Temperature distribution of straight and zigzag channels at pitch number ($N = 8$).....	49
3.17 Streamlines distribution at a pitch number ($N = 8$) (a) straight and (b) zigzag channel	49
3.18 (a) Local pressure drop and (b) local Nusselt number along flow direction..	49
3.19 Local convective heat transfer coefficient along the flow direction	50
3.20 Local heat transfer coefficient of the zigzag channel and straight channel ...	51
3.21 (a) Total global pressure drop, and (b) global Fanning friction factor at different mass flow rates for different channels.....	52
3.22 Velocity magnitude distribution for $Np = 8$ at different mass flow rates.....	52
3.23 (a) Global Nusselt number and (b) comprehensive performance evaluation index (ζ) at different mass flow rates for zigzag and horizontal channels.....	54
3.24 Effects of channel diameter analysis (a) Global Nusselt number (Nu) and Fanning friction factor (f), and (b) comprehensive performance evaluation index (ζ) at different channel diameter (D).....	54
3.25 Comparison of present CFD and Kim's correlation results.....	56
3.26 Geometry and boundary condition.....	57
3.27 Mesh convergence study at 1sec	58
3.28 Comparing the results of the relationship between heat transfer coefficient and velocity of the present work, H.I. Mohammed et al.'s	58
3.29 Velocity distribution of section $Z=980$ mm.....	59
3.30 Vapor distribution of section $Z=980$ mm.....	59

LIST OF FIGURES (Continued)

Figure	Page
3.31	Temperature distribution of section Z=980 mm..... 60
4.1	Effect of the channel zigzag angles on Nusselt number (Nu)..... 61
4.2	Effect of the channel zigzag angles on pressure loss factors (f)..... 62
4.3	Effect of the channel zigzag angles on Euler number (Eu)..... 63
4.4	Compare the effectiveness of various zigzag angles on cold side 63
4.5	Compared the performance evaluation criteria (Nu/Eu) of various zigzag angles on cold side..... 65
4.6	f correlation comparison for CFD cases 67
4.7	Nu correlation comparison for CFD cases..... 68
4.8	Local pressure drop in different bending channels..... 68
4.9	Velocity distribution in different bending channels..... 70
4.10	Distribution of streamwise velocity magnitudes at 3rd corner cross-sections..... 71
4.11	Temperature distribution at 3rd corner cross sections 71
4.12	The velocity vectors at 3rd corner cross sections 72
4.13	Analysis the general geometric parameters of a zigzag channel..... 73
4.14	Results based on channel curvature length (L_R) at $Re=1500$ 74
4.15	Common structural parameters of a zigzag channel 75
4.16	Schematic of PCHE geometry, (a) the zigzag channel unit, (b) the cross-section unit, and (c) the pitch of the zigzag channel with the inserted curvature at the corners..... 77
4.17	Bending number at various bending angles and channel sizes 78
4.18	Nusselt number at various bending number (cold side)..... 78
4.19	Nusselt number at various bending number (hot side)..... 79
4.20	Friction factor at various bending number (cold side)..... 80
4.21	Friction factor at various bending number (hot side)..... 82
4.22	Nu/f at various bending number..... 83

LIST OF FIGURES (Continued)

Figure	Page
4.23	Distribution of Nu and f along the flow direction for various β 85
4.24	Distribution of friction factor along the flow direction for various diameters and bending angles..... 86
4.25	Distribution of Nu/f along the flow direction for various β 87
4.26	Correlation and CFD ($Nu-\beta$) data comparison (cold side)..... 88
4.27	Correlation and CFD ($Nu-\beta$) data comparison (hot side) 89
4.28	Friction factor comparison between correlations and CFD data 90
4.29	Correlation and CFD ($f-\beta$) data comparison (cold side) 91
4.30	Correlation and CFD ($f-\beta$) data comparison (hot side) 92
4.31	Friction factor comparison between correlations and CFD data 93
4.32	Comparison of Experimental Data and Correlations for f and Nu 94
5.1	Illustrates vapour-phase distribution at different cross-sectional views (a number of 0 represents the liquid phase, while a number of 1 corresponds to the fully vapor phase)..... 97
5.2	Behaviours velocity of a vapour phase pattern inside undergoing evaporation 98
5.3	Effect of inlet temperature and pressure on temperature distribution 99
5.4	Effect of inlet temperature and pressure on pressure distribution..... 101
5.5	Effect of inlet temperature and pressure on heat transfer distribution..... 102
5.6	Flow patterns behavior with corresponding vapor quality at different pressure..... 103
5.7	Vapor distribution of different inlet temperature and pressure 104
5.8	Impact of channel diameter on local evaporation heat transfer coefficient. 105
5.9	Impact of channel diameter on pressure distribution 105
5.10	Impact of channel diameter on vapor phase. 106

LIST OF FIGURES (Continued)

Figure	Page
5.11 Flow patterns behavior with corresponding vapor quality at different Channel diameter (a number of 0 represents the liquid phase, while a number of 1 corresponds to the fully vapor phase).	108
5.12 Impact of channel shape on evaporation heat transfer coefficient	109
5.13 Impact of channel shape on vapor phase.....	109
5.14 Different flow pattern in zigzag channel with corresponding vapor quality (a number of 0 represents the liquid phase, while a number of 1 corresponds to the fully vapor phase).....	110
A.1 NACA straight-channel test apparatus.....	127
A.2 Relation between $\log(100\lambda)$ and $\log Re$ where r/k = relative roughness, λ = resistance factor.....	127
A.3 Geometry of the straight semicircular channel (cold side) plate used in the PCHE design (all dimensions in inches).....	128
A.4 Geometry of the straight semicircular channel (hot side) plate used in the PCHE design, (all dimensions in inches).....	128
A.5 KAIST helium test loop.....	129
A.6 The angle of a zigzag channel in PCHE	129
A.7 Images of a section of a hot-side or cold-side plate.....	129
A.8 Layout of the high-temperature helium test facility.....	130
A.9 Design of the heat plates: (a) straight channel design for low pressure used on the hot side, and (b) 'N'-type design for high pressure used on the cold side.....	130
A.10 Diffusion bonded core and scanning electron microscopy image of the cross-section of the PCHE core.....	131
A.11 Schematic of the two-phase nitrogen experimental set-up.....	131

LIST OF ABBREVIATIONS

f_g	Global pressure loss factor
ρ	Fluid density
A_c	Cross-sectional area of the channel
\dot{m}	Mass flow rate
L	Fluid-flow actual length
ΔP_f	Total pressure loss
P_{inlet}	static pressures at the inlet
P_{outlet}	static pressures at the outlet
h_g	global heat-transfer coefficient
q''_g	averaged-surface heat flux
$T_{f,g}$	arithmetic mean temperature between the inlet and outlet temperature of each side
$T_{w,g}$	average of the four terminal temperatures
Nu	Nusselt number
k	fluid thermal conductivity
d_h	Hydraulic diameter
Eu	Euler number
v	mean velocity
ε	effectiveness
C_p	Specific heat capacity
D	Channel diameter
α_l	Volume fraction of the liquid phase
α_g	Volume fraction of the vapor phase
S	Mass transfer rates due to phase change
\vec{F}_σ	Volumetric surface tension force
\vec{u}	Velocity field
p	Pressure

LIST OF ABBREVIATIONS (Continued)

F	Gravitational force
σ	Interfacial surface tension between the phases symbols
ρ_l	Liquid density
ρ_g	Vapor density
k_l	Curvatures of the liquid
k_g	Curvatures of the vapor
T	Shared temperature field
E	Enthalpy
k_e	Effective thermal conductivity
\dot{Q}	Heat transfer rates occurring through the interface
E_l	Specific heat of liquid
E_g	Specific heat of vapor
T_{sat}	Saturation temperature
h_{lg}	Latent Heat
ζ	Comprehensive performance evaluation index
α	Zigzag bending angle
Pr	Prandtl number
Re	Reynolds number
L_R	Sub-channel length
L_z	Half of a pitch length
x	Wavy amplitude
P_L	Pitch length
y	Width of the zigzag channel at the corner
β	Bending number
r_b	Bend curvature radius
t	Thickness between two channe
w	Width between channel and side wal
x	Channel local sub-length
c	Cold side

LIST OF ABBREVIATIONS (Continued)

<i>h</i>	Hot side
<i>sat</i>	Saturation
PCHE	Printed circuit heat exchanger
CFD	Computational fluid dynamics
<i>Exp</i>	Experiment
LNG	Liquefied natural gas



CHAPTER I

INTRODUCTION

1.1 Background and Motivation

Natural gas, primarily composed of methane, which can exist as cryogenic fluids at extremely low temperatures, is employed in the energy sector and various industrial practices. It is also a promising renewable energy and cleaner-burning fossil fuel with high quality, which has occupied 24% of the world's total use of energy. According to International Energy Agency (IEA) forecast, the demand of global energy will grow about 30% until 2040 (Biro, 2021). The off-shore gas requires more than 25% of the total natural gas to supply as a gas source to the enormous global energy market for facing the problems of energy shortage and carbon emissions (Khan et al., 2014). Most of the remaining natural gas is supplied from the deep sea. The deep-sea natural gas is exploited by inshore natural gas liquefaction plants and offshore natural gas liquefaction plants. However, offshore natural gas liquefaction is more efficiently to exploit natural gas when the gas well is far from the land, Floating Production Storage and Offloading System (FPSO) make a promising candidate for NG treatment. In the FPSO, the compact heat exchanger plays an important role for the liquefaction and vaporization operations. Therefore, the development of compact heat exchanger performance is an important issue to promote the economic efficiency of the whole system. The printed circuit heat exchanger (PCHE) is well suited in the floating liquefied natural gas (FLNG) plants, a newly developed compact heat exchanger, the heat transfer area density is more than $2500 \text{ m}^2/\text{m}^3$, pressure capacity is up to 60 MPa and the minimum operating temperature is lower than -200°C (Cai et al., 2022; Wang et al., 2022).

The PCHEs are assembled by a large number of flat metal plates with minichannels, etched on the plates with photochemical machining process. The metal plates are stacked and bonded to create a high-integrity heat exchanger core by the use of diffusion bonding technique for the capability of very high pressure, very high

and very low temperature operating, install it with headers for flow distribution. To achieve high thermal performance of PCHE, various channels design has been investigated such as straight, wavy (zigzag), S-shape fined channel, and airfoil fined (Chen et al., 2015; Sarmiento et al., 2021; Wang et al., 2017). These minichannels enhanced the heat transfer because small channels increased the heat transfer coefficients. Therefore, innovative in channel design of PCHE is an attractive technology to increase the efficiency and power output of the heat exchanger system. As the PCHEs applications of working fluid conditions, there are single-phase flow and two-phase flow in minichannel (Ray & Das, 2020). The researchers reviewed the single phase flow in minichannel for high-heat-flux cooling techniques and suggested that the single-phase liquid systems have the large pressure penalties, still required the high pumping power for the achievement of high thermal performance (Ebadian & Lin, 2011). C. Huang, et. al also discussed the single phase flow and heat transfer in the various minichannel PCHEs for recent two decades. From their evaluation, the global perspective is deeply focused on heat transfer enhanced and reducing in pressure drop performances in the design process of PCHEs for the LNG application (Huang et al., 2019). In two phase minichannel system, the working fluid's temperature increased during boiling to achieve high heat dissipation rates. As compared to single phase, these systems achieve the desired cooling rates at lower pumping costs and more uniform surface temperatures. However, the main downside of boiling in microchannel involve the compressibility, flashing, choking, instabilities and oscillations in the flow. These drawbacks may provide the illusive prediction on early onset of critical heat flux and flow properties in minichannel (Kim & Mudawar, 2014). Therefore, further research is still needed enhancement techniques of innovative minichannel in PCHE to promote in enhancing heat transfer with low pressure drop penalty, and realize the minichannel boiling/evaporation fundamental to provide the accurate mapping flow regimes and surface features to make them more effective in convective boiling heat transfer and pressure drop for the critical heat flux in minichannels hydraulic diameters.

To enhance the performance of printed circuit heat exchangers (PCHEs), more effort is required. They still remain quite expensive. Therefore, in this research work, the heat transfer characteristics and pressure drop of PCHEs were numerically

investigated with supercritical and cryogenic working fluids to enhance thermal hydraulic performance in cryogenic applications.

1.2 Research objective

The thermal-hydraulic performance of a minichannels PCHE plays a crucial role in liquefaction and vaporization processes within the energy sector and diverse industrial applications, serving as a pivotal component in the secure treatment of cryogenic fluids. The main aims of this study are to numerically examine the pressure drop and heat transfer attributes of high-temperature and very low-temperature cryogenic fluid PCHEs, modeling both the steady-state of zigzag PCHEs and the transient behavior of straight channel PCHEs using developed heat exchanger models. The objectives are as follow.

(1) To investigate the effects of geometric parameters such as bend angle, and diameter on heat transfer and pressure drop under the steady-state of zigzag PCHEs.

(2) To develop empirical correlations for the thermal-hydraulic performance of zigzag channel PCHEs by analyzing geometric parameters and a specific Reynolds number range.

(3) To analyze the heat transfer mechanisms and performance metrics during the evaporation process, including vapor generation rate, heat transfer coefficient, and pressure drop under transient behavior of minichannels PCHEs.

1.3 Scope of this Study

(1) Based on numerical method, this study used computational fluid dynamics simulation to analyze the thermal hydraulic performance of a printed circuit heat exchanger.

(2) The 3D numerical model was based on single banking model (set up cold and hot plates alternate each other), not full minichannels heat exchanger (MHX) for investigation the effects of geometric parameters.

(3) The evaporation 3D model considered a liquid flow channel with heat source walls.

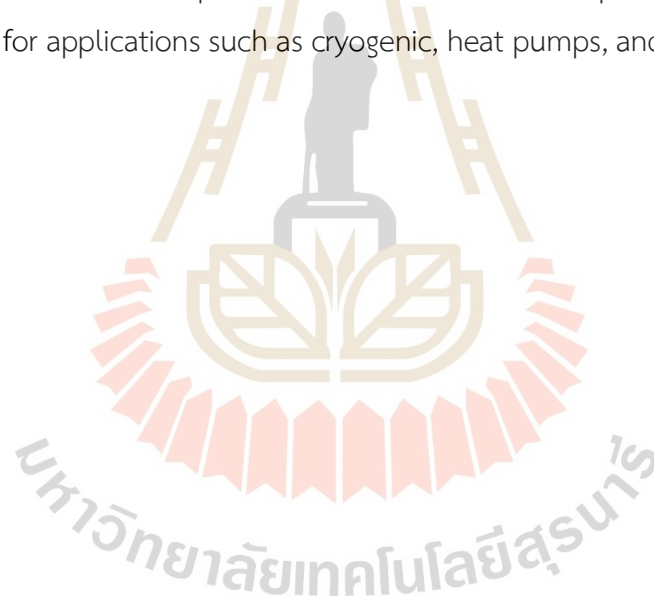
(4) The working fluid employed in this study included various states: single-phase (helium supercritical state) for optimizing zigzag channel parameters, and two-phase (cryogenic fluids: methane and nitrogen) for the evaporation process.

1.4 Expected Outcomes

(1) Investigation of zigzag channel geometric parameters can help identify the optimal combination of parameters for enhanced performance in PCHEs.

(2) The developed correlations can understand the PCHE behavior under specific flow conditions and provide valuable insights for optimizing PCHE design and performance in various industrial applications.

(3) Analysis of evaporation in a minichannels PCHEs can gain insights into the behavior of PCHEs under evaporation conditions and develop models to optimize their performance for applications such as cryogenic, heat pumps, and waste heat recovery.



CHAPTER II

LITERATURE REVIEWS

2.1 Review on Printed Circuit Heat Exchanger (PCHE)

Heatric had been manufactured compact heat exchangers types by diffusion bonding integrity, involving Hybrids Heat Exchangers, Formed Plate Heat Exchangers (FPHEs) and Printed Circuit Heat Exchangers (PCHEs) since 1985. In 1980, One of Heatric's researchers developed PCHEs which can operate in high pressure, high temperature, robustness with high compactness and efficiency than others. The capabilities of pressure and temperature range are shown in Figure 2.1. The formed of printed circuit heat exchangers are combination of etched plates, alternating layers hot to cold, cold to hot, etc. Typically, PCHEs have mini channels (cross-sectional semicircle shape) in Figure 2.2. By the alloy development, structural materials of PCHEs are generally used super alloys such as Alloy 800H, Alloy 625, Alloy 617 and stainless such as SS 316L, SS 316, SS 304, SS 904L.super alloys.

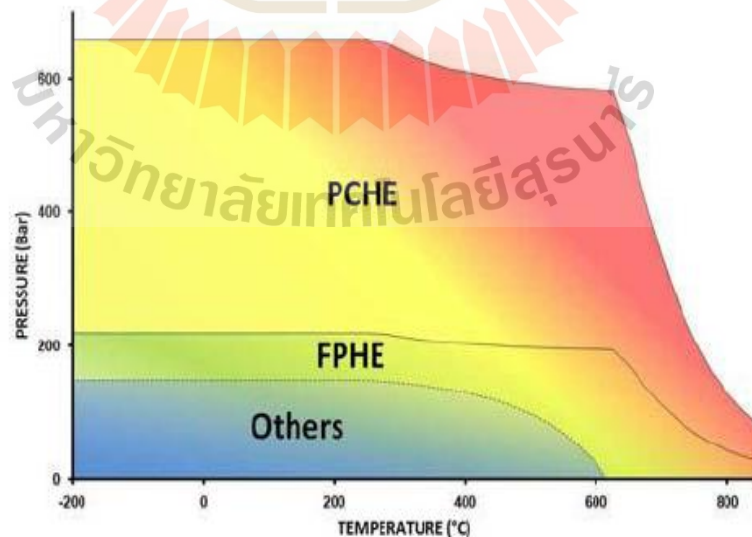


Figure 2.1 Capabilities of Pressure and Temperature (Southall & Dewson, 2010).

Advantages of PCHEs include their ability to achieve reduced weight, space, and supporting structure requirements due to their high heat transfer surface area per unit volume. They are significantly smaller and lighter, typically four to six times more compact compared to conventional shell-and-tube exchangers. This compactness leads to reduced energy requirements and costs, as well as lower fluid inventory. Additionally, PCHEs can achieve extremely high heat transfer coefficients, enhancing their efficiency in heat exchange processes. However, PCHEs also come with certain disadvantages. They tend to be expensive in terms of capital costs when compared to shell-and-tube units. Moreover, the fluid used in PCHEs needs to be exceptionally clean, as blockages can occur easily in the very small channels characteristic of PCHEs. Regular and careful cleaning of the filters is required to prevent blockages and maintain optimal performance.

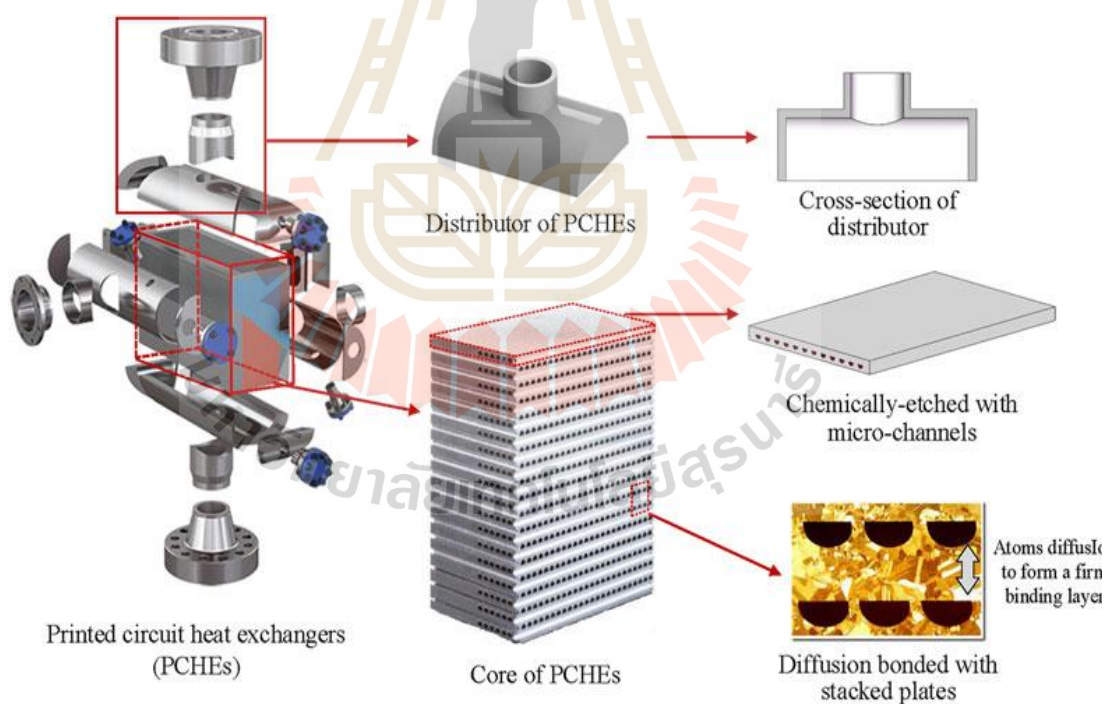


Figure 2.2 Structure of printed circuit heat exchangers (Xie et al., 2022).

2.1.1 Compactness and Selection of Minichannels PCHE

The compact heat exchangers and their classification criteria can be classified by surface area density that is indicative of the amount of heat transfer surface area per unit volume of the heat exchanger (m^2/m^3), reduce the weight, size, and cost. In accordance with the surface compactness of Shah's classification, surface area density of gas-to-fluid operation in heat exchanger is higher than in a liquid or phase-change stream heat exchanger. The density of surface area of printed circuit heat exchangers (PCHEs) is more than $700 \text{ m}^2/\text{m}^3$ in gas-to-fluid operations and more than $400 \text{ m}^2/\text{m}^3$ in liquid-to-liquid and phase change processes (Yoon et al., 2013). The hydraulic diameter d_h of mini channel is less than 6 mm (1/4 in). The degree of compactness of heat exchangers illustrate in Figure 2.3 as 'compactness' or 'area density' (Reay, 2002).

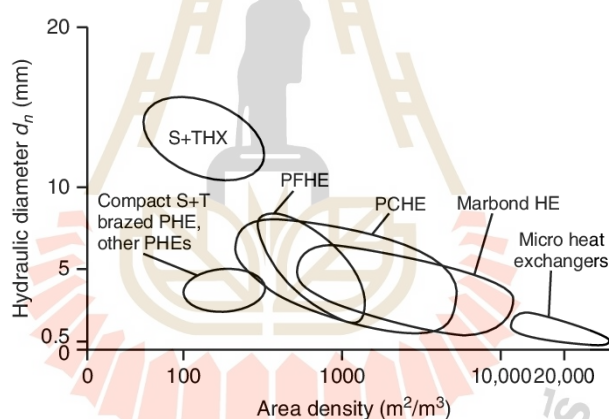


Figure 2.3 The area densities of a range of compact heat exchangers (Reay, 2002).

To improve heat exchanger thermal performance, the easy way is increasing of the heat transfer surface. However, it has a serious drawback because the volume of the heat exchanger and size increases as well, using more fluids. Therefore, compact heat exchangers are interesting to allow a minimal volume increase for a maximal surface increase. The key-point of area density is to have a larger heat transfer surface with the smallest volume. the reducing of the width that means volume and weight leads to a strong increasing of the area density. For same volume and weight,

a microchannel heat exchanger has a much larger heat transfer rate compared to others types.

2.2 Applications of Printed Circuit Heat Exchangers in Cryogenic Fluid Handling

The handling of cryogenic fluids in various industrial sectors has undergone a significant transformation with the utilization of printed circuit heat exchangers (PCHes). As the demand for efficient and reliable cryogenic fluid management continues to grow, PCHes have emerged as indispensable components due to their unique design and exceptional performance characteristics. By providing an overview of PCH technology and its application in cryogenic environments, this study aims to shed light on the crucial role of PCHes in meeting the evolving demands of cryogenic fluid handling across industries.

2.2.1 Cryogenic Fluids

A cryogenic liquid is characterized by having a normal boiling point below $-130\text{ }^{\circ}\text{F}$ ($-90\text{ }^{\circ}\text{C}$). Industrial gases that are typically transported, handled, and stored as liquids at these cryogenic temperatures include argon, helium, hydrogen, nitrogen, and oxygen. Liquefied gases have a normal boiling temperature below 120 K fall under the category of cryogenic fluids (Zohuri, 2018). Liquefied natural gas (LNG) qualifies as a cryogenic fluid due to its existence at extremely low temperatures. It serves as a crucial component for various industries engaged in natural gas production, liquefaction, and distribution, as well as for those utilizing LNG as a fuel source. Nowadays, the use of liquefied natural gas (LNG) has been growing steadily for replacing traditional resources due to its high calorific value and low carbon dioxide emissions, inexpensive. Basically, the natural gas (NG) is transformed to form liquefied natural gas (LNG) by cooling natural gas to cryogenic temperatures $-160\text{ }^{\circ}\text{C}$ for it is stored and transported over long distances. liquid state has a volume approximately 600 times smaller than when in its gaseous form, resulting in economical transported and safely over long distances. Before being transferred into pipelines, LNG is warmed and regasified to convert the NG gas along with the user demands. There are different composition of natural gases depending on it has a different gas composition and

different amounts of each component. Natural gas is a combustible mixture gas, an organic compound of hydrogen and carbon, petroleum. The primarily natural gas is formed methane and also includes ethane, propane, butane, and pentane. Natural gas composition is shown in Table 2.1 (Smithson, 2023).

Table 2.1 Chemical composition of natural gas.

Compound	Symbol	Percent in Natural Gas
Methane	CH ₄	60-90
Ethane	C ₂ H ₆	0-20
Propane	C ₃ H ₈	0-20
Butane	C ₄ H ₁₀	0-20
Carbon Dioxide	CO ₂	0-8
Oxygen	O ₂	0-0.2
Nitrogen	N ₂	0-5

In LNG platform, the liquefaction process overcomes the economic barriers imposed where NG is distributed at large distances from the source. However, the liquefaction operation is needed a greater energy and cost intensive process for conversion the NG to its liquid phase by cryogenic refrigeration technologies. Therefore, a huge amount of cold energy is received from the transported LNG process that could potentially be recovered in downstream operations when liquid convert to NG. During regasification process, the cryogenic energy could provide an energy saving of 200 kW h/ton LNG (Li et al., 2017). However, the conventional vaporizer at LNG receiving terminals don't satisfy this valuable low temperature cold energy. These conventional vaporization technologies are thermally inefficient and have a drawback sustainable impact on the locality as ambient heat sources are used to vaporize the processed LNG. Therefore, the LNG receiving terminals must be employed with efficient and reliable heat exchangers, also known as "vaporizers." These vaporizers play a crucial role in efficiently converting LNG back into its gaseous form while minimizing energy

consumption and environmental impact. Therefore, investing in advanced vaporization technologies is essential to enhance the efficiency and sustainability of LNG regasification processes (Pospíšila et al., 2019).

2.2.2 PCHE technology and its application in cryogenic environments

A significant amount of cryogenic energy (850 kW h/ton-LNG) is required for the liquefaction of NG before transportation. The total amount of LNG cold energy is wasted about 20 million MW h per year (Pospíšila et al., 2019). This options are required to improve the thermo-economic performance of this combined facility through the integration of LNG cold energy. Some of options for LNG cold energy integration currently being used in industry are as the following:

(1) Cryogenic Air Separation and Liquefaction (ASL): ASL is a process that separates and liquefies atmospheric air into nitrogen, oxygen, and argon by cooling it to cryogenic temperatures. The integration of LNG cold energy with the ASL process provides a low-temperature heat sink that enhances the efficiency of refrigerant condensation, such as nitrogen. This approach reduces the overall energy required for cooling and liquefaction, leading to cost savings and improved performance in cryogenic applications, including LNG regasification and high-purity gas production.

(2) BOG (Boil Off Gas) re-liquefaction: Some cold energy requires for the condensation of BOG that can be provided from sub-cooled LNG in the initial pumping stages during the send-out operation.

(3) Desalination of sea water: the cold energy is utilized for the integration with the sea water desalination process to produce the fresh water.

(4) Thermal storage and food processing: LNG vaporization energy can also be utilized to assist the cryogenic energy requirement for the sustainable low temperatures in refrigerated warehouses (Koku et al., 2014).

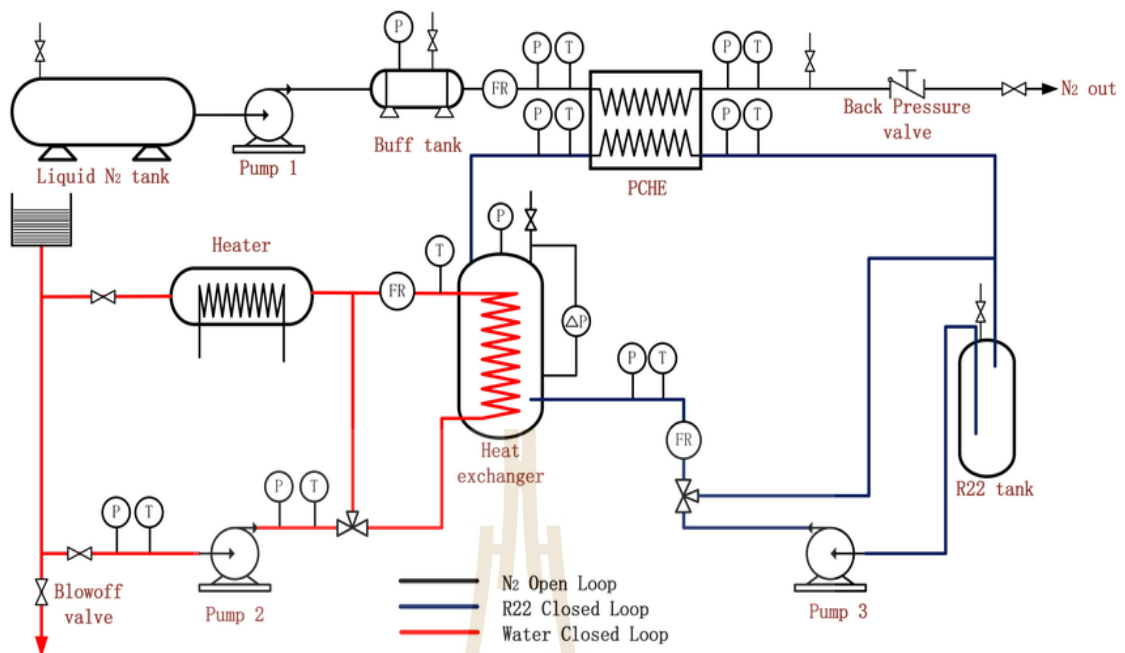


Figure 2.4 The test schematic of liquefied gas vaporization process (Zhao, Chen, et al., 2019)

This particular configuration of energy recovery options or power generating facility become the key in LNG vaporization process. The common LNG vaporizers are as intermediate fluid vaporizers, open rack vaporizers (ORVs), super ORVs and submerged combustion vaporizers (Han et al., 2017; Liu et al., 2016; Pan et al., 2016). These traditional LNG vaporizers have low efficiencies and huge volumes, and they do not satisfy the requirement of high efficiency and high compactness in finite volume vaporization processes in the construction of LNG gasification systems. Thus, the design of a high-performance compact vaporizer is importance in practical industry. In this regard, minichannels heat exchanger is a promising candidate of vaporizers with excellent performance and small components, of which PCHE is the most representative example. The printed circuit heat exchanger (PCHE) have attracted in recent years to replace these traditional vaporizers because of safety, high compactness and efficiency under high pressure and low temperature operating (Chu et al., 2017; Kim & No, 2011; Yoon et al., 2014).

One of techno-economic evaluation of PCHE for the heat integration of vaporization cold energy in natural gas processing illustrates in Figure 2.4 (Zhao, Chen, et al., 2019). This energy recovery process was combined of an open liquid nitrogen vaporized loop, a closed R22 loop, and a closed water loop. A cryogenic liquid pump vented out liquid nitrogen from the low-pressure tank and was pressurized to supercritical pressure. After passing through a buff tank, the cryogenic liquid nitrogen was transformed into supercritical nitrogen by passing through the PCHE. On the hot side, R22 refrigerant gas was circulated in the closed loop. Hot water in a shell and tube heat exchanger with a horizontal floating plate after passing through a three-way control valve and a mass flowmeter heated the liquid R22 in the R22 tank. Hence, the hot R22 passed through PCHE and transferred the heat to the cold side. For driving the water, a water pump was used in the closed water loop. The water was heated by an electric heater and was then flowed into the heat exchanger for transferring heat to R22; an electro-magnetic flowmeter measured the water flow.

The benefits of PCHEs provide the opportunity to use the waste heat of the exhaust gases and LNG cold energy in a combined system. This research aims to improve the thermal and hydraulic performance of PCHE for the critical LNG applications utilizes in energy recovery or power generating system.

2.3 Effects of Geometric and Operational Parameters on Minichannels PCHE Thermal Hydraulic Performance

Printed Circuit Heat Exchangers (PCHEs) play a pivotal role in the handling of liquefied natural gas (LNG), where they must operate effectively under varying conditions. The optimization of these heat exchangers involves a careful balance of operating parameters and geometric variables tailored to the specific cryogenic application. This optimization process has a significant impact on the thermal and hydraulic performance of PCHEs in cryogenic environments.

Four main kinds of PCHE flow channels are straight, zigzag, S-shape, and airfoil fin; the basic structure parameter; as shown in Figure 2.5 (Kim et al., 2015; Saeed et al., 2020). The structure of PCHEs are the key factors to enhance heat transfer characteristics and to reduce the pressure drop characteristics for the better thermal

hydraulic performance. Basically, the heat transfers and pressure drop characteristics of PCHEs depend on the type of flow channels.



Figure 2.5 Different kinds of PCHE flow channels (Kim et al., 2015; Saeed et al., 2020).

In recent years, researchers have focused on investigating PCHEs heat transfer and hydraulic characteristics with various flow channels, both through numerical simulations and experimental studies. Particularly, this current study has emphasized the thermal-hydraulic performance of PCHEs featuring zigzag channels. The enhancement of heat transfer in PCHEs can be achieved by increasing either the convective heat transfer coefficient or the surface area exposed to heating. Zigzag channel configurations in PCHEs effectively extend the heated surface area, thereby improving heat transfer performance between primary and secondary working fluids.

2.3.1 Effects of Bending-Angle on Thermal Hydraulic Performance of Zigzag Channels PCHEs

Researchers have recently proposed that zigzag channel PCHE could provide excellent heat transfer performance and compactness. Lee et al. (Lee & Kim, 2013) studied the performance of a zigzag PCHE with semicircular, rectangular, trapezoidal, and circular channel cross-sections. In their studies, the cold side's channel bending angle (α) was 40° , while that of the hot channel was 35° . The structural parameters of zigzag channel are shown in Figure 2.6. Saeed et al. (Saeed & Kim, 2017) performed a numerical study to evaluate the thermal-hydraulic performance of supercritical carbon dioxide (SCO_2) PCHE with different zigzag-channel angles from 25° to 40° . The pitch, center-to-center longitudinal distance in flow direction between the adjacent tubes (one bend unit), is in the range of 7.24–16.195 mm of geometric configurations. The results indicated that an increase in the channel

bending angle on both the cold and hot sides decreased the performance evaluation criteria of the PCHE. Lee et al. (Lee & Kim, 2012) conducted optimization of zigzag channel geometries based on the channel curved angle (8° , 20.5° , 32.5° , 35.5° , 40° , and 41°) and the ellipse aspect ratio (0.6, 0.66, 1.08, 1.29, 1.57) of the cold side to investigate the flow and heat transfer characteristic between design parameters. The thermal-hydraulic performance of a printed circuit LNG vaporizer with a semi-circular zigzag channel was numerically investigated by Pan et al. (Pan et al., 2020) for various bending angles (0° , 15° , 30° and 45°) of both cold and hot channels; the 15° bending angle showed the best performance. The curved angles of the zigzag channel shape were analyzed by Meshram et al. (Meshram et al., 2016). They found that a larger bending angle provided better heat transfer but had a pressure drop penalty. Chen et al. (Chen et al., 2016) studied a high-temperature PCHE to minimize the pressure drop and improve the heat transfer characteristics for a Reynolds number range of the laminar-transition flow region. Yoon et al. (Yoon et al., 2017) also performed computational fluid dynamics (CFD) predictions on the thermal-hydraulic characteristics of PCHEs with different elbows of zigzag channels (10° , 15° , 20° to 45°). They determined that the fluid pressure drop of the zigzag channel PCHE dominated the zigzag channel geometry, and the Nusselt number could influence the overall heat exchanger design. Lee et al. (Lee et al., 2017) reported that the thermal design of zigzag-type PCHEs with inserts varies between 0.5 mm and 2 mm in the length of linear channels. They suggested that a straight channel of 1 mm was a better design for heat transfer parameters and pressure losses in the PCHE. Therefore, the zigzag channel's bending angle is still an important design parameter for improving the performance of zigzag-type PCHEs. Hu et al. (Hu et al., 2021) analyzed the heat transfer characteristic flows depending on different mass flux conditions inside the zigzag angle 15° channels of PCHEs using an experimental method. The rate of heat transfer increased with mass flux increments. The overall heat transfer performance of supercritical carbon dioxide (SCO_2) in a printed circuit heat exchanger with a zigzag fin was experimentally investigated by Li et al. (Li et al., 2019). They proposed a new evaluation method based on the working mass flow rates, pressure, and flow rate. Finally, they demonstrated that increasing the mass flow rate and operating pressure affected the

heat transfer coefficient. Cheng et al.(Cheng et al., 2020) studied the effect of mass flow rates on the pre-cooler thermal performance of the supercritical CO₂ Brayton cycle. In this study, the zigzag angle and pitch number were 32.5° and 9 mm on the SCO₂ side, and 15° and 24.6 mm on the water side, respectively. They found that the development of the heat transfers and increases the pressure drop while the high inlet Reynolds number on the SCO₂ side. The higher pressure losses were due to the disturbance of the fluids in the flow passages, which was necessary to reduce the effectiveness of the heat exchanger.

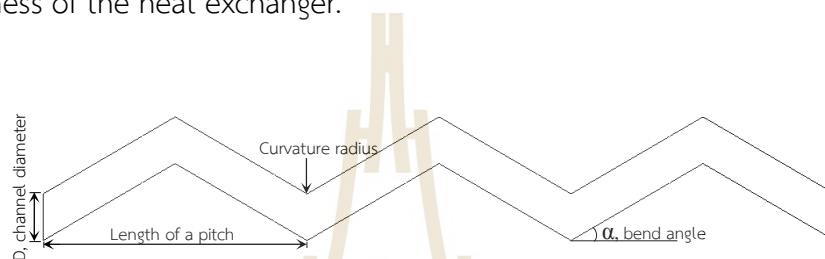


Figure 2.6 Structural parameters of a zigzag channel.

2.3.2 Effects of Various Geometric Parameters on Thermal Hydraulic Performance of PCHEs

The effect of a narrow cross-section wavy channel on the PCHE thermal-hydraulic performance was numerically studied by Yang et al.(Yang et al., 2019). The narrow cross-section channel slightly dropped the total heat transfer rate and increased the pumping power. Lee et al. (Lee & Kim, 2013) investigated the effect of zigzag channel cross sections (semicircular, rectangular, trapezoidal and circular) on thermal-hydraulic performance. de la Torre et al. investigated the impact of bend radius and zigzag angle on mechanical and thermal stresses (Torre et al., 2023). Jin and colleagues (Jin et al., 2022a) conducted a study focusing on the optimization of zigzag channels, exploring the effects of pitch, bend angle, and bend radius. It was found that the bend angles had a notable impact on both heat-exchange capacity and pressure drop. Changes in pitch primarily influenced the channel count, showing less influence compared to other structural factors. Additionally, they observed that maintaining a suitable bend radius of less than 3 mm facilitated smooth flow direction transitions, enhancing flow resistance while preserving heat transfer capability. de la Torre and

colleagues (Torre et al., 2021) investigated the influence of zigzag channel parameters on thermal-hydraulic performance to establish optimal designs. They introduced two optimal designs aiming for the lowest Fanning friction factor and the highest Nusselt number. In the first design, they proposed a zigzag length to hydraulic diameter ratio (l_z/D_h) of 6.15, a bend angle (α) of 45° , and a bend radius to hydraulic diameter ratio (R/D_h) of 0. For the second design, the parameters were $l_z/D_h = 12.3$, $\alpha = 5^\circ$, and $R/D_h = 4.2$. Additionally, they developed correlations linking the Nusselt number (Nu) and the friction factor for helium fluid to the geometric parameters and the Reynolds number. Lee et al. (Lee et al., 2017) investigated a new configuration for a Printed Circuit Heat Exchanger (PCHE), which combined a zigzag-type PCHE with a straight channel at the bending point. The lengths of these straight channels ranged from 0.5 to 2 mm, while the mass-flow rates varied from 1.41×10^{-4} to 2.48×10^{-4} kg/s. Introducing a 1 mm straight channel led to a significant improvement in thermal-hydraulic performance, showing an increase of approximately 26–28% compared to the original zigzag channel. Experimental studies on a microchannel heat exchanger (MCHE) assembly with asymmetric zigzag flow channels on the hot and cold sides were carried out by Chen Zeng and colleagues (Zeng et al., 2022). In comparison to the cold side, there are fewer channels on the hot side but a greater heat transfer area since the flow channels on the hot side were constructed with a bigger hydraulic diameter. The study used volume and area goodness factors to assess the total thermal-hydraulic performances of symmetric and asymmetric structures after establishing correlations for the Nusselt number and friction factor. The outcomes showed that the symmetric design was not as effective as the asymmetric structure MCHE. The results showed that the asymmetric design showed up to 2.72 times greater area goodness factor and 3.35 times higher volume goodness factor within the experimental range. Wang et al. (Wang et al., 2023) conducted a numerical investigation to compare the thermal-hydraulic performance of various zigzag channel configurations with different angles and straight sections inserted at the bending point. The study revealed that the addition of a straight portion resulted in a slight decrease in heat transmission, a significant reduction in pressure loss, and an improvement in flow uniformity. Furthermore, the thermal performance was notably enhanced for the two modified

channels with smaller pitch angles and larger inserted straight section ratios compared to the straight channels. Zhou et al. (Zhou et al., 2024) analyzed numerically to compare the performance of a modified bending point zigzag channel with the original channel. The investigation revealed that incorporating a continuous turning structure into the zigzag channel resulted in a substantial improvement in heat transfer. This modification also influenced key variables such as specific heat and eddy viscosity. Particularly noteworthy was that both the straight channel at the bending point and the zigzag channel with rounded corners exhibited significantly enhanced thermal and hydraulic performance compared to the original zigzag channel. Jin et al. (Jin et al., 2022b) focused on investigating the impacts of different structural parameters in zigzag channel Printed Circuit Heat Exchangers (PCHEs). Among these parameters were pitch sizes ranging from 10 to 25 mm, zigzag angles varying from 90 to 165 degrees, and bend radii spanning from 0.2 to 7.0 mm. The analysis revealed notable variations in flow resistance and heat transfer efficiency, particularly highlighting the effects of changes in bend radius and zigzag angle.

2.3.3 Operational Parameters of Zigzag PCHEs

The two PCHEs performance in a high-temperature helium test facility was investigated by Mylavarapu et al. (Mylavarapu et al., 2014). The experiment ranges of inlet temperature, pressure, Reynolds number varied 85°C-390°C, 1.0-2.7 MPa, 950-4100 on cold side; and on hot side data ranges are 208°C-790°C, 1.0-2.7 MPa and 900-3900, respectively. The pressure losses and fluid temperatures were measured to determine flow resistance and heat transfer characteristics of the channel surface. Tang et al. (Tang et al., 2021) analyzed the thermal performance in a zigzag channel printed circuit heat exchanger with supercritical liquefied natural gas as working fluid under different conditions. They proposed correlations between the Nusselt number and Prandtl number for mass flux within the range of 1.4 - 89.4 kg/(m².s), inlet temperature 180-340°C, operating pressure 7-9 MPa, and wall thermal conductivity 5-45 W/m.K. Zhao et al. (Zhao et al., 2020) conducted an experimental and numerical investigation on supercritical nitrogen in airfoil fin printed circuit heat exchanger, concluding that the increase of mass flow rate increases the average convective heat transfer coefficient for inlet pressures ranging from 5 MPa to 8 MPa. Shi et al. (Shi et al., 2020) studied the

friction features and heat transfer between molten salt and supercritical CO₂ in the airfoil channel of PCHE under different mass flow rate and inlet temperature conditions. Shin and Yoon (Shin & Yoon, 2020) investigated two-phase nitrogen in a PCHE, to understand the pressure drop and the heat transfer coefficients when the phases transition from two- to single-phase. Peng et al (Peng et al., 2020) simulated the propane transcritical flow and condensation flow in a double bank channel unit for the PCHE under various mass fluxes. Local heat transfer coefficient as well as pressure drop was investigated during the phase-change process. R134a condensation flow in a 1 mm diameter circular tube with various mass fluxes was analyzed by Da Riva et al. (Da Riva et al., 2012) The results suggested that the turbulence condensation is very important under the large mass flux simulations.

2.4 A Review on Phases Transition Process in Minichannels of PCHEs

Evaporation and condensation is a key heat transfer mechanism, particularly in systems where phase change occurs, such as in cryogenic, cooling, or heating applications. By focusing on the evaporation process, researchers can explore methods to enhance heat transfer within minichannels. Efficient evaporation processes can lead to reduced energy consumption in heat exchangers, which is beneficial for both environmental sustainability and cost savings. Emphasizing the evaporation process in minichannels PCHEs allows researchers and engineers to delve deeper into the fundamental mechanisms of heat transfer, leading to improved efficiency, optimized designs, and advancements in microscale technologies.

For the advancement of PCHEs in two-phase cryogenic applications, it is crucial to know the condensation and evaporation heat transfer characteristics of natural gas (NG). Goto et al. (Goto et al., 2023) conducted experimental research to explore the impact of channel geometry on condensation flow visualization, heat transfer, and pressure drop within straight and wavy minichannels PCHEs. Their findings indicated that wavy minichannels demonstrated enhanced heat transfer and pressure drop performance in comparison to straight channels. Hu et al. (Hu et al., 2023) conducted flow boiling characteristics experiments of R22 in zigzag channels, heat transfer coefficient correlation was developed to reflect the effects of sloshing conditions.

Yoo et al. (Yoo et al., 2022) examined condensation heat transfer and pressure drop in PCHEs with semicircular channels using propane. Thirty experimental cases explored different mass fluxes, saturation pressures, and vapor quality to derive correlations for the two-phase heat transfer and pressure drop. Liu et al. (Liu et al., 2012) explored an experimental investigation of flow instability, two-phase flow patterns, and performance analysis within a microchannel co- and counter-current heat exchanger. The heat exchanger, measuring 20 mm by 20 mm, featured 18 parallel microchannel on both sides. They recommended the use of the counter-current configuration due to its remarkable efficiency enhancement at higher mass fluxes compared to its cocurrent counterpart. Zhao et.al (Zhao, Zhang, et al., 2019) examined the condensation flow of R22 refrigerant in the minichannels of a PCHE with a hydraulic diameter of 0.91 mm. Various flow patterns, including smooth-annular and wavy-annular flows, were observed at different refrigerant mass fluxes, with an extension of the annular region downstream as the R22 mass flux increased. Optimal heat transfer performance was found at an inlet vapor quality of 0.7, with the local condensation heat transfer coefficient increasing with rising R22 mass flux. Additionally, they established correlations that provide valuable tools for further analysis and optimization of PCHE designs for enhanced performance in refrigeration and cooling applications. Song et.al (Song et al., 2022) investigated flow boiling heat transfer in two types of rectangular radial microchannel heat exchangers to address heat dissipation challenges in high heat flux devices. Mathematical models were developed to optimize their structural parameters and validated using the heat transfer coefficient (HTC). Results show that the grooved heat exchanger consistently exhibits better heat transfer performance compared to the one without grooves. These findings offered insights into optimizing microchannel heat exchanger designs for enhanced heat transfer efficiency. Liang (Liang et al., 2022) introduced and investigated for capillary microchannel flow and heat transfer characteristics using simulations based on the phase-field model. The noncircular channels exhibit increased capillary flow rates and heat transfer capacities due to changes in liquid surface curvature at acute angles and expansion of the adsorption layer on the wall surface, all while maintaining capillary pressure. Moreover, they revealed that increasing diameter and wettability enhances

heat transfer capacity in the initial stages of capillary flow. Metallic microstructure devices with multi-microchannel array arrangements have been developed and tested for liquid evaporation, particularly with water, by Anurjew et al. (Anurjew et al., 2011). They found that long straight microchannel are not optimal for evaporation. Baek et al. (Baek et al., 2014) analyzed the two-phase heat transfer coefficients of an argon–refrigerant mixed refrigerant heat exchanger. The study revealed that condensation heat transfer coefficients were low, measuring below $1000 \text{ W/m}^2 \text{ K}$ for mass fluxes ranging from 0 to $250 \text{ kg/m}^2 \text{ s}$, while evaporation coefficients peaked around $5000 \text{ W/m}^2 \text{ K}$ at $350 \text{ kg/m}^2 \text{ s}$.

Through the synthesis of various studies, it highlights the key factors influencing phase transition, such as heat transfer coefficients, flow patterns, and channel geometries. The findings underscore the importance of optimizing minichannel designs for efficient phase transition, offering valuable insights for the development of high-performance PCHE systems for such applications as multi-channel heat exchangers, electronic device cooling, refrigeration and cryogenic devices, air separation, and the petrochemical industry.

2.5 An Overview of the Literature Review

From the literature, researchers have investigated the thermal-hydraulic performance of PCHEs with various zigzag channel types. Those studies showed that the zigzag channel bending angles have an important influence on the thermal-hydraulic performance of PCHEs. Therefore, the analysis of zigzag bending angles can help improve the comprehensive performance of PCHEs. Most of the PCHE performance evaluations have been based on a 15° bending channel angle, and some analyses have focused on larger intervals of bending channel angles, such as 0° , 5° , 10° , and 45° . The literature found that the heat transfers steeply increased in the low-bending-angle interval and did not significantly increase in the high-bending-angle interval. However, the pressure drop increased fluently in the high-bending-angle interval (Chen et al., 2019; Meshram et al., 2016; Pan et al., 2016; Yoon et al., 2017). The higher pressure drop can affect the pumping power consumption and the thermal cycle economy. This suggested that the low-bending-angle interval PCHE achieved high

performance. It was interesting to determine the best bending angle of the zigzag channel at smaller angle intervals. Therefore, this study aimed to evaluate the smaller interval bending channel angles (0° , 3° , 6° , 9° to 30°) of the PCHE and the weight between the thermal and hydraulic characteristics, such as enhancing the heat transfer rate and reducing the pressure loss. With the aforementioned motivation, new correlations were developed using the optimal bending channel angles of PCHE designs to predict the Nusselt number and Fanning friction factor. This investigation specifically focused on Reynolds numbers below 2000.

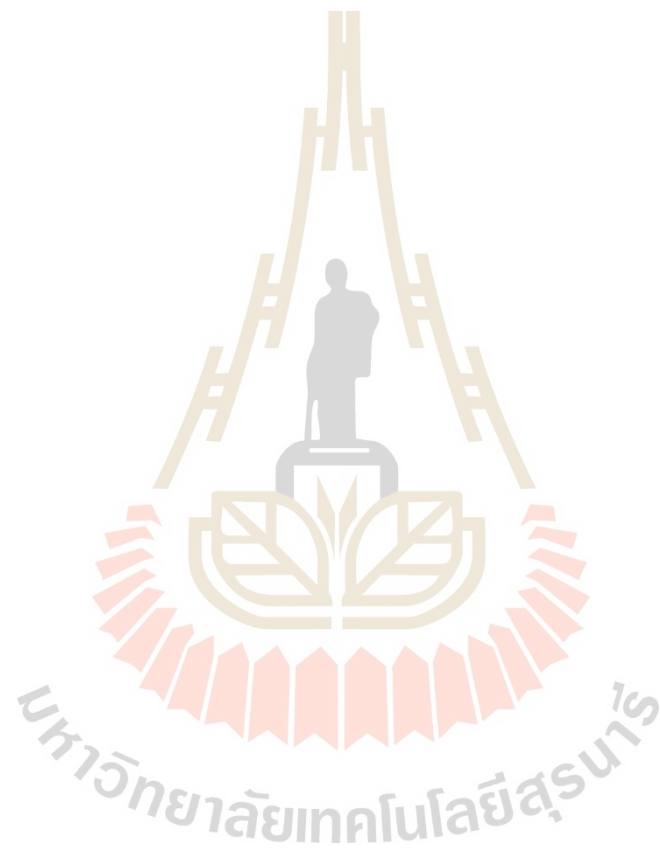
According to the overview of various geometric parameters effect, numerous experimental and numerical studies have been conducted to optimize the channel geometry and operational parameters to increase the performance and compactness of zigzag PCHEs. It was determined that as a continuous channel type, the performance of the zigzag-type PCHEs must be enhanced. PCHEs are still highly expensive, and additional work is required to make them more compact and economical. Therefore, the current work concentrated on using a numerical approach to optimize the channel geometry to improve the PCHE performance and cost-effectiveness. The previous assessment evaluated the effect of the smaller interval bending angles (ranging from 0° to 30° in increments of 3°) and varying channel curvature lengths on the performance of zigzag channel PCHEs while maintaining a constant channel diameter of 2 mm. However, the bending flow exerted a substantial influence on the convection heat transfer rate and friction loss factor due to the flow separation and reverse flow. It is interesting to note the influence of bending flow variations on the thermal-hydraulic performance of PCHEs when altering the zigzag channel diameter. Therefore, this study introduces a novel approach for determining the optimal bending number of the zigzag channel in printed circuit heat exchangers (PCHEs) based on the semicircular channel diameter (2mm-5mm). The goal is to enhance heat transfer performance. The heat transfer rate and frictional resistance of PCHEs are investigated by simulations using three-dimensional numerical models. Although various correlations for Nusselt number and Fanning friction factor in zigzag channel PCHEs have been established, their accuracy remains unverified within the novel bending number ranges for the different channel diameters. The main purpose of the current

study is to address these uncertainties. In addition, the operational parameters of PCHEs are diverse and interconnected, requiring careful consideration and optimization to achieve efficient heat transfer, safe operation, and energy efficiency across a range of applications and working conditions. In this study, a range of operational parameters spanning from cryogenic to very high temperatures, and from low to elevated pressures, were considered across various mass flow rates.

For the zigzag channel optimization analysis, helium in supercritical states was selected over cryogenic fluids for several practical and technical reasons. Supercritical fluids avoid phase boundaries, which simplifies the modeling process by eliminating issues related to phase separation and instability, resulting in more stable and efficient flow within the channels. In contrast, cryogenic fluid simulations are time-consuming and complex, often taking 1-4 months per case, which makes them less practical for extensive design optimization. Supercritical fluid simulations are less computationally demanding and can be validated using existing experimental and CFD data, streamlining the optimization process. By using supercritical helium, the study benefits from improved efficiency, reduced computational costs, and the ability to utilize validated data, leading to more effective and practical optimization of zigzag channel designs.

While research on two-phase PCHE is ongoing, much of the data available from previous studies is constrained in terms of the scale and application of PCHE. When designing a PCHE for Floating Storage Recirculation Unit (FSRU) applications and Liquefied Natural Gas (LNG) transfers, it becomes crucial to thoroughly assess the heat transfer performance under two-phase conditions. The literature studies showed that two-phase localized heat transfer within PCHEs proves to be a challenging task. Therefore, it is necessary to study the two-phase heat transfer through CFD simulation, which can possibly decrease energy consumption and manufacturing costs. This study aimed to gain insights into the behavior of two-phase flow during flow vaporization in a minichannel by combining experimental observations with numerical simulations. The simulations used nitrogen and methane as the working fluids. Additionally, the effect of evaporation parameters was analyzed, with particular attention given to the

evolution of the flow modes and the local flow and transport phenomena. The accuracy of the simulations was validated with experimental data.



CHAPTER III

RESEARCH METHODOLOGY AND NUMERICAL MODEL VALIDATION

This chapter outlines the research methodology, simulation techniques, and validation procedures utilized to ensure the accuracy and reliability of the study's findings. In this thesis, the simulation techniques and validation strategies are divided into two sections: zigzag channel PCHEs parameter optimization and straight channel PCHEs evaporation parameters. The present numerical models are validated with experimental, reliable numerical and theoretical results. By meticulously detailing the simulation techniques and validation strategies, this study aims to provide a robust framework for understanding and optimizing PCHE thermal hydraulic performance.

3.1 Geometrical Configurations and Boundary Condition of the Zigzag Channel

In this numerical analysis, 3D modellings were carried out using the ANSYS-FLUENT code for (0°, 3°, 6°, 9° to 30°) bending zigzag-channel PCHE. For validation, a 15° bending zigzag-channel PCHE was modeled, and numerical results were validated with the results obtained from Chen et al. experiment (Chen et al., 2019). Under different fluid flow conditions, the Reynolds number especially helps to predict the flow characteristics, defined as the ratio of inertial forces to viscous forces occurring in fluid relative to internal movement due to different fluid velocities. In this study, the Reynolds number (Re) range was lower than 2,300 in the laminar flow condition, and helium used as the working fluid. The computational domain of detailed geometry is illustrated in Figure 3.1.

The arrangement of the flow channels was a single bank method, a counter-flow arrangement. There were two periodic boundary conditions: one was between the top and solid bottom walls, while another was for the left and right solid walls. The boundary conditions of the front and back solid walls were considered adiabatic. The plate material was Alloy 617, which has a density of 8,360 kg/m³, and temperature-

dependent functions for the specific heat and thermal conductivity were obtained from the Special Metals online database (SpecialMetals, 2005). Then, the NIST chemistry webbook (NIST, 2023) was applied to export the thermo-physical properties of helium as an implemented file into ANSYS-FLUENT. For the fluid boundaries, the inlet mass flow rates were 1.1238×10^{-4} kg/s per channel on both the hot and cold channels; the cold inlet temperature was 623.15 K, and the hot side was 1073.15 K.

(a) Three-dimensional single banking domain

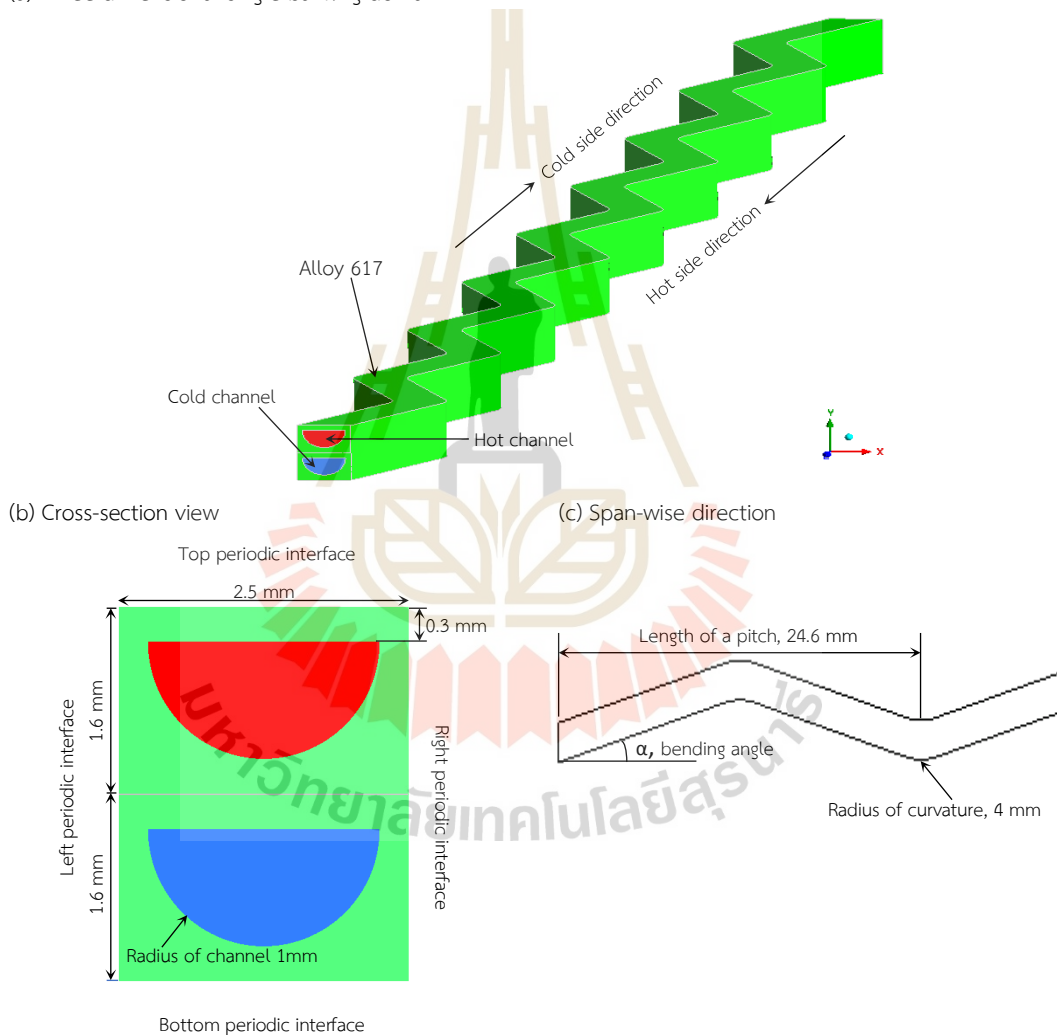


Figure 3.1 Physical model of the zigzag channel PCHE with counter flow arrangement.

The outlet pressure of helium was set to 3 MPa on both sides, and the operating pressure was 3 MPa, respectively. The fluid boundary walls were set as a

couple walls. In addition, the bending angle was 15° , the radius of the fillet at the bends was 4.0 mm, and the semicircle-nominal diameter was 2 mm on both channels. The modeled block of each side was created with a thickness of 1.6 mm and a width of 2.5 mm, which inserted a total of 16 zigzag bends per flow channel, channel a pitch length of 24.6 mm respectively.

3.2 Equations Governing Flow and Heat Transfer in Zigzag Channel Simulation

For the execution of three-dimensional conjugate heat transfer in zigzag channel PCHEs, the commercial computational fluid dynamics code (Ansys Fluent), a steady state was used in simulation. The SIMPLE algorithm was selected for pressure and velocity coupling because a small error was observed between the simulation results obtained using the SIMPLE algorithm and the experimental results compared with other algorithms (Zhao, Zhou, et al., 2019a). The SIMPLE algorithm (Semi-Implicit Method for Pressure-Linked Equations) is an iterative method in computational fluid dynamics for solving the Navier-Stokes equations. It couples velocity and pressure fields by iteratively solving momentum equations, correcting pressure, and updating velocities until convergence. In addition, the SIMPLE algorithm produces a more economical and stable iteration method. Second-order numerical schemes were adopted to solve the governing equations to obtain accurate results. In simulation, viscous dissipation and thermal radiation effects were not considered. In this research, the effects of bending angle on PCHE performance simulation were based on a laminar model. The continuity equation for the laminar flow of an incompressible fluid through the zigzag channel is given by (Khan et al., 2021):

$$\nabla \cdot \vec{u} = 0 \quad (3.1)$$

where \vec{u} is the velocity vector. The momentum equations, based on the Navier-Stokes equations, describe the fluid flow in the zigzag channel:

$$\nabla \cdot (\rho \vec{u} \vec{u}) = -\nabla p + \nabla \cdot (\mu \nabla \vec{u}) \quad (3.2)$$

Here, ρ is the fluid density, p is the pressure, and μ is the kinematic viscosity. The energy equation governs the heat transfer within the zigzag channel:

$$\nabla \cdot (\rho C_p T_f \vec{u}) = \nabla \cdot (k_f \nabla T_f) + Q \quad (3.3)$$

where f represents the fluid, T is the temperature, C_p is the specific heat capacity at constant pressure, k is the thermal conductivity, and Q represents any heat sources or sinks.

For the mesh convergence study, The shear-stress transport (SST) k - ω turbulence model was incorporated to account for turbulent fluctuations in the flow and heat transfer equations (Argyropoulos & Markatos, 2015; Cong et al., 2021):

$$\nabla \cdot (\rho k \vec{u}) = \nabla \cdot \left[\left(\mu + \frac{\mu_t}{\sigma_k} \right) \nabla k \right] + G_k - \rho \epsilon \quad (3.4)$$

$$\nabla \cdot (\rho \omega \vec{u}) = \nabla \cdot \left[\left(\mu + \frac{\mu_t}{\sigma_\omega} \right) \nabla \omega \right] + G_\omega - \beta \rho \omega^2 + \frac{\rho \sigma_\omega^2}{\omega} \nabla \cdot (\mu_t \nabla \omega) \quad (3.5)$$

Where k is the turbulence kinetic energy, ω is the specific rate of dissipation of turbulent kinetic energy, μ_t is the turbulent viscosity, and σ_ω are model constants. The symbol ϵ represents the specific rate of dissipation of turbulent kinetic energy. The terms G_k and G_ω represent the generation terms for turbulent kinetic energy (k) and the specific rate of dissipation of turbulent kinetic energy (ω), respectively.

3.3 PCHEs Performance Parameters

There are two main performance measurements of the heat exchanger: pressure drop and heat transfer rate. Pressure losses were created by the flow disturbances from changes in fluid density, viscosity, and elbow direction over the length when the fluid passed through the channel from its beginning to its end. For each fluid, the global pressure loss factor (f_g) could be calculated as (Chen et al., 2019):

$$f_g = \frac{\Delta P_f d_h \bar{\rho} A_c^2}{2\dot{m}^2} \quad (3.6)$$

Where d_h represents the hydraulic diameter of the channel, $\bar{\rho}$ is the mean fluid density calculated by using the average temperature based on each channel's inlet and outlet temperatures. A_c denotes the cross-sectional area of the channel in the spanwise direction, \dot{m} represents the mass flow rate, and l is the fluid-flow actual length. The total pressure loss is expressed as ΔP_f , which can be calculated as follows:

$$\Delta P_f = P_{inlet} - P_{outlet} \quad (3.7)$$

where P_{inlet} and P_{outlet} are the static pressures at the inlet and outlet of the zigzag channel in the PCHE, respectively. The global heat-transfer coefficient was computed using Eq. (3.8), which requires the global heat transfer rate, bulk fluid temperature, and wall temperature.

$$h_g = \frac{q_g''}{|T_{f,g} - T_{w,g}|} \quad (3.8)$$

where q_g'' notes the averaged-surface heat flux, $T_{f,g}$ is the arithmetic mean temperature between the inlet and outlet temperature of each side, and $T_{w,g}$ represents the average of the four terminal temperatures of a zigzag-type channel PCHE. They can be defined as,

$$T_{f,g} = \frac{(T_{inlet} + T_{outlet})}{2} \quad (3.9)$$

$$T_{w,g} = \frac{(T_{h,inlet} + T_{h,outlet} + T_{c,inlet} + T_{c,outlet})}{4} \quad (3.10)$$

Convection is fundamentally based on two heat-transfer mechanisms: thermal diffusion (conduction) and thermal convection (fluid motion). The dimensionless form of the convective heat transfer parameter is described by the Nusselt number (Nu) in

fluid dynamics, which is the ratio of the convective to conduction heat transfer under the same conditions. For either the cold or hot channel of PCHE, Nu can be calculated using Eq. (3.11).

$$Nu = \frac{h_g d_h}{k} \quad (3.11)$$

where k is the fluid thermal conductivity, calculated based on the average fluid temperature between the inlet and outlet of each channel.

The Euler number (Eu), which signifies the relationship between pressure drop, dynamic velocity head, and the relative momentum loss rate, is expressed as follows (Zhao, Zhou, et al., 2019b):

$$Eu = \frac{\Delta p_f}{\bar{\rho} v^2 / 2} \quad (3.12)$$

Where v is the mean velocity calculated by using the average temperature based on each channel's inlet and outlet temperatures.

The effectiveness values for the PCHEs with various zigzag channel angles PCHEs were evaluated using the mass flow rate and measured fluid temperature. The fluid flow rates and inlet temperature at the channel entrance of PCHEs could have non-uniform distribution, affecting the heat exchanger's steady-state condition. The effectiveness of a heat exchanger is the ratio of the actual heat transferred to the maximum heat that can be transferred in a heat exchanger with an infinite area, which is given as (Nemati et al., 2015),

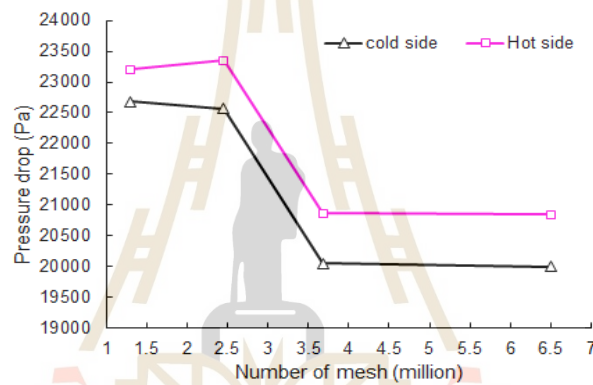
$$\varepsilon = \frac{(\dot{m}c_p)_c (T_{c,outlet} - T_{c,inlet})}{(\dot{m}c_p)_{min} (T_{h,inlet} - T_{c,inlet})} = \frac{(\dot{m}c_p)_h (T_{h,outlet} - T_{h,inlet})}{(\dot{m}c_p)_{min} (T_{h,inlet} - T_{c,inlet})} \quad (3.13)$$

$$\varepsilon = \frac{T_{c,outlet} - T_{c,inlet}}{T_{h,inlet} - T_{c,inlet}} \quad (3.14)$$

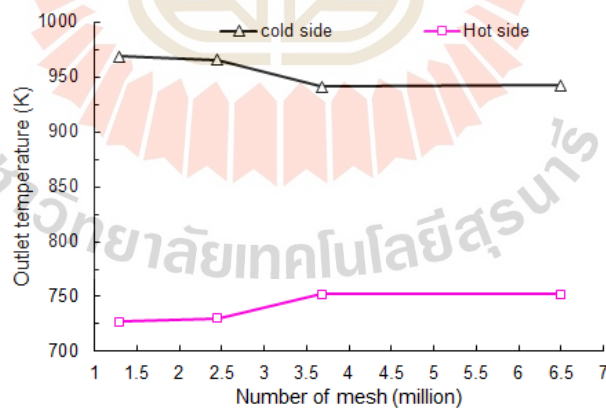
$$\varepsilon = \frac{T_{h,outlet} - T_{h,inlet}}{T_{h,inlet} - T_{c,inlet}} \quad (3.15)$$

In Eq.(3.13), $\dot{m} C_p$ is the heat capacity rate of the fluid of interest (C). If $C_{min} = C_c$, the equation can be expressed as in Eq. (3.14). This can be interpreted as the “temperature effectiveness” for cold fluids. If the minimum capacity fluid changes from cold to hot, as $C_{min}=C_h$, then the effectiveness is defined by Eq. (3.15).

3.4 Mesh Convergence Study for Zigzag Channel PCHes Analysis



(a) Pressure drop



(b) Outlet temperature

Figure 3.2 Mesh independency study.

Four different meshes were configured to determine the suitable number of mesh grid points. The mesh numbers from 1.3 million to 6.5 million. The outlet temperature and pressure drop of the fluid on both sides were determined to compare

the mesh simulation results, aiming to predict accurate results and reduce computational time. When mesh number is 3.678 million and the y^+ is lower than 2, both the outlet temperature and the pressure drop converge with refining the mesh grid number, as shown in Figure 3.2. The simulation considered 3.678 million elements for the numerical model was reliable and saved computational time. In comparison, outlet temperature on cold side was higher than the hot side. In a counter flow heat exchanger, the cold fluid continuously encounters progressively hotter sections of the hot fluid, allowing it to absorb heat efficiently along its flow path. This design enables the cold fluid to outlet at a higher temperature than the hot fluid's outlet temperature (Cengel & Ghajar, 2020). The 3.678 million mesh generation of the computation domain is illustrated in Figure 3.3.

3.5 Model Validation for Zigzag Channel PCHEs Analysis

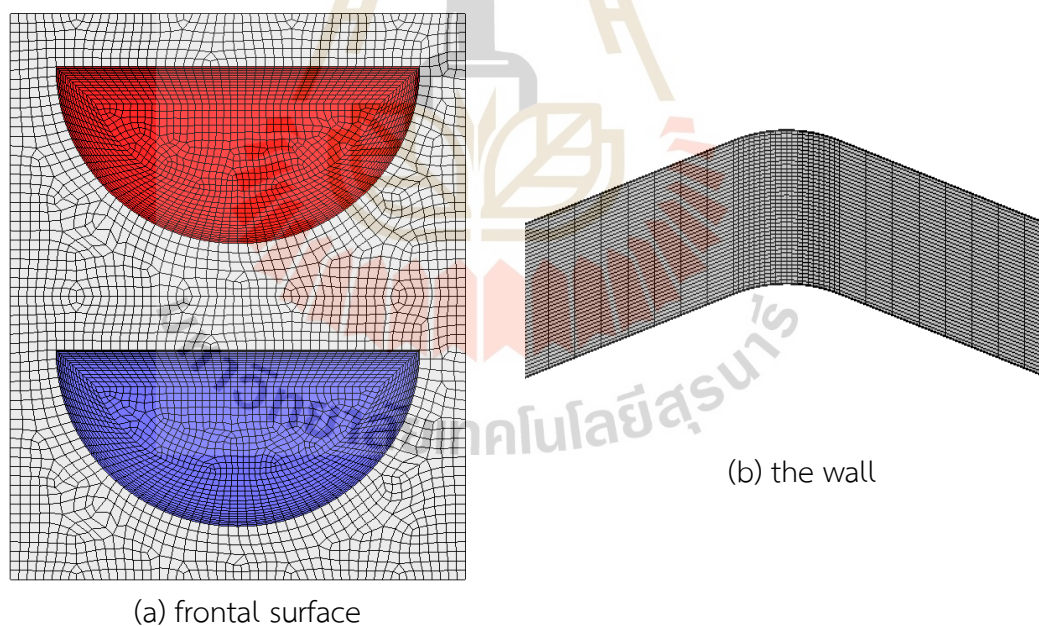


Figure 3.3 Mesh generation (3.678 million) of the computational domain.

The validation for the CFD model was carried out by three different channels, comparing with theoretical and published work at Reynolds number (Re) less than

2,300. The numerical model was set up laminar model, steady state condition. In this work, a simple flow of the circular channel PCHE was considered, utilizing basic experimental geometric values with a channel diameter of 2.0 mm and a channel length of 272 mm (Mylavarapu, 2011). However, the flow length considered is significantly greater than the length required for the flow to become hydrodynamically fully developed (Mylavarapu et al., 2014). Therefore, the length of the circular channel was considered to be 372 mm in this simulation. The geometry of the semicircular channel PCHE was assumed to have the same cross-section as in (Mylavarapu et al., 2014). In their experiment, the experimental channel length contacted along the flow was 305 mm between the hot and cold sides. The geometry of the straight semicircular channel is shown in figures A.3 and A.4. Consequently, the simulation channel length was considered to be 305 mm on both sides. In the zigzag channel simulation, Chen et al.'s (Chen et al., 2019) rounded edge channel and In Hun Kim et al.'s (Kim et al., 2009) sharp-edged channel models were used to verify the zigzag channel PCHE.

3.5.1 Circular Channel Validation

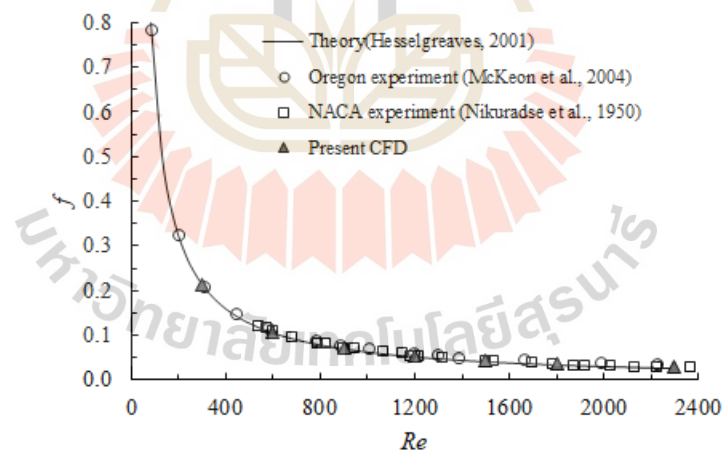


Figure 3.4 A simple flow analysis for a straight circular channel PCHE.

Figure 3.4 illustrates the Fanning friction factor as a function of the simple flow Reynolds number. For the circular channel validation, mesh numbers ranging from 0.54 million to 3.2 million were tested. After testing for mesh convergence, 2.7 million mesh was found to have reached the convergence level and

was used for the validation. The present CFD results of a circular channel were observed very well with theoretical (Hesselgreaves, 2001), but were lower compared to experimental data (McKeon et al., 2004; Nikuradse, November 1950). The CFD model assumed a uniform flow distribution at the inlet, a smooth wall, and was based on a core section. The experiment channel may not be perfectly smooth because of imperfect manufacturing and tolerances. In addition, the real flow may not be uniformly distributed due to the header and different path lengths. This introduces an error between CFD results and experimental results.

3.5.2 Semicircular Channel Validation

Figure 3.5 shows the comparison of the Nusselts numbers and the pressure loss factors for the semicircular channel. In validation, mesh numbers ranging from 0.3 million to 4.01 million were tested. After testing for mesh convergence, 2.51 million mesh was found to have reached the convergence level and was used for the validation. The maximum difference is around 20% in Nusselt's number, and below 10% for the pressure loss factor between experimental (Mylavarapu et al., 2014) and CFD results. Since the shape of the duct cross-section is sensitive to the pressure loss factor in laminar flow, uncertainty is produced in the results calculated from the experimental data because the geometry is not perfectly semi-circular.

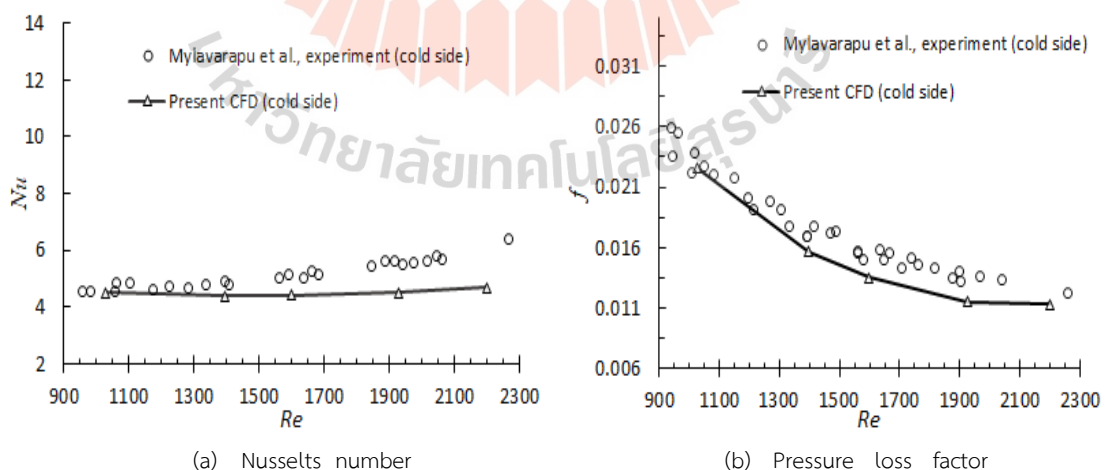


Figure 3.5 Analysis for a straight semicircular channel PCHE.

3.5.3 Zigzag Channel Validation

In zigzag channel simulation, using 6 million mesh number was determined for a In Hun Kim CFD model. In Figure 3.6, the comparison of Nusselts number results shows that the present CFD results exhibit a good agreement about 7% with In Hun Kim et al.'s experimental data (I. H. Kim et al., 2009) and with Chen et al.'s experimental data about 10% average error (Chen et al., 2019).

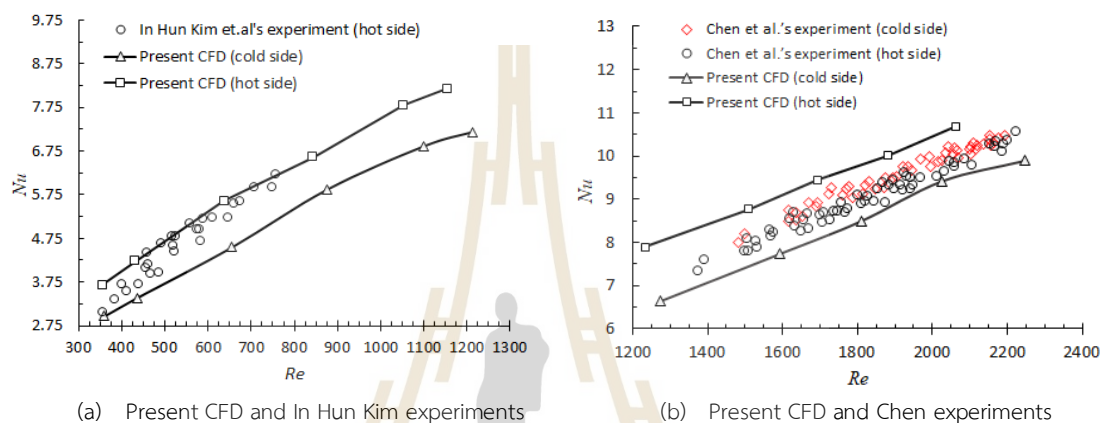


Figure 3.6 Comparison of global Nusselt number.

The global pressure loss factor comparison between the current simulation results and experimental results are shown in Figure 3.7. The present CFD results exhibited average deviation about 15% with In Hun Kim experiments (Kim et al., 2009). The average deviation between the present simulation and Chen et al.'s experimental results were mostly within an average range of 12% on the cold side and 20% on the hot side. The simulation model was only considered an ideal model for the core of a PCHE with smooth channel walls. However, the experimental results included the effects of the header and plenum features within the flow passage. Moreover, the smaller cross-sectional area and the shape of the channel likely contributed to the conflict between the measured data and model prediction. Furthermore, the differences in the friction factor values between the simulation and experiment were within the acceptable ranges defined in the literature (Li et al., 2020; Yih & Wang, 2020).

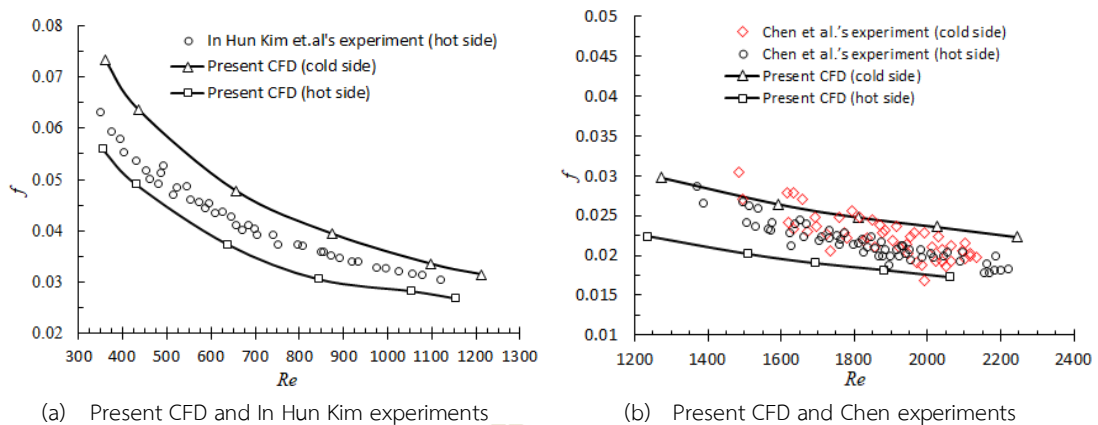


Figure 3.7 Comparison of global pressure loss factors.

In validation section, the present CFD is enough for bending channel angle analysis. Although the present CFD results deviate from the experiments, that may from experiments include some uncertainty. If assume perfect smooth wall, the present CFD model is strongly enough for analysis by the proof of Figure 3.4.

3.6 Model Preparation and Boundary Conditions for PCHE Evaporation

This section outlines the steps taken to prepare the computational model and establish the necessary boundary conditions for simulating the evaporation process within the printed circuit heat exchangers (PCHEs). The preparation of the computational model and establishment of boundary conditions are crucial steps in simulating the evaporation process within the PCHE. By defining the geometry, mesh, and boundary conditions accurately, it ensure a reliable and efficient simulation of heat transfer and fluid flow phenomena. Next chapter presents the simulation results, offering a detailed examination of heat transfer phenomena, fluid flow characteristics, and the overall performance of PCHEs during evaporation.

This study conducted the experimental parameters of straight channel PCHE using two-phase nitrogen working fluid (Shi et al., 2020). The experiment used different inlet conditions for the hot and cold sides: two-phase for the cold and gas phase for the hot. The hot and cold sides had distinct plates, with straight-channel and N-type-channel designs, respectively. Both sides featured aligned channels within the core,

with a 446 mm length for core heat transfer. Therefore, the two-phase flow numerical 3D model channel length was considered 446 mm, and the semi-circular channel diameter was 0.884 mm. Real PCHE systems use a single inlet and outlet nozzle to distribute fluid across multiple microchannel. Inlet and outlet header designs, fluid states, and channel patterns can lead to maldistribution (Shin & Yoon, 2020). Simulations based on a single channel may not reflect actual outcomes due to these complexities. Performing simulations for all channel is very time-consuming, especially for diverse cases. Software limitations exist for simulating the nitrogen phase change from liquid to gas. PCHE's alternating cold and hot layer arrangement leads to a periodic boundary condition. Assuming uniform heat loss, the majority of heat from hot-side channels transfers to cold-side channels. Therefore, the present simulation was considered a single-channel PCHE, as shown in Figure 3.8. For the boundary condition, the computational model set three types of surfaces: inlet mass flowrate, outlet pressure drop, and heat wall. In simulation, a single-straight channel geometry was tested for model verification and evaporation flow visualization. The model was verified by using both cold (liquid) nitrogen and hot (vapour) nitrogen. Therefore, the heat wall boundary conditions were a heat source wall used on the cold side and a heat sink wall used on the hot side.

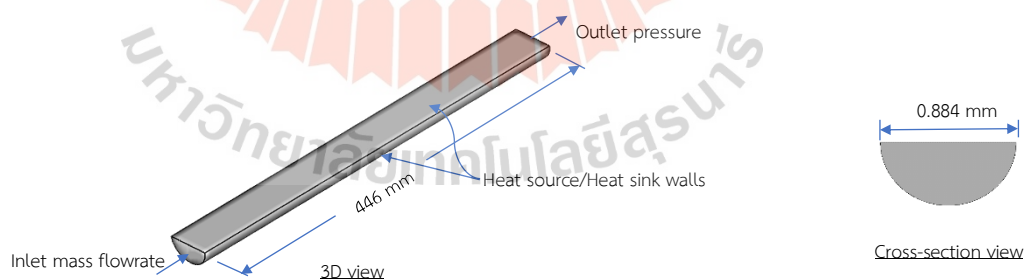


Figure 3.8 A single-channel PCHE geometry and boundary conditions.

3.7 Numerical Simulation Method of Multiphase Flows

This paper utilizes the Volume of Fluid (VOF) model to analyze phase-to-phase interactions between fluids, including mass, momentum, and energy transfers at the

interphase. In the VOF model, computational cell of volume fractions for each phase are recorded. All phases of volume fractions sum to unity (Hasanpour et al., 2018).

$$\alpha_l + \alpha_g = 1 \quad (3.16)$$

Where α_l represents the volume fraction of the liquid phase and α_g is for vapor phase, respectively. The conservation equations are employed to track the surface between these phases, and the equations are computed for the volume fraction of each phase. The continuity equations for each phase can be understood as:

$$\frac{\partial \alpha_l}{\partial t} + \nabla \cdot (\vec{u} \alpha_l) = \frac{-S}{\rho_l} \quad (3.17)$$

$$\frac{\partial \alpha_v}{\partial t} + \nabla \cdot (\vec{u} \alpha_v) = \frac{-S}{\rho_v} \quad (3.18)$$

Where S represents the mass transfer rates due to phase change, expressed in $\text{kg}/(\text{m}^3 \cdot \text{s})$. Based on the Navier-Stokes formulations and the interfacial two-phase flow, a momentum transport equation is present in cells for the two phases. This equation depends on the volume fractions of all phases, and it must also consider the force caused by surface tension at the interface.

$$\frac{\partial}{\partial t}(\rho \vec{u}) + \nabla \cdot (\rho \vec{u} \vec{u}) = -\nabla p + \nabla \cdot [\mu(\nabla \vec{u} + \nabla \vec{u}^T)] + \rho \vec{g} + \vec{F}_\sigma \quad (3.19)$$

In this context, \vec{F}_σ defines the volumetric surface tension force, applying the Continuum Surface Force (CSF) model introduced by Brackbill et al. (Brackbill et al., 1992). Here, \vec{u} is the velocity field, p stands for pressure, and F represents the gravitational force.

$$F_\sigma = \sigma \frac{\alpha_l \rho_l k_g \nabla \alpha_g + \alpha_g \rho_g k_l \nabla \alpha_l}{0.5(\rho_l + \rho_g)} \quad (3.20)$$

Where the interfacial surface tension between the phases symbols as σ (N/m) which can be expressed in terms of the pressure jump across the surface, acting as the source term in the momentum equation. ρ_l and ρ_g denote the liquid density and vapor density, while k_l and k_g represent the curvatures of the liquid and vapor phases, respectively. To adjust the body force term in the surface tension, the curvatures of the phases use in calculation which can be defined as,

$$k_l = \frac{\nabla \alpha_l}{|\nabla \alpha_l|}, k_g = \frac{\nabla \alpha_g}{|\nabla \alpha_g|} \quad (3.21)$$

As the previous discussion, the VOF model simulates the movement of distinct phases by tracing the interface's motion across the entire solution domain. The continuity equation is employed to solve for the volume fraction of each phase, thereby tracking the interface between the phases. This approach accounts for situations where a control volume is not entirely occupied by a single phase.

The energy equation, shared between the liquid and vapor phases can be defined as follows:

$$\frac{\partial}{\partial t}(\rho E) + \nabla \cdot [\vec{u}(\rho E + p)] = \nabla \cdot (k_e \nabla T) + \dot{Q} \quad (3.22)$$

The equation involves the shared temperature field, denoted as T , along with the enthalpy represented by E . And the effective thermal conductivity, k_e , plays a crucial role in the equation. Additionally, the term \dot{Q} (W/m^3) incorporates the heat transfer rates occurring through the interface.

$$E = \frac{(\alpha_l \rho_l E_l + (1 - \alpha_l) \rho_g E_g)}{(\alpha_l \rho_l + (1 - \alpha_l) \rho_g)} \quad (3.23)$$

$$k_e = \alpha_l k_{e,l} + (1 - \alpha_l) k_{e,g} \quad (3.24)$$

In which the values of E_l and E_g are determined based on the specific heat of liquid and vapor phases demonstrated by:

$$E_l = C_l (T - 298.15), E_g = C_g (T - 298.15) \quad (3.25)$$

3.7.1 Mass Source Term



Figure 3.9 A cross-sectional view of the channel's polyhedral mesh for the PCHE model.

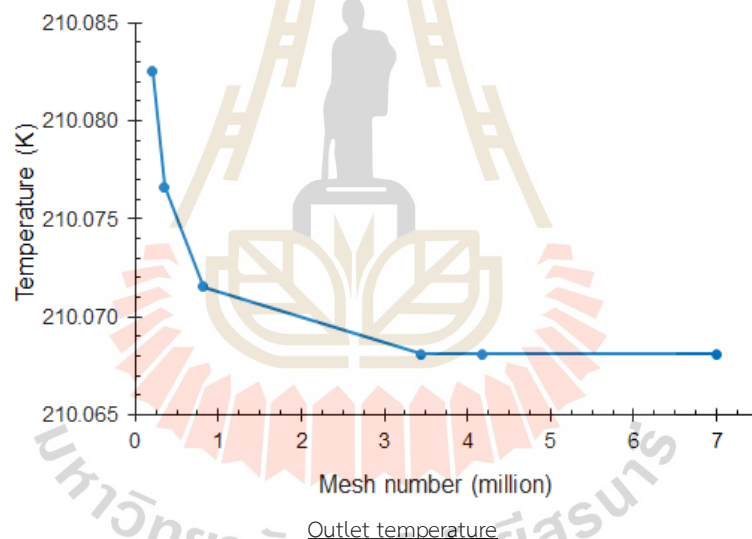
To simulate the evaporation and condensation processes, a mass transfer model based on Lee (1980) and is adapted. In this model, the phase change is represented by a mass source term, which is primarily influenced by constant pressure and the saturation temperature. If the saturation occurs at $T \geq T_{sat}$, the evaporation process takes place. During this process, the mass of the liquid phase decreases, while the mass of the vapor phase increases within the control volume. The magnitudes of mass source term are:

$$S = c_l \alpha_l \rho_l \frac{T - T_{sat}}{T_{sat}} \quad (3.26)$$

$$S = c_g \alpha_g \rho_g \frac{T - T_{sat}}{T_{sat}} \quad (3.27)$$

When the saturation occurs at $T < T_{sat}$, it occurs the condensation process meanwhile the mass of the liquid phase increases and the mass of vapor phase decreases in the control volume respectively.

To ensure a satisfactory numerical convergence of the interfacial temperature at T_{sat} , the empirical coefficients c_l and c_g are needed to be fine-tuned and can be expressed as a time relaxation parameter with unit 1/sec. Large c_l and c_g values cause convergence issues, while small values lead to a significant deviation between the interfacial temperature and the saturation temperature. In this study, the value of c_l and c_g are set equal to 10 s^{-1} which has the best convergences solution of continuity and energy equations with the minimum deviation from saturation temperature at the interface.



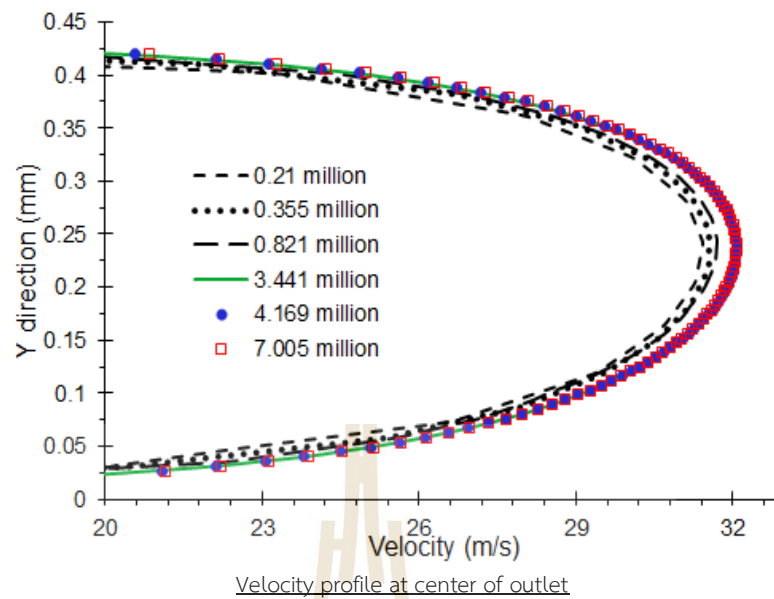


Figure 3.10 Shows the grid sensitivity test for CFD simulation convergence.

3.7.2 Heat Source Term

The evaporation and condensation mass transfer source terms are developed from the heat transfer source term. This enables the direct definition of the heat transfer source as:

$$\dot{Q} = h_g \cdot S \quad (3.28)$$

where h_g represents the latent heat, J/kg.

3.8 Mesh Grid Sensitivity Test for PCHE Evaporation Model

The 3D numerical simulation was carried out using the ANSYS Fluent program. A mesh grid convergence study was conducted under steady-state conditions vapor nitrogen. Polyhedral elements were used to mesh the numerical model, as shown in Figure 3.9. Six sets of grid numbers were simulated and compared, considering an inlet mass flowrate of 1001.5 kg/hr, inlet temperature of 288.45 K, inlet fluid pressure of 0.82 MPa and a heat sink of -25.6 kW of the entire PCHE channels. The outlet pressure was set up zero in simulation. The continuity, momentum, and energy governing

equations were solved using the SST k-omega turbulence model and the Semi-Implicit Method for Pressure-Linked Equations (SIMPLE). Thermo-physical properties, influenced by temperature and pressure, were sourced from NIST chemistry webbook and implemented in the program using a piecewise-linear approach. The outlet temperatures and velocity profiles from the numerical simulations using six different grid numbers were compared, as depicted in Figure 3.10. Ultimately, a grid with over 3 million elements was chosen for its accuracy and efficiency in the subsequent study. The decision on the optimal number of elements was based on 3.441 million the element size.

3.9 Numerical Model Verification for PCHE Evaporation Model

An experimental data was carried out to verify the numerical model PCHE, using nitrogen (N₂) as liquid fluid and gas fluid, respectively (Shin & Yoon, 2020). The verification considered both steady and transient experimental conditions. The experimental PCHE was designed for industrial-scale use with a capacity of up to 50 kW as a recuperator on a floating storage regasification unit (FSRU). This experiment analyzed the flow rate effect of the hot side on the PCHE, which holds particular importance in the thermal and hydraulic analysis of the PCHE. Moreover, in an effort to minimize heat loss or gain, the experiment included three additional cases under single-phase conditions. The recorded data on outlet pressure and temperature was used to calculate the effective heat transfer. In the present study, steady-state numerical analysis was employed to investigate the impact of flow rate variations on the hot side. Additionally, heat loss experiments were conducted as part of the current numerical evaporation transient analysis. The experimental data used for the verification of the numerical model through the equation below (Shin & Yoon, 2020):

$$\text{Absolute percent error} = \left| \frac{(T_{CFD} + 273.15) - (T_{Exp} + 273.15)}{(T_{Exp} + 273.15)} \times 100\% \right| \quad (3.29)$$

3.9.1 Steady State Condition

To validate the simulation, outlet temperatures were measured. The hot side operated under steady-state vapor conditions. The inlet mass flowrate of the entire PCHE model varied from 531.5 kg/h to 1001.5 kg/h. The inlet temperatures and pressures are 288.45–288.95 K and 0.82-0.83 MPa. The heat sink ranged from -25.6 kW to -27.5 kW. The present results showed good agreement, as shown in figure 3.11, compared with experimental results (Shin & Yoon, 2020).

3.9.2 Transient State Condition

The cold side simulated for analysis of transient two-phase (vapor-liquid) conditions. For case 1, the inlet mass flowrate of the entire PCHE model, temperature, pressure, and heat source were 213 kg/hr, 102.05 K, 1.35 MPa, and 18.2 kW. In case 2, these values were 205.1 kg/hr, 102.85 K, 1.59 MPa, and 20.6 kW. The time step was chosen to ensure a Courant number lower than 1 and ranged from 0.01 to 0.00001 seconds. In the simulation, the inlet was specified as a fully liquid condition. The numerical simulation presented in this study exhibited excellent agreement with experiments, with an absolute error of less than 2% in figure 3.12. Thus, the outcomes of this study can be validated.

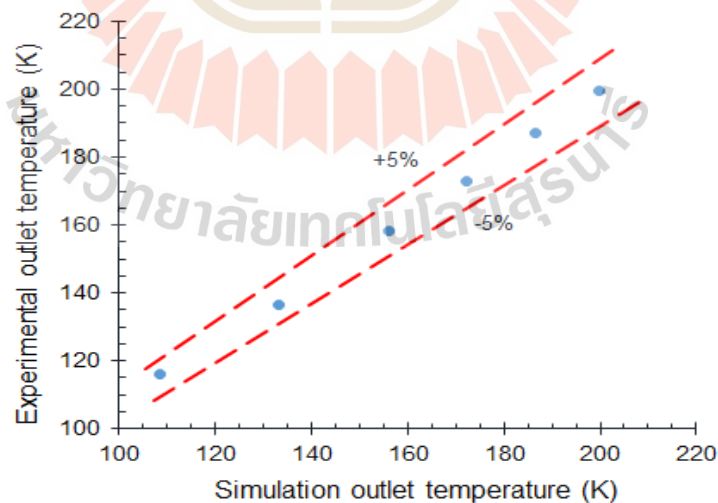


Figure 3.11 Comparison between experimental and simulation results under steady state condition (hot side).

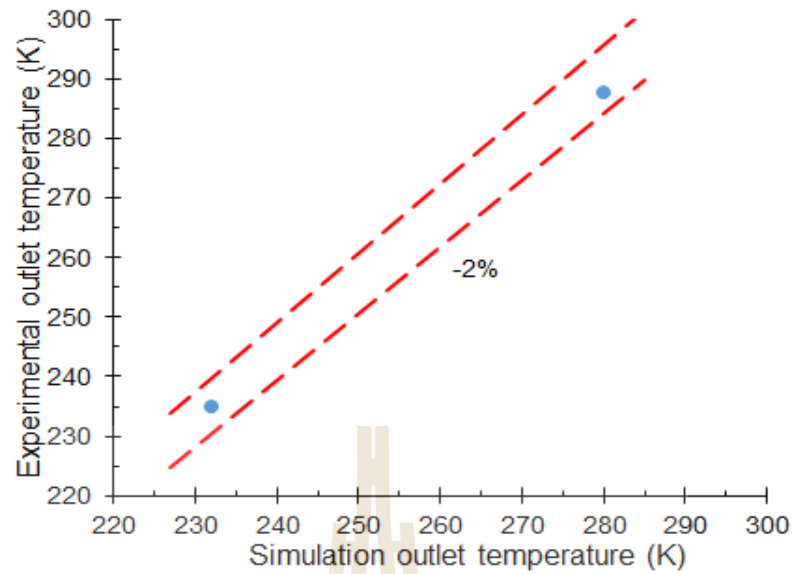


Figure 3.12 Comparison between experimental and simulation results under transient condition (cold side).

3.10 Case Study Simulation of Channel Structure Effects On Thermal Hydraulic Performance of PCHE

The primary objective of this case study is to conduct a comprehensive numerical investigation into the effects of channel structure variations on the thermal hydraulic performance of PCHEs. By simulating different channel geometries, flow velocities, and operating conditions, we can identify optimal configurations that maximize heat transfer rates while minimizing pressure losses.

3.10.1 Setting up Numerical Models and Simulation Method

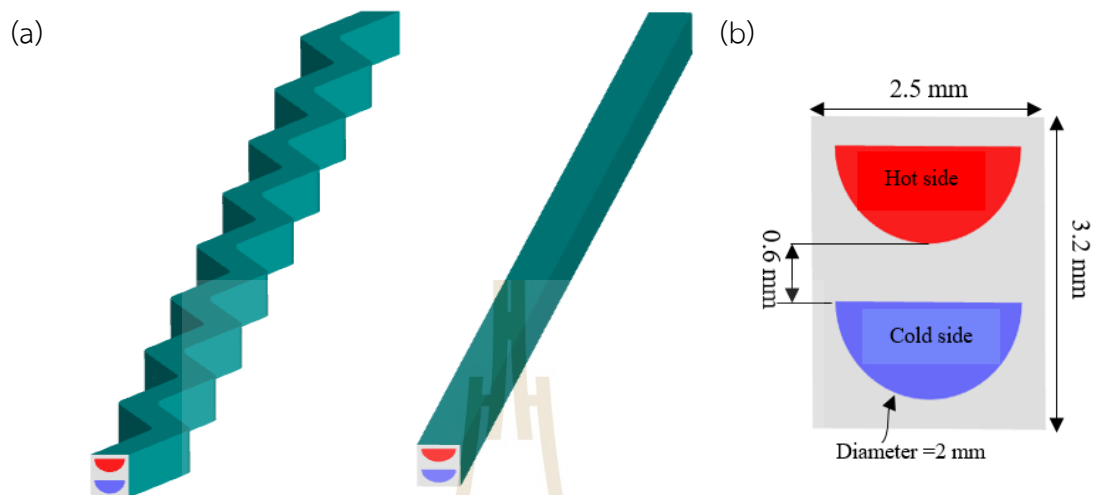


Figure 3.13 (a) 3D models of zigzag and straight channels. (b) Cross-sectional view of simulation domain.

For the numerical model, Chen et al. (Chen et al., 2019) 15° zigzag channels with round corners (fillet radius = 4 mm) and straight channel used. For simulation, Ansys fluent commercial software was used. The counter-flow channels with a cross-section are shown in Figure. 3.13. The cold side is blue, the hot side is red, and the solid material is shown in gray in Figures 3.13 (a) and (b). To reduce computational resources and time, a numerical model was set up as a single banking method. The top, bottom, left, and right positions were set as the periodic boundary conditions. The entire channel length was divided into 8.5 pitches. A pitch length was 24.6 mm. For the simulation, the numerical models were set to the steady-state condition, inlet mass flow rate, and pressure outlet. The inlet temperatures on the cold and hot sides were 623.15 K and 1073.15 K, respectively, and the outlet and working pressures were 3 MPa on both sides. Supercritical helium was used as working fluid. The thermal-physical of helium properties depend on temperature and pressure and have been imported from the NIST chemistry webbook (NIST, 2023). The ANSYS Fluent commercial software was used to perform the simulation. The average

Reynolds number (Re) angel was considered lower than 2300. Therefore, the simulation employed steady state and laminar model. For the coupling of velocity and pressure, the simple algorithm was set up. To solve the momentum and energy, a second-order upwind scheme was used for accurate results.

3.10.2 Grid Independence and Model Validation

Table 3.1 Mesh grid independency simulation results.

Mesh (million)	T_{outlet} (K)		ΔP (kPa)	
	Cold side	Hot side	Cold side	Hot side
0.124	938.22	757.62	14747.7	15384.8
1.95	954.36	740.06	15324.5	16091.5
3.123	947.10	748.80	15947	16578.1
4.87	948.78	747.00	15350	16000

As shown in Table. 3.1, four mesh-grid elements were studied: 0.124, 1.95, 3.123, and 4.87 million. The mesh grids were generated in the ANSYS Mesh software. For the mesh-independence study, an inlet mass flow rate of approximately 9.7857×10^{-5} kg/s per channel in both channels was simulated. The outlet temperature and pressure drop were measured. To determine the appropriate mesh grid, the fine mesh results were used to calculate the relative error. In comparison, a grid number of 0.124 million showed about up to 3.924% on pressure drop and 1.422% an outlet temperature with the fine mesh results. When the mesh grid number was greater than 1.95 million, the maximum relative error was approximately 0.928% for the outlet temperature and 3.889% for the pressure drop, which is the safety percentage error. Therefore, a grid number of 1.95 million was suitable for saving computational time and obtaining accurate results. For model validation, the Reynolds number test was simulated, and validated using the results of Chen et al. (Chen et al., 2019). The validation is shown in Figure 3.14. The present simulation has some discrepancies of up to 5% with Chen et al.'s simulation, 31% with the experimental

results for the Fanning friction factor, and 10% and 2% for the Nusselt number. Thus, the zigzag channel PCHE model was strongly validated for use in numerical studies.

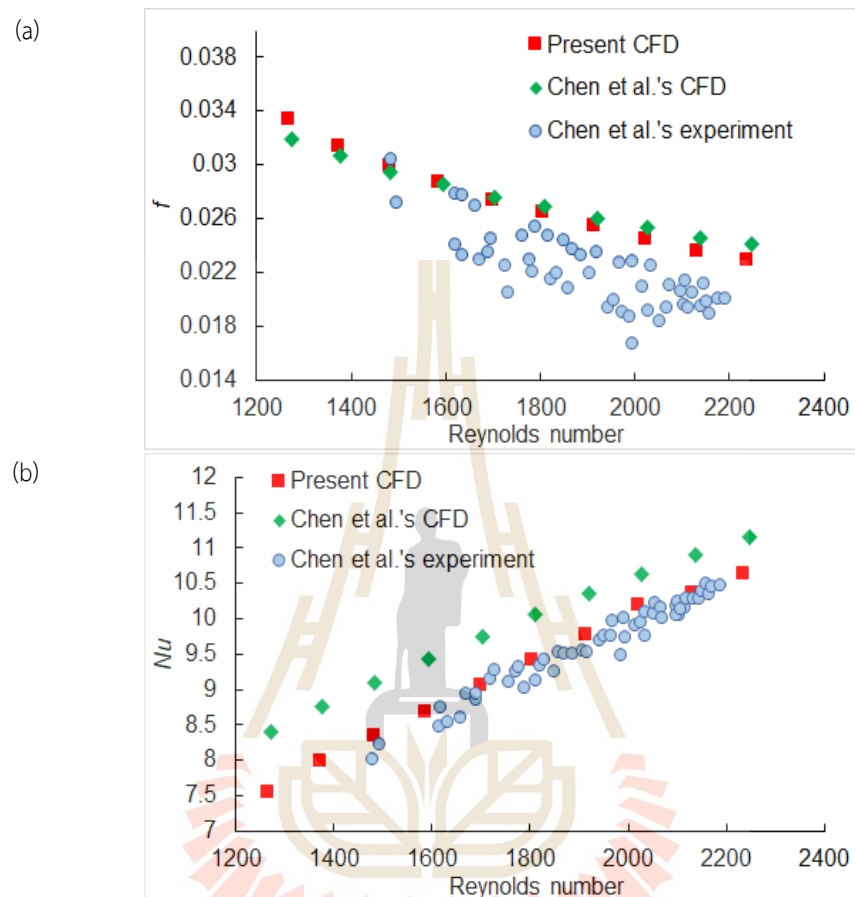


Figure 3.14 Global Fanning friction factor (f) comparison, and global Nusselt number (Nu) comparison.

3.10.3 Relation Between Channel Structure and Thermo-Physical Properties

The variation of thermo-physical properties depending on channel structure was studied at mass flow rate 8.515×10^{-5} kg/s simulation. In order to focus on the channel structure's effect, the channel's full length was considered equal pitch length (8.5 pitches) and the same inlet mass flowrate on both sides.

The variation absolute velocity in the cold channels are shown in Figure 3.15. It was found that the straight channel was no flow disturbance since it didn't have a bend corner. However, the zigzag channel exhibited flow separation around

the corner. The flow moved from the inner curvature to the outer curvature of the wall. The flow curvature induced an intensive centrifugal force that created the flow separation. In addition, at the inner wall, a reverse pressure gradient is generated, leading to the holding of the secondary flow zone, creating a vortex and increasing the pressure drop (Hong et al., 2017).

As shown in Figure 3.16, the temperature distribution in all channels increases from the wall to the fluid over the flow distance. The temperature distribution of the zigzag channel exhibited more significant variation than that of the straight channel. These results indicate that the curvature channel significantly influences the heat transfer. The flow channel asymmetry can be attributed to local heat flux changes after passing through a corner (Kim et al., 2008). Therefore, the temperature distribution of the zigzag channel was not uniform.

Figure 3.17 shows the streamline distribution at corner of the pitch number ($N = 8$). The straight channel exhibited no vortices resulting from the absence of a flow disturbance. In the zigzag channel, vortices are produced at the bending point. This is because the flow disturbance at the outer wall was separated from that at the inner wall. A secondary flow is generated by the flow separation, which significantly enhances the heat transfer, mixing fluid, and accelerating core displacement (Pan et al., 2020). These secondary flows indicate efficient cross-sectional fluid mixing, non-uniform temperature profiles, and a high heat-transfer rate.

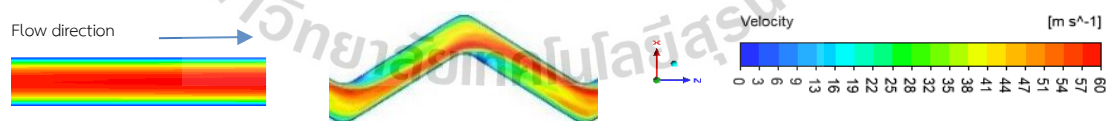


Figure 3.15 Velocity distribution of straight and zigzag channels at pitch number ($N = 8$).



Figure 3.16 Temperature distribution of straight and zigzag channels at pitch number (N = 8).

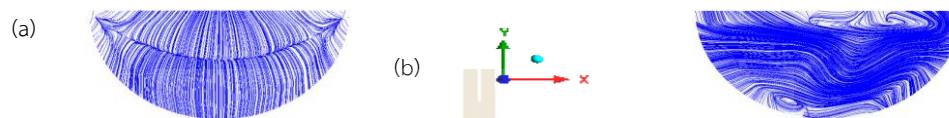


Figure 3.17 Streamlines distribution at a pitch number (N = 8) (a) straight and (b) zigzag channel.

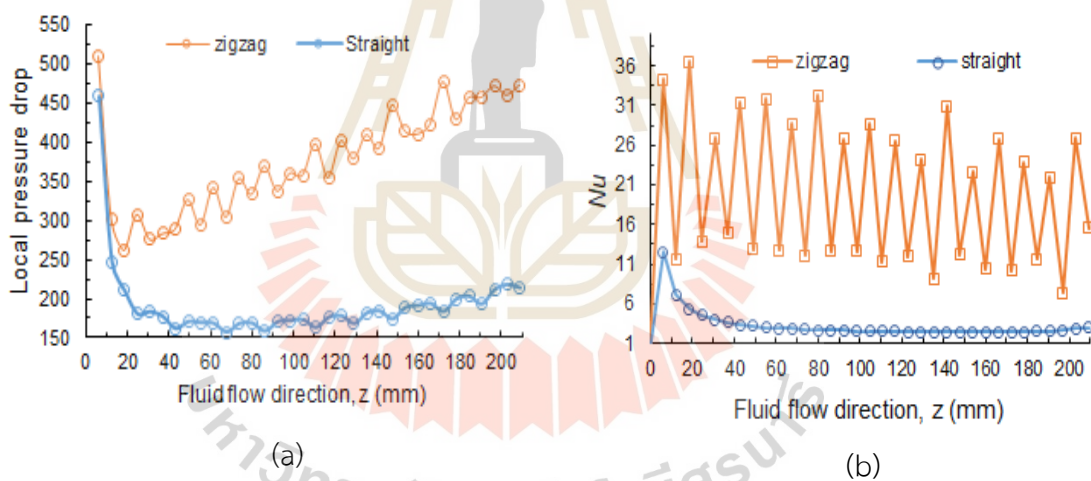


Figure 3.18 (a) Local pressure drop and (b) local Nusselt number along flow direction.

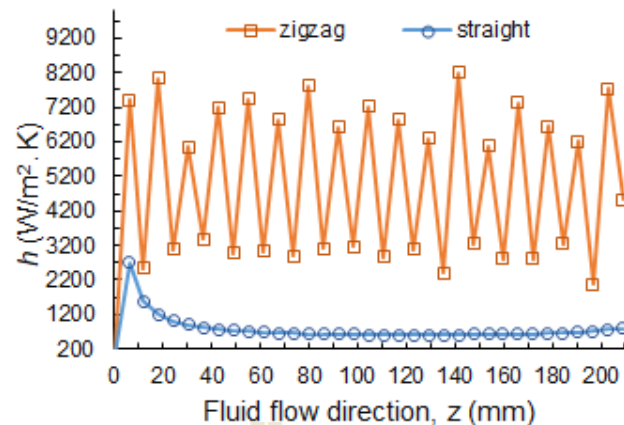


Figure 3.19 Local convective heat transfer coefficient along the flow direction.

As shown in Figure 3.18a, the zigzag channel exhibited a higher pressure drop than the straight channel. The secondary flow in the zigzag channel was significant, as shown in Figures 3.15 and 3.17, which led to an increase in pressure drop. The long length of the flow path also increased the pressure drop. In Figure 3.19, the zigzag channel has a higher heat transfer coefficient than the straight channel over the flow distance, resulting from the high heat-transfer rate (Figure 3.16) and the actual flow area. The result of secondary flows with large vorticity structures (Figure 3.15 and 3.17) significantly affects the fluid mixing and convective high heat-transfer rates. Therefore, the zigzag channel showed a significant heat transfer coefficient. Figure 3.18(b) shows the local Nusselt number (Nu), which is similar to the convective heat-transfer coefficient. The Nusselt number of the zigzag channel was larger than that of the straight channel. Because of the higher thermal energy transported by the hot surface, the viscosity and thermal conductivity were lower, the thinned film thickness and the higher convective heat-transfer coefficient, leading to a larger local Nu . As shown in Figure 3.20, the local heat flux of the zigzag channel appears obviously non-uniform on the wall and significantly increased on the windward side of the channel corner. It is because incoming mainstream impacts on the windward sides and changes the flow direction, which leads to shifting the high heat flux zone and fluctuating the local Nusselt number.

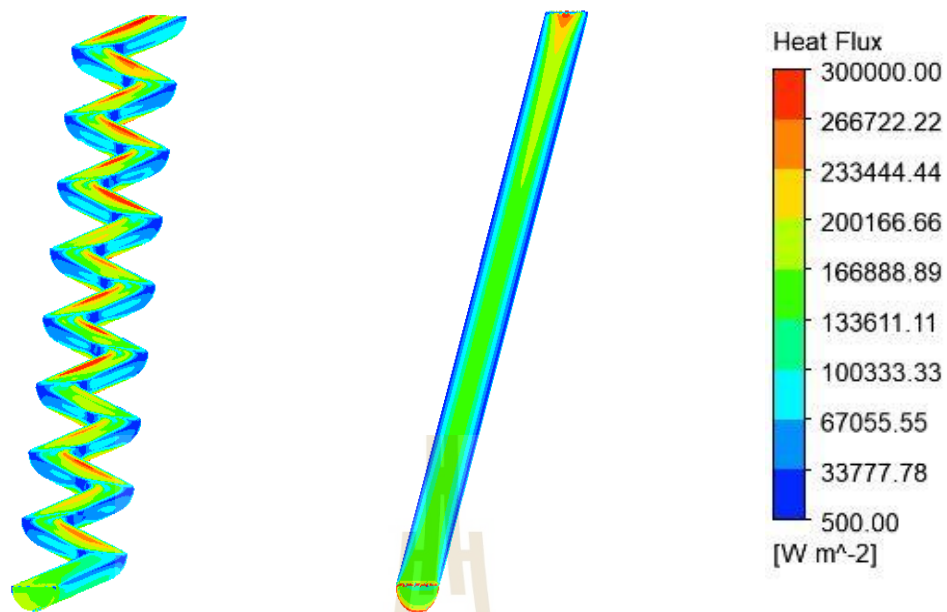


Figure 3.20 Local heat transfer coefficient of the zigzag channel and straight channel

3.10.4 Mass Flow Rate Effect on the Channels

From the mass flow rate 8.515×10^{-5} kg/s simulation, the channel shapes significantly affected the local flow and thermal performance. Therefore, the mass flow rate is one of an important parameter for analysis of PCHE performance. A different mass flow rate from 5.108×10^{-5} kg/s to 8.515×10^{-5} kg/s was applied to the global thermal-hydraulic performance of PCHE analysis.

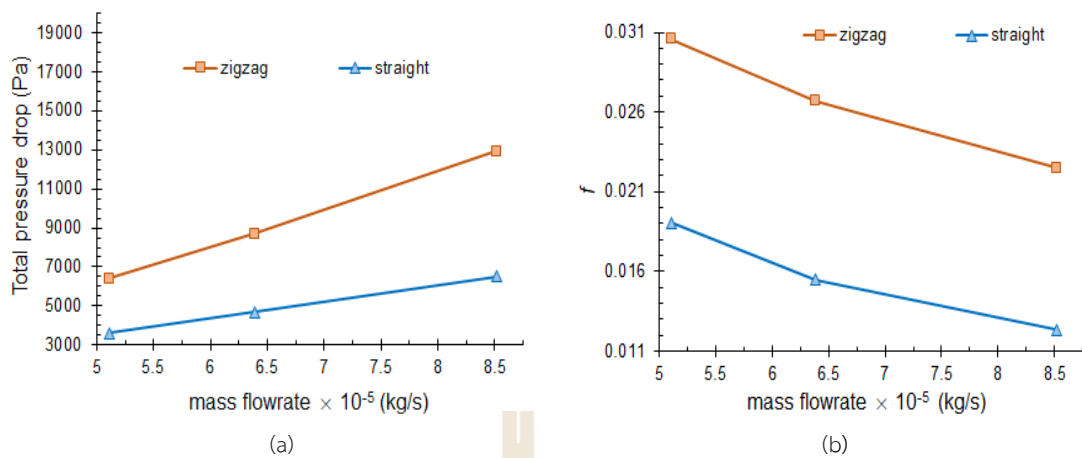


Figure 3.21 (a) Total global pressure drop, and (b) global Fanning friction factor at different mass flow rates for different channels.

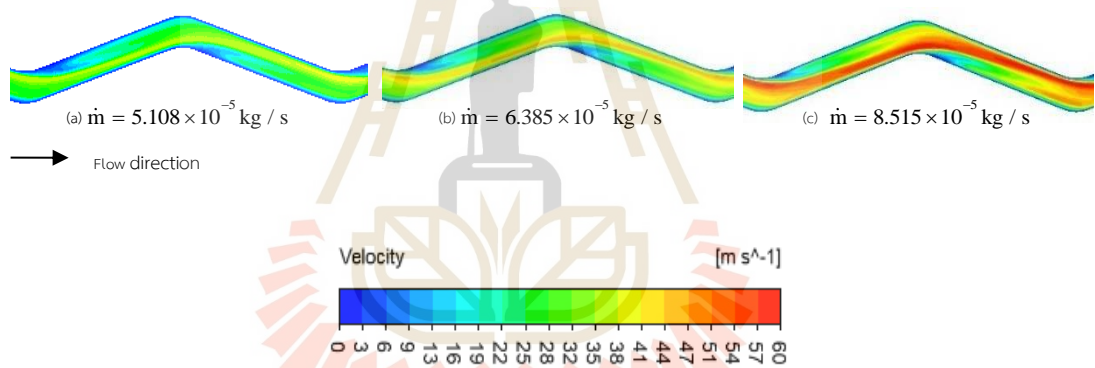


Figure 3.22 Velocity magnitude distribution for $N_p = 8$ at different mass flow rates.

As shown in Figure 3.21 (a), the largest total pressure drop was found in the zigzag channel due to the long length of flow channel. In addition, the zigzag channel changed the fluid flow direction at the corner, causing flow separation and vortices, which increase the pressure drop. The pressure drop in the two channels increased with increasing mass flow rate owing to the increase in the fluid velocity, as shown in Figure 3.22. The friction loss when the fluid passes through the channel is shown in Figure 3.21 (b) using the dimensionless value of Fanning friction factor. A higher mass flow rate reduced the Fanning friction factor by about 54% in a straight channel and 36%

in a zigzag channel compared to a lower mass flowrate. According to equation (3.6), there is an inversely proportional relationship between f and the mass flow rate square. However, the zigzag channel of the Fanning friction factor was predicted to be up to 45% higher than a straight channel. Figure 3.23(a) shows the global Nusselt number.

The same trends of h and Nu increase with increasing mass flow rate owing to an increase in the channel surface heat flux. A higher global Nusselt number was observed in a zigzag channel up to 55% than in a straight channel because of the heat absorbed from the hot solid by the fluid per unit volume, resulting in an increase in the temperature on the cold side, the thermal conductivity decreasing, and Nu increasing.

Between straight and zigzag channel effect analysis, the simulation considered a full-length channel of 8.5 pitches with a pitch length 24.6 mm and the same cross-section area of $1.57 \times 10^{-6} \text{ m}^2$. However, the actual flow length was a zigzag channel of 216 mm and a straight channel of 209 mm. Therefore, the criterion $\zeta = (Nu / Nu_0) / (f / f_0)$ was applied to investigate the pressure drop and heat transfer performance for a given pumping power (Pan et al., 2020; Shi et al., 2019; Wang et al., 2021). Where the subscript 0 represents the comprehensive minimum performance value of the straight channel at a mass flow rate of $5.108 \times 10^{-5} \text{ kg/s}$ as a basis. The zigzag channel showed a higher comprehensive performance of about 16% at low mass flowrate and 22% at high mass flowrate simulation than the straight channel, as shown in Figure 3.23(b). Therefore, the zigzag channel provided better heat transfer performance than flow losses.

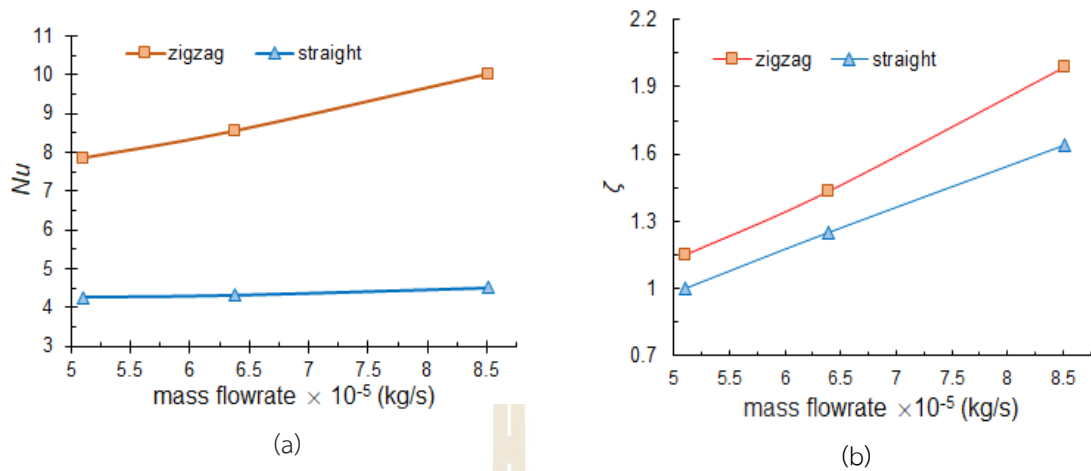


Figure 3.23 (a) Global Nusselt number and (b) comprehensive performance evaluation index (ζ) at different mass flow rates for zigzag and horizontal channels.

3.10.5 Mass Flow Rate Effect on the Channels Effect of Zigzag Channel Diameter on The PCHE Performance

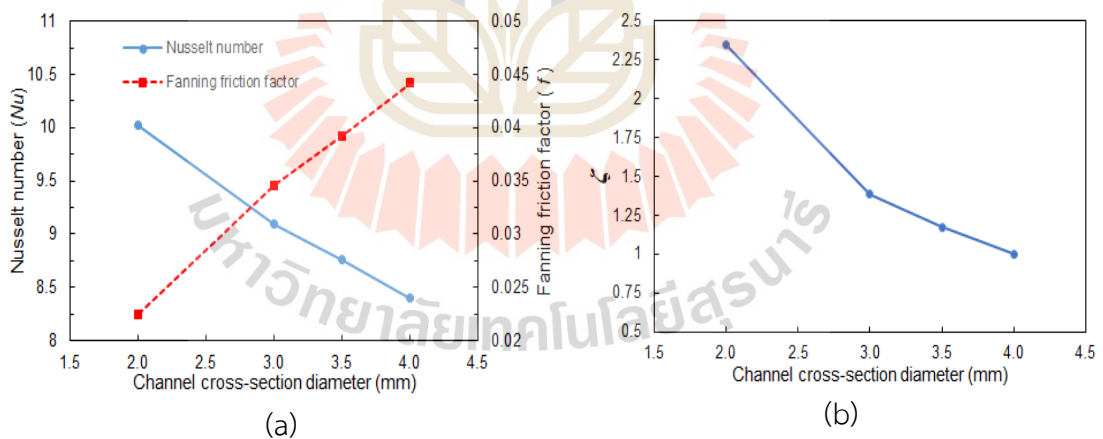


Figure 3.24 Effects of channel diameter analysis (a) Global Nusselt number (Nu) and Fanning friction factor (f), and (b) comprehensive performance evaluation index (ζ) at different channel diameter (D).

To determine the effect of the zigzag channel diameter on PCHE performance, the same mass flow rate (8.515×10^{-5} kg/s) was simulated on both sides. The channel-diameters was 2-4 mm. As shown in Figure 3.24 (a), the Nusselt number decreases, and the friction factor increases more quickly with an increasing in channel diameter. This indicates that the small-diameter channel is better in terms of overall heat-transfer characteristics. In addition, the small-diameter channel reduces the friction loss, power consumption, and heat exchanger size. Therefore, the small-diameter channel exhibited a better comprehensive performance evaluation index in Figure 3.24 (b).

3.10.6 Comparison Between Present Study and Other Research of 15° Bending Zigzag Channel

This study examines the effect of channel geometry on PCHEs performance in a laminar flow condition. Figure 3.25 showed that the comparison of the present study results and Kim's correlation results (Kim & No, 2013). Kim's model used a sharp-cornered zigzag channel with a bending angle of 15° and a channel diameter of 1.51 mm, while the present study used a round-cornered zigzag channel with a bending angle of 15° and a channel diameter of 2 mm. The round-cornered zigzag channel can provide better heat transfer. However, the present CFD study increased the Fanning friction factor. It is because the channel diameter increased by 1.32 times compared to the Kim model. This study observed a significant effects of geometrical structures and the corresponding parameters on the thermal and hydraulic performance of PCHEs. A study on the optimization of channel structure in zigzag channel PCHEs will be performed in the future.

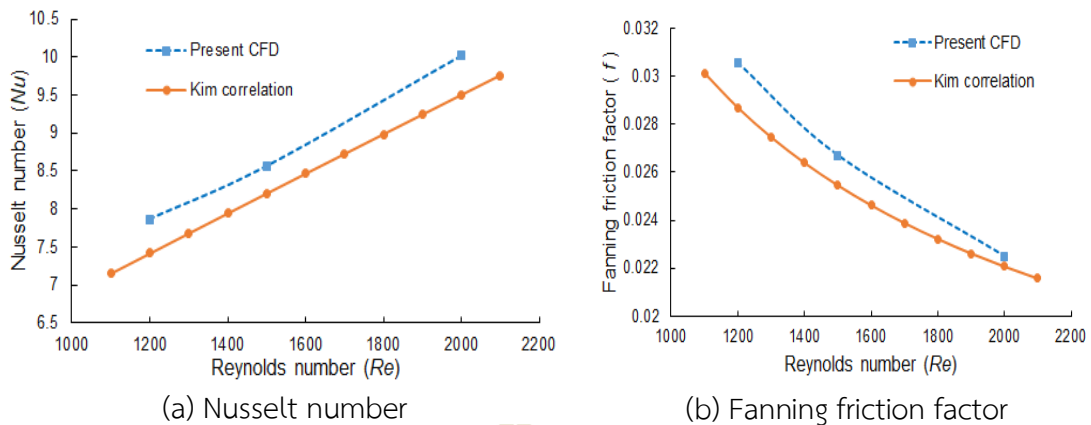


Figure 3.25 Comparison of present CFD and Kim's correlation results

3.10.7 Challenges in Geometry Optimization from Case Study of Channel Structure Analysis

Two types of microchannel, straight and zigzag were investigated in this study. The effect of the thermophysical properties along the flow direction between the straight and zigzag channel PCHE was studied at a specified mass flow rate. The channel shapes were found to significantly affect the heat-hydraulic performance. In local and global analysis, the zigzag channel PCHE offered maximum heat transfer with an extra pressure drop compared to a straight channel under the considered operating regime. In addition, the global Fanning factor decreased with increasing mass flowrate, which was related to the decrease in fluid density and viscosity. The global Nu of all channel shapes increases with increasing mass flow rate. This study shows that a zigzag channel enhances the convective heat transfer performance and reduces the flow friction. In this study, the zigzag small-channel diameter reduced the pressure drop and increased heat transfer. Therefore, a zigzag channel with a small diameter has a relatively high comprehensive performance-evaluation index. Based on a comparative analysis, channel structures and designs with various zigzag angles are recommended.

3.11 Case Study Simulation of Evaporation Effect on Heat Transfer Characteristics and Mass Transfer Multiphase Flow Channels

The primary objective of this case study was to conduct detailed simulations of evaporation effects within multiphase flow channels. By employing advanced

computational fluid dynamics (CFD) techniques, this study aims to experience phase change phenomena such as boiling or condensation, particularly at higher heat fluxes. Modeling these two-phase flow regimes requires specialized models and considerations for phase-change heat transfer.

3.11.1 Numerical Methodology and Mesh Convergence Study

The numerical simulation of phase-change mass and heat transfer in a horizontal minichannels was modelled in ANSYS Fluent with nitrogen working fluid. Figure 3.26 presents the geometric parameters and boundary condition of 3-D model for the evaporation process. the VOF method with the SST $k-\omega$ model and a user defined function (UDF) code based on Lee model was used to illustrate the behavior of the vapor distinct from the liquid. Different Grid densities were carried out for each process considering the running time and the accuracy of the results. The grid of 85499 elements in Figure 3.27 was chosen because with further refining, the liquid volume fraction stayed in the same range with maximum error of 0.7% in Figure 3.27 but the time of running the simulation increases. The water working fluid was used in mesh convergence study and model verification.

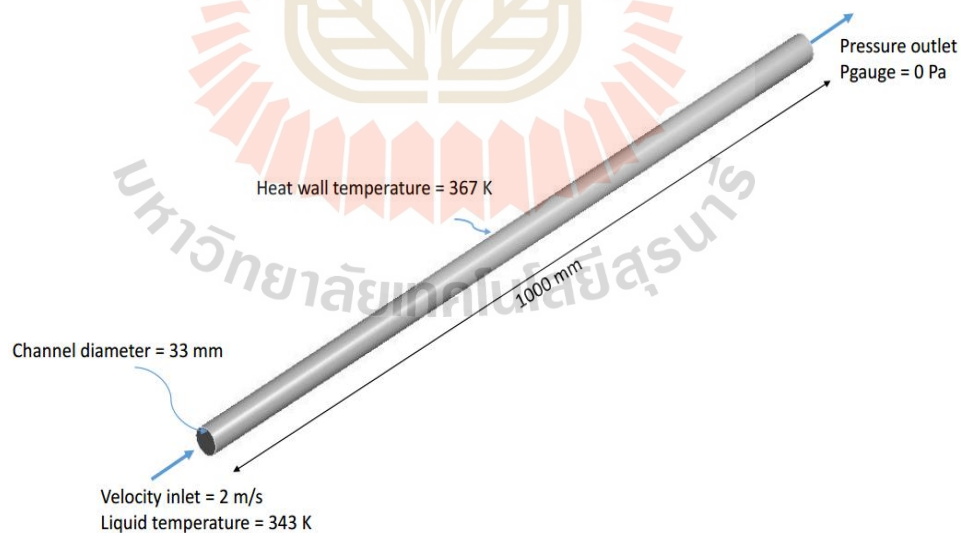


Figure 3.26 Geometry and boundary condition.

3.11.2 Model Validation

To validate the numerical work for evaporation process, two previous studies were repeated with the same geometry and the same boundary conditions. Inlet velocity were 1.0 m/s, 1.5 m/s, and 2.0 m/s, while set up the inlet liquid temperature was 343 K and the wall temperatures was 351 K. The present results show a well agreement in the relationship between the heat transfer coefficient and the velocity, maximum error 4% with H.I. Mohammed et al. (Mohammed et al., 2019), as shown in Figure 3.28.

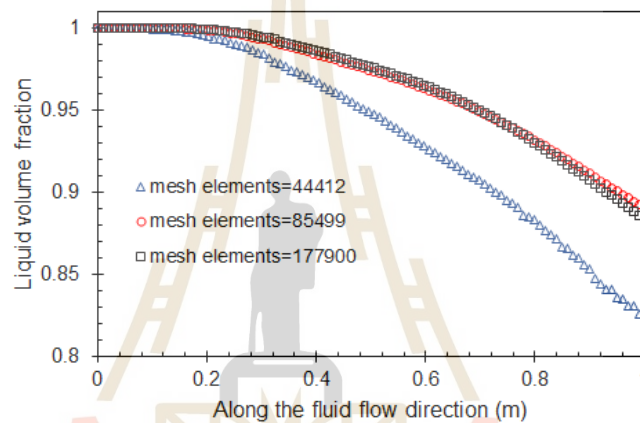


Figure 3.27 Mesh convergence study at 1sec.

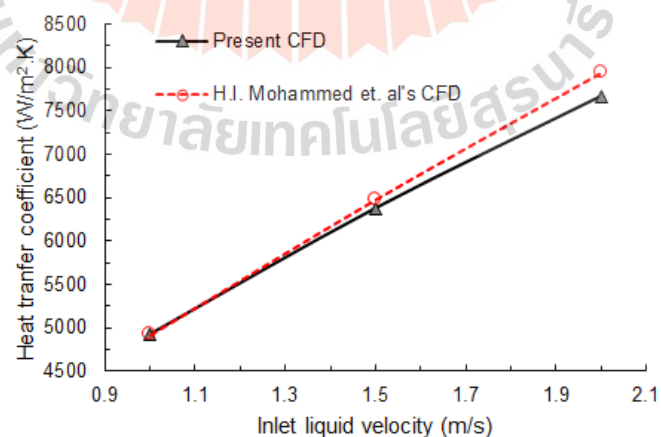


Figure 3.28 Comparing the results of the relationship between heat transfer coefficient and velocity of the present work, H.I. Mohammed et al.'s (Mohammed et al., 2019).

3.11.3 Analysis of Evaporation Process Within Multiphase Flow Channel

Nitrogen was used as a working fluid for modeling of two-phase condition. The liquid nitrogen in channel set up inlet mass flowrate 0.025 kg/s, temperature 70 K and outlet pressure 0.65 MPa. The outside heated wall temperature was 293 K. In figure 3.29, vapor velocity profile gradually changes

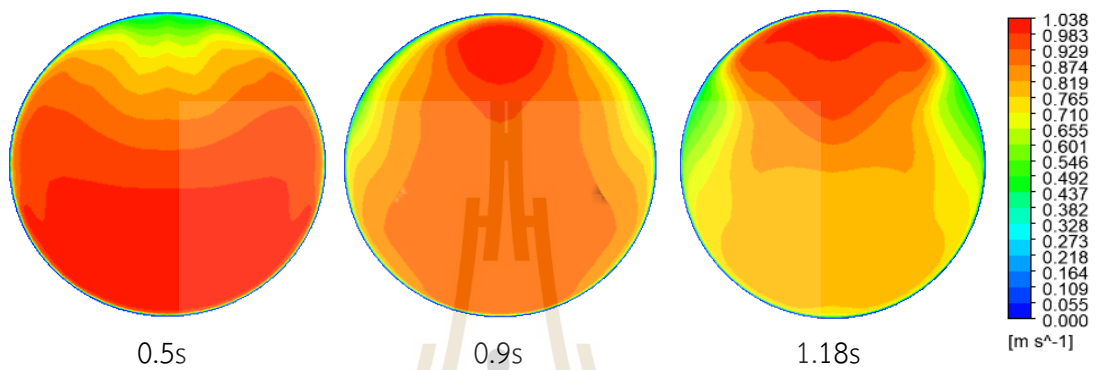


Figure 3.29 Velocity distribution of section $Z=980$ mm.

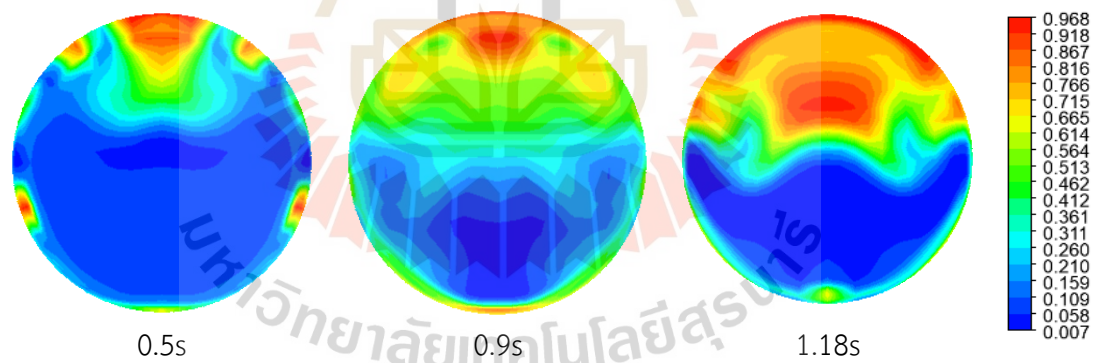


Figure 3.30 Vapor distribution of section $Z=980$ mm.

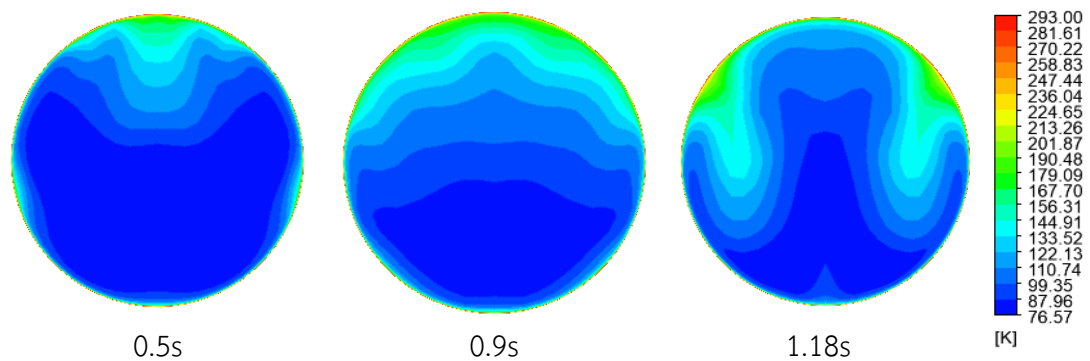


Figure 3.31 Temperature distribution of section Z=980 mm.

along the radial direction. because of drag force and float lift the velocity of upper vapor that in the area of mainstream. The vapor content increasing in figure 3.30, the velocity become higher and move the upper region of channel because the density of vapor is smaller than liquid. When the nitrogen fluid heated and evaporated, the vapor quantity increases gradually in radial direction with heating time increasing. It can be seen that the vapor is more and more in the upper of the channel and liquid nitrogen content less in the lower of the tube due to the gravity effect. In figure 3.31, temperature of wall in the upper region become high with the vapor content increases.

3.11.4 Summary of Evaporation Process Within Multiphase Flow Channel

Successfully transitioning from 30 mm evaporation simulation to mini-channel evaporation requires a thorough understanding of the unique challenges and careful consideration of modeling approaches, numerical techniques, and validation strategies. Each challenge presents an opportunity to deepen the understanding of mini-channel heat transfer and optimize the design of PCHEs for enhanced efficiency and performance. The successful simulation of evaporation in 30 mm channels has provided a solid foundation for the next minichannels evaporation study. By tackling the unique complexities of mini-channel heat transfer, the main aim was to contribute valuable insights to the optimization of PCHE designs for a wide range of cryogenic applications.

CHAPTER IV

OPTIMIZING THE ZIGZAG CHANNEL DESIGN CONFIGURATIONS WITHIN PRINTED CIRCUIT HEAT EXCHANGERS (PCHES)

The optimization of zigzag channel configurations within Printed Circuit Heat Exchangers (PCHEs) is crucial for enhancing thermal and hydraulic performance. This chapter presents simulation results for zigzag channel configurations specifically designed and optimized for use in cryogenic applications. The findings aim to improve heat transfer performance and achieve significant energy savings. All simulation results and discussions are detailed below.

4.1 Analysis of The Thermal Hydraulic Characteristics of the Different Zigzag Bending Angles

To understand the mechanisms of heat transfer augmentation, an analysis was conducted on different zigzag bending angles. This analysis was carried out under the condition of identical inlet mass flow rates, while the Reynolds numbers varied.

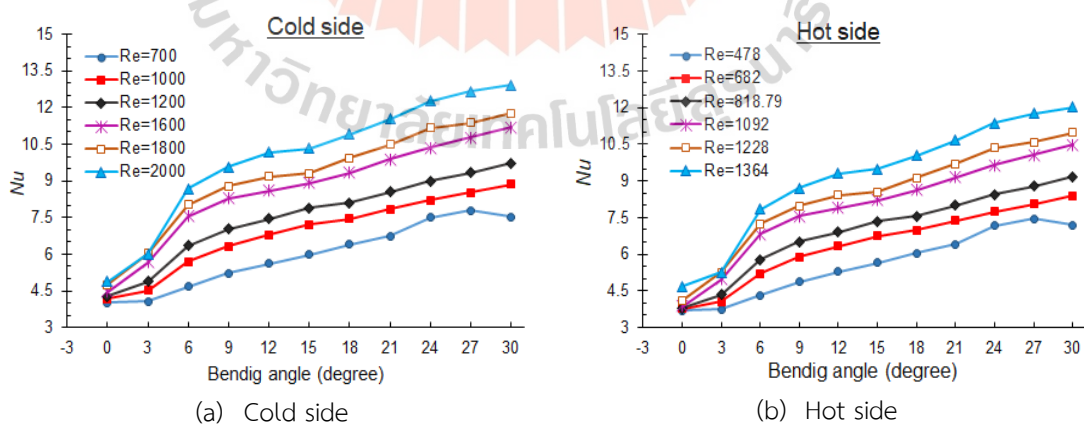


Figure 4.1 Effect of the channel zigzag angles on Nusselt number (Nu).

A comparison of the global Nusselt number for the proposed zigzag channel geometry for both cold and hot channels is shown in Figure 4.1. At each bending angle, the Nusselt number tended to increase with increasing Reynolds numbers. This suggested that higher flow velocities lead to an improved convective heat transfer. The 0° bending angle (straight channel) resulted in the lowest heat transfer augmentation.

This is expected because there is no additional mixing or disruption of the flow, resulting in a relatively lower heat transfer. At bending angles of 3° - 15° , the rate of increase in the Nusselt numbers generally became steeper with higher Reynolds numbers, indicating a stronger impact of flow velocity on heat transfer enhancement at these bending angles. At bending angles of 18° - 30° , the rate of increase becomes less pronounced compared to the previous range, suggesting a diminishing effect of channel curvature on heat transfer enhancement. However, the heat transfer augmentation mechanisms associated with a bending angle of 15° may become less effective at higher Reynolds numbers. Other factors, such as flow separation and dead zones, may impact the heat transfer capacity and reduce the effectiveness of the 15° bending angle in enhancing heat transfer. Overall, the behavior of the Nusselt number within each range of bending angles indicated the influence of the channel curvature on heat transfer augmentation.

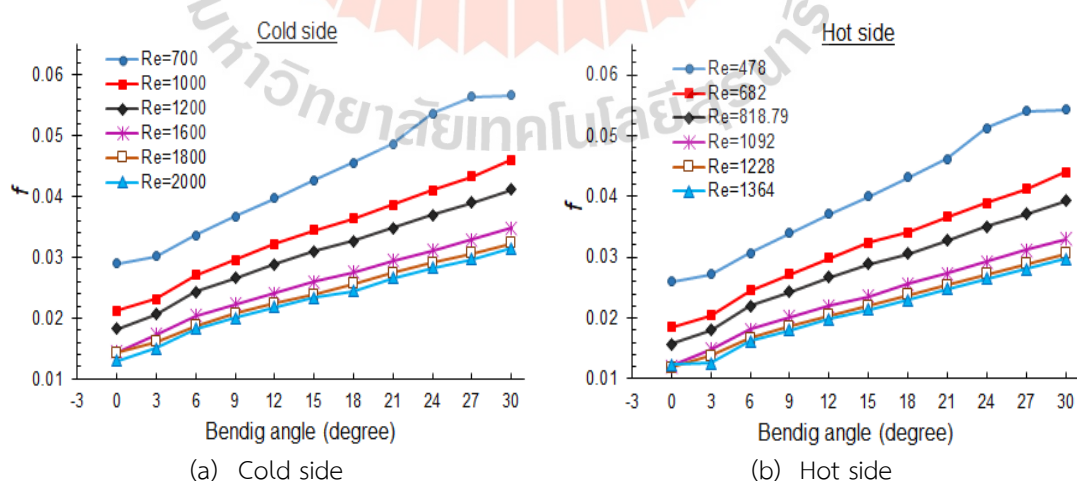


Figure 4.2 Effect of the channel zigzag angles on pressure loss factors (f).

The global friction factor comparison for the various proposed curved channels is shown in Figure 4.2. It was found that the patterns of pressure losses decreased with increasing mass flow rate. When the fluid slowly passes through a small channel, fluid viscosity is relatively higher, and frictional shear force rises. Therefore, pressure drop increasing in zigzag-channel PCHEs was directly proportional to volumetric flow rates under the laminar flow condition. Moreover, it was observed that the pressure drop on both sides increased with an increase in the zigzag angle. An increase in the actual fluid-flow length was expected to generate more friction, resulting in a higher loss in curved elbows in the bending channel owing to direction changes.

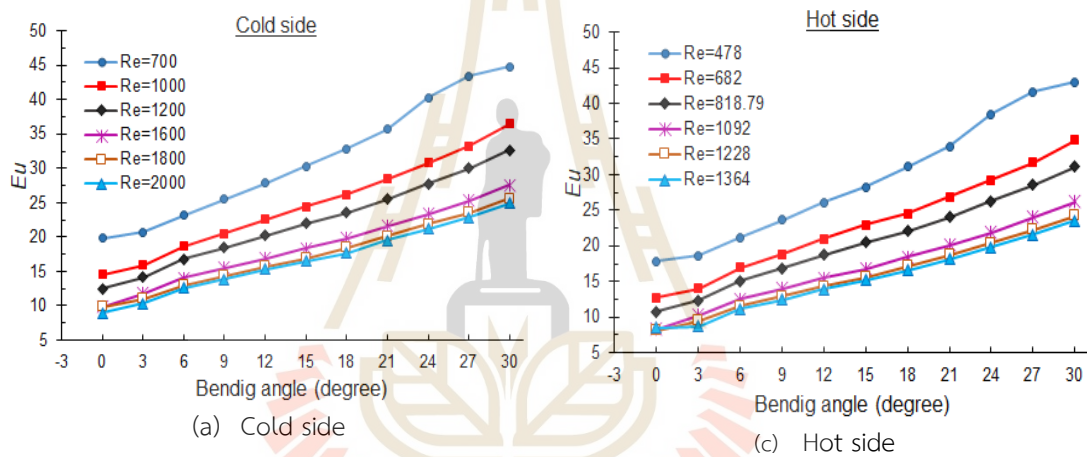


Figure 4.3 Effect of the channel zigzag angles on Euler number (Eu).

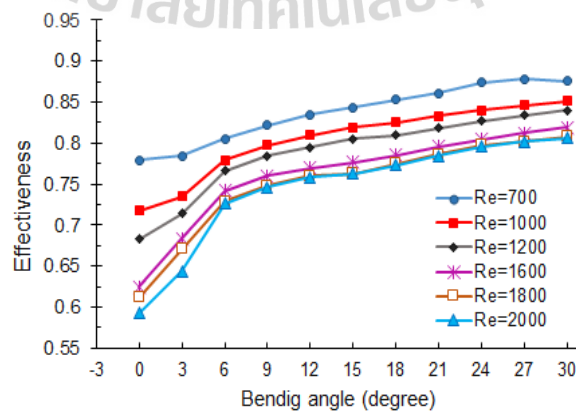


Figure 4.4 Compare the effectiveness of various zigzag angles on cold side.

Figure 4.3 shows the Euler numbers for different bending angles in the zigzag channel printed circuit heat exchanger (PCHE). The results indicated that increasing the bending angle generally leads to higher Euler numbers, suggesting greater flow resistance and pressure drop within the zigzag channels. This can be attributed to the increased flow disruption caused by curvature bends, resulting in more mixing flow and higher energy losses. Additionally, higher Reynolds numbers generally resulted in lower Euler numbers, thereby improving flow efficiency and reducing pressure drop. This can be attributed to the enhanced convective heat transfer and reduced flow resistance associated with the higher fluid velocities. The results suggested that the bending angle and Reynolds number significantly influence flow resistance and flow efficiency. Further analysis, including considerations of heat transfer performance and effectiveness was necessary for a comprehensive evaluation of the PCHE performance and to make informed design decisions.

Figure 4.4 illustrates the effectiveness comparison of the zigzag-channel PCHEs versus the angled channel curves for different Reynolds numbers. The effectiveness increased with decreasing mass flow rates, which was achieved by a lower Reynolds number leading to a higher exit temperature on the cold side and lower on the hot side. The cold fluid can take more time to absorb heat from the hot fluid, resulting in lower mass flow rates and higher cold outlet temperature. The heat transfer effectiveness tends to be relatively lower at small angles ($0^\circ - 3^\circ$). This is because the heat transfer surfaces are nearly parallel to each other, resulting in a smaller available surface area for heat transfer. Within the range of 6° to 30° , the results suggest that increasing the angle between the heat transfer surfaces generally leads to an improved heat transfer effectiveness. This indicates that increasing the angle of the heat transfer surface can enhance heat transfer efficiency. However, weighing energy on quality and quantity was not feasible for mass flow rate reduction, as it was an effective improvement. It was intended to be reasonable in operating and thermal product parameters for heat exchanger systems (Wang & Wu, 2017). It was clarified that the flow resistance and convective heat enhancement should be considered more in thermal designs.

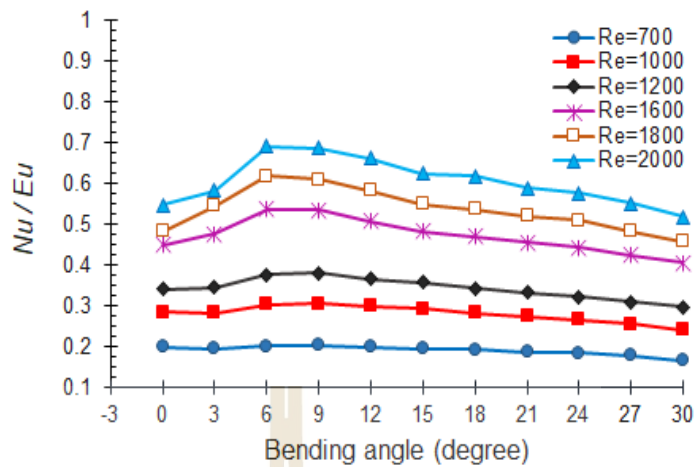


Figure 4.5 Compared the performance evaluation criteria (Nu/Eu) of various zigzag angles on cold side.

The objective of enhancing the performance of the heat exchanger involved improving heat transfer efficiency while minimizing pressure drop. To achieve this, it was crucial to consider the heat transfer and pressure loss characteristics of supercritical helium in Printed Circuit Heat Exchangers (PCHE). In this study, the ratio of Nusselt number to Euler number (Nu/Eu) was introduced as a measure of the supercritical helium performance in the channel. A higher Nu/Eu ratio indicated better heat transfer performance. The ratio of the Nusselts number and Euler number (Nu/Eu) analyses for the thermal-hydraulic performance of the PCHEs are in Figure 4.5. The Nu/Eu increased as the mass flow rate increased, which developed the fluid volume unit's heat-absorbed capacity. The 6° and 9° bending channel PCHE was at the highest performance evaluation criteria compared to other bending channel angles of PCHEs. The performance evaluation criteria significantly reduced when the bending channel angle exceeded 9°, whereas the pressure losses were much larger than the heat transfer, as discussed earlier. Consequently, the PCHE performance evaluation criteria are not good at exceeding the 9° bending channel angle. The pressure loss results mainly show the drastic changes along the flow direction in this region, which led to an extreme disturbance in the flow. The penalty of pumping power increased with the larger size. In the bending channel angle before 9°, its performance evaluation criteria

were developed with the increased channel bending angle and mass flow rates with better heat transfer and low-pressure losses. Therefore, selecting the bending channel angle is a qualified process between the pressure drop and heat-transfer performance under the same operating conditions. These results indicate that it is more effective to use the 6°- 9° bending channel at low Re in PCHes. Conversely, at higher Reynolds numbers, a channel bending angle of 9° slightly dropped the performance. Therefore, a channel bending angle of 6° showed a greater tendency for enhanced heat transfer in high-flow regimes.

4.2 Correlation Analysis for Friction Factor and Nusselt Number in Optimal Angle Zigzag Channel PCHes

The effect of Reynolds number was investigated for various channel angles in PCHes. The bending channel angles of 6° and 9° demonstrated improved performance in PCHes. Therefore, the correlation took into consideration the specific channel angles of 6° and 9° bending angles. The development of 6° and 9° bending angle correlations for friction factor (f) and Nusselt number (Nu) with constant boundary conditions and various zigzag angles (α) was presented through computational simulations. The fitted f and Nu correlations were considered the curved and the straight associated with Re and the Prandtl number (Pr) (Kim & No, 2013).

$$f.Re = 15.78 + C_1 Re^a \quad (4.1)$$

$$Nu = 4.089 + C_2 Re^{b1} Pr^{b2} \quad (4.2)$$

However, the present simulation was analyzed with constant Prandtl number ($Pr = 0.66$) and various zigzag angles on a range of Re . Therefore, the correct forms of f and Nu are functionally correlated to α and Re can be represented as:

$$f.Re = 15.78 + C_1 Re^{a1} \alpha^{a2} \quad (4.3)$$

$$Nu = 4.089 + C_2 Re^{b1} \alpha^{b2} \quad (4.4)$$

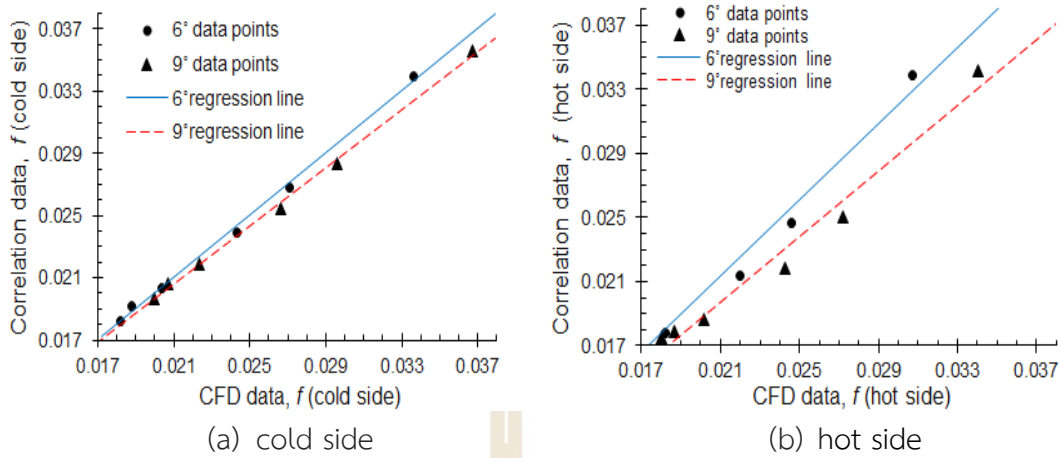


Figure 4.6 f correlation comparison for CFD cases.

The multiple nonlinear regressions method with MATLAB programming was applied to find the unknown correlations' coefficients. The proposed f correlation for the hot and cold side are:

$$f_h \cdot Re = 15.78 + 1.35 \times 10^{-7} Re^{2.6162} \alpha^{0.52221} \quad (4.5)$$

$$f_c \cdot Re = 15.78 + 4.52 \times 10^{-2} Re^{0.90287} \alpha^{0.32941} \quad (4.6)$$

where the friction factor correlations for the hot side (f_h) and cold side (f_c) have different applicable ranges based on the Reynolds number (Re). f_h is valid when the Reynolds number is in the range of 478 to 1364 and f_c is valid when the Reynolds number is in the range of 700 to 2000. The f characteristic between correlations and CFD data are shown in Figure 4.6. Based on the comparison results, it can be observed that the relative errors of the friction factor (f) correlations for the cold side channel and hot side channel fall within a range of $\pm 4.25\%$ and $\pm 10\%$ respectively.

The proposed Nu correlations for the hot and cold sides can be represented as follow:

$$Nu_h = 4.089 + 1.83 \times 10^{-5} Re^{1.8108} \alpha^{0.35952} \quad (4.7)$$

$$Nu_c = 4.089 + 8.5 \times 10^{-5} Re^{1.5732} \alpha^{0.47157} \quad (4.8)$$

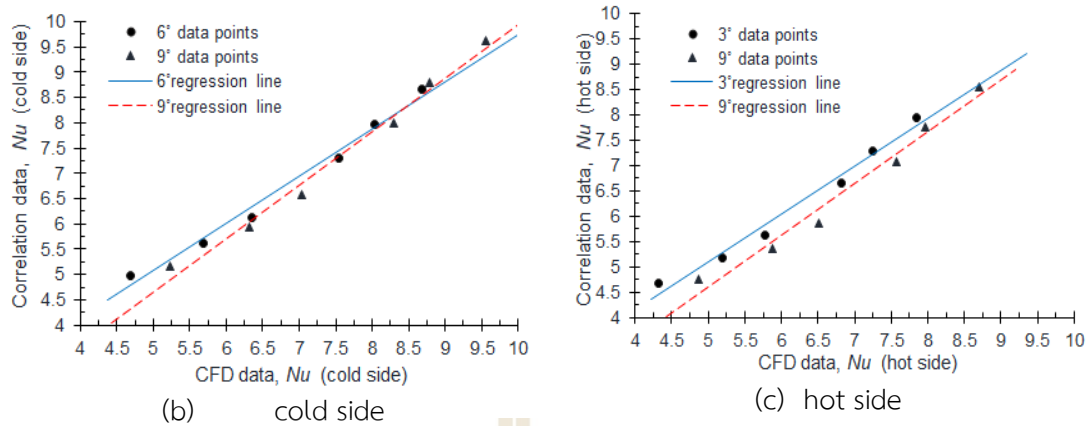


Figure 4.7 Nu correlation comparison for CFD cases.

where the Nusselt numbers (Nu) represents for the hot side (Nu_h) and cold side (Nu_c). The valid Reynolds number range was $478 \leq Re \leq 1364$ for Nu_h and $700 \leq Re \leq 2000$ for Nu_c . The Nu characteristic between correlations and CFD data are shown in Figure 4.7. Based on the comparison results, it can be observed that the relative errors of the Nu correlations for the cold side channel and hot side channel fall within a range of $\pm 6.7\%$ and $\pm 9.9\%$ respectively.

4.3 Effect of Channel Bending Angles on Local Internal Flow and Heat Transfer Characteristics

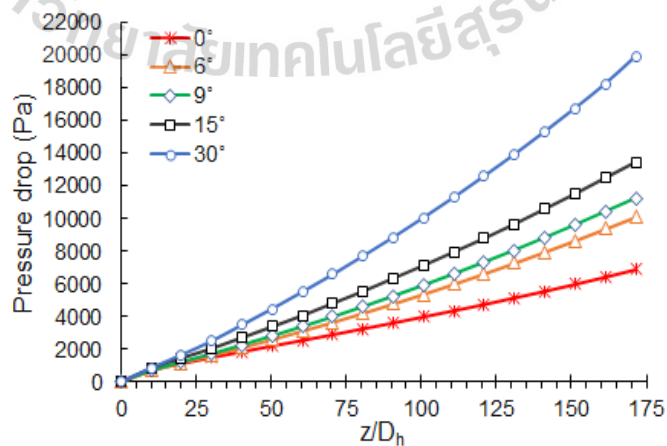


Figure 4.8 Local pressure drop in different bending channels.

According to the above analysis, there were three bending angle regions of heat transfer rate: a significant developing region ($6^\circ - 9^\circ$) and a slight developing region ($12^\circ - 30^\circ$), and a distinct improvement region ($0^\circ - 3^\circ$). Therefore, the effects of the bending angle on the internal flow and heat transfer characteristics were analyzed. This case was investigated on the cold side. The best performance angle of 6° and 9° , the performance reference angle of 0° , the original angle of 15° , and the highest angle of 30° were selected and compared.

Figure 4.8 shows the pressure drop of helium in different bending channels. The helium pressure drop, and the flow distance increased for all channels due to friction losses between the wall and the flow. According to Eq (3.6), higher pressure losses occurred when the actual flow length was increased. These results explain why the bending-angled channels increase with increasing pressure drop. For bending angle cases, the flow direction of the fluid changed rapidly around the bending point as well as the local separation flow and backflow of the fluid in Figure 4.9. In bending-angle channels, the fluid velocity near the wall was extremely low owing to the viscosity of the fluid. The fluid then initiated backflows, and the fluid boundary layer was separated from the wall. A lower fluid velocity was not sufficient to overcome this adverse pressure difference. Therefore, a separation flow zone is generated, and the fluid around the corner wall flows in the reverse direction. These separation flows blocked the flow in the channels, and the heat transfer was enhanced because of the low fluid velocity. In compared of bending angles, 6° and 9° can be smoothly passing through the channel. However, the 15° and 30° bending angles caused more separation flow, resulting in greater disturbances and pressure loss in the channel. The more bending angle caused more separation flow, resulting in greater disturbances and pressure loss in the channel. This may be caused by a reduction in effective heat transfer area due to the flow separation and dead zone, resulting in low heat transfer capacity. The pressure loss in the straight channel (0°) was reduced, driven only by friction without the separation flows.

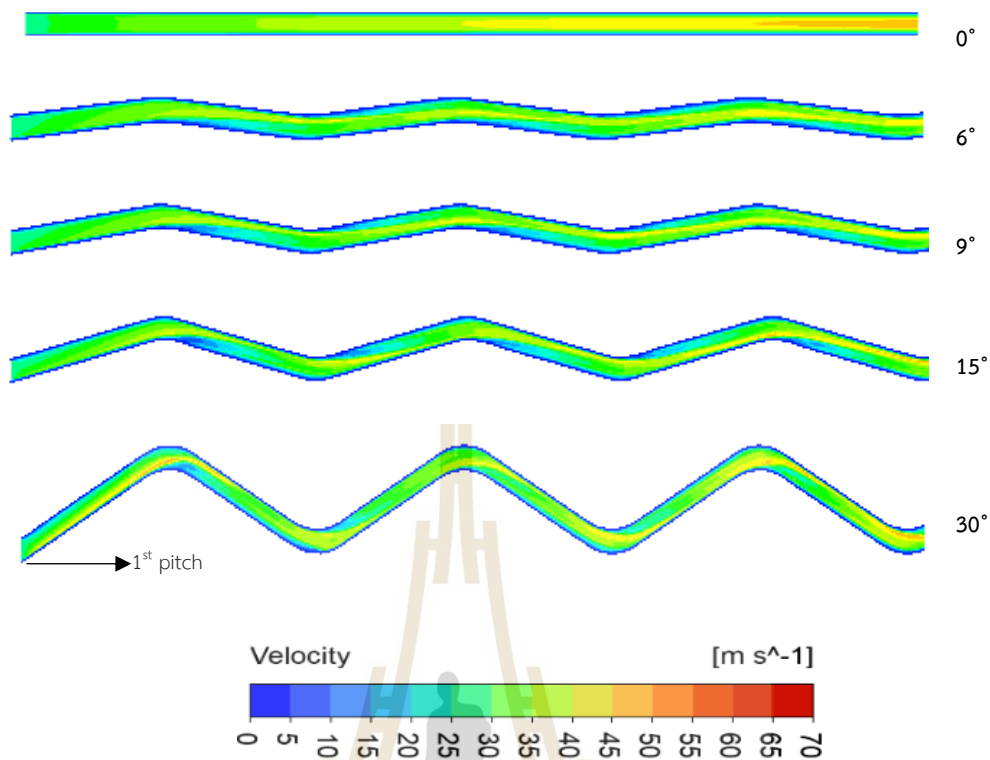


Figure 4.9 Velocity distribution in different bending channels.

Figure 4.10 shows the velocity magnitude on the cold side. A 3rd bending corner were selected to examine the effect of the channel bending angle on the local flow. In the central region of an internal flow, the fluid accelerates for the compensation in the axial velocity decreasing due to the boundary layer growth near the wall, which is well known as an accelerating core (Pan et al., 2020). It can be seen that the accelerating core was located in the central area of the straight channel. This characteristic is a laminar Poiseuille flow (pressure-induced flow), which occurs when successive concentric flow layers are heated by thermal diffusion. However, the accelerating core in bending zigzag channels, the accelerating core moves to the very exterior or region of the bending section. This is because the fluid changed direction with the periodic forcing resulting from the centrifugal force (Li et al., 2020). Then. The accelerating core thinned by shifting or even breaking the bound layer, resulting from conduction to convective heat transfer, was enhanced in the channels.

In Figure 4.11, it can be observed that the temperature gradient in the near-wall zone was much higher than that in the core region. Therefore, it had a positive effect on heat transfer performance. Furthermore, it was observed that the bending angle channel increased the small temperature gradient. The high-temperature fields were influenced near the wall at 6° and 9° , which improved the heat transfer compared with the 15° and 30° bending channel angle. This indicates that the movement of the centrifugal force and thermal-physical properties of the fluid change with the inclination angle of the channels (H. Liu et al., 2022), affecting the flow and heat transfer.

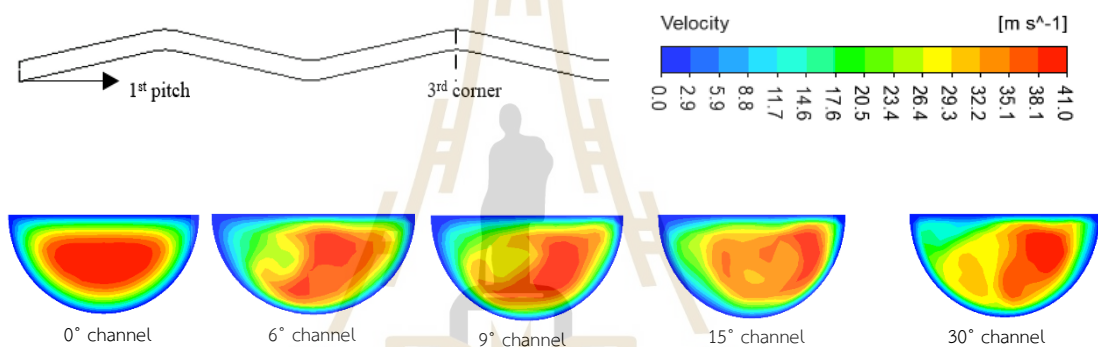


Figure 4.10 Distribution of streamwise velocity magnitudes at 3rd corner cross sections.

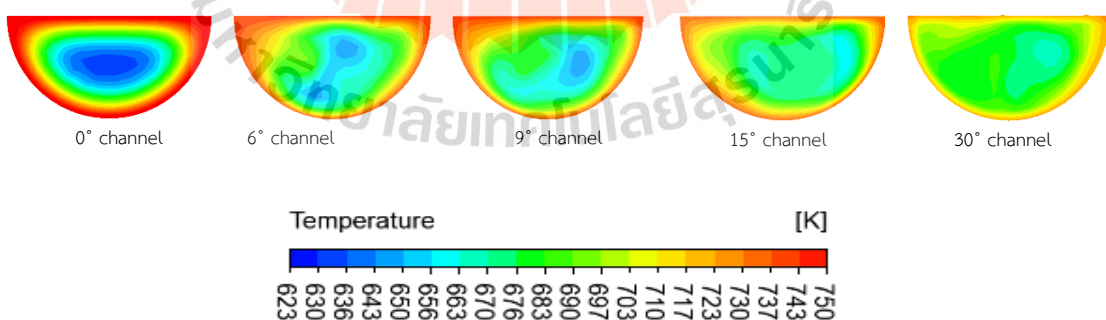


Figure 4.11 Temperature distribution at 3rd corner cross sections.

From Figure 4.12, it can be observed that the secondary flow distribution had a variety of velocity vector magnitudes. The secondary flow has important consequences for

convecting the high-momentum fluid to bend, skew the streamwise velocity, and dominating the heat transfer characteristics, called vortex flow. By the comparison, the secondary flow was more obvious at bending angle channels, while there was no secondary flow at the straight channel ($\alpha=0^\circ$). The two points showed that the collision effects were more potent at the bending angle structure, which created the radial mixing and vortex flow, and enhanced the convection heat transfer. The 6° and 9° bending angle channel had a great vortex flow than the 15° bending angle channel. Therefore, the 6° and 9° bending angle channel can enhance at a high heat transfer rate. However, the 30° bending channel angle generated the stronger two secondary vortices due to the imbalance between centrifugal force and main stream. The strength of secondary vortex flow is significantly affected heat transfer enchantment on the wall. In addition, the secondary flow induces an unstable flow field and increases pressure losses (Tang et al., 2017). Thus, zigzag-type bending channels should be carefully analyzed to reduce pressure losses and enhance heat transfer for a suitable PCHE design.

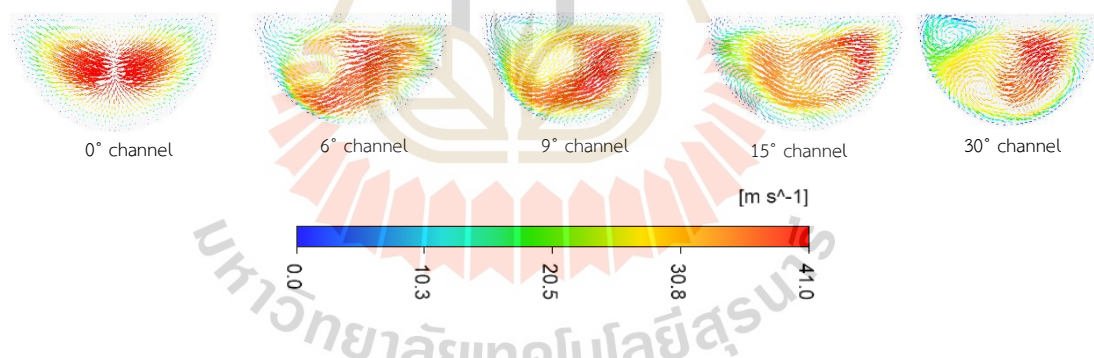


Figure 4.12 The velocity vectors at 3rd corner cross sections.

4.4 Analysis The Effect of Geometric Parameters and Compare with Other Correlation Results

The previous study analyzed the influenced of bending zigzag channel angles on heat transfer and friction factor. It was observed that the results of some channel angles varied in heat transfer and friction factor behavior. Notably, some research studies indicated an increase in both heat transfer and friction factor with an increase in the channel angle (Yoon et al., 2017). Therefore, this study analyzed a significant

effects of geometrical structures and the corresponding parameters on the thermal and hydraulic performance of PCHEs. This study focused on analyzing the significant effects of geometrical structures and their corresponding parameters on the thermal and hydraulic performance of Printed Circuit Heat Exchangers (PCHEs).



Figure 4.13 Analysis the general geometric parameters of a zigzag channel.

The zigzag channel structural parameters of PCHEs have a strong effect on thermal-hydraulic performance. Suitable structural parameters of the zigzag channel can enhance the heat transfer process and reduce the pressure drop. As shown in Figure 4.13, the general structural parameters of zigzag channels include channel diameter (D), bending angle (α), sub-channel length (L_R) and half of a pitch length (L_z). Fig.22 and 23 show the characteristics of fluid flow conditions in channels with different bending angles at a constant $L_z = 12.3$ mm and $D = 2$ mm for the previous CFD models (model A). The new CFD geometry (model B) was considered similar to Yoon's model [14]. The parameters were a zigzag angle of 9° - 21° and non-uniform half of a pitch length (L_z) for a constant diameter of 2 mm and a constant $L_R = 7.5$ mm.

The effect of channel geometric parameters considered a model A, model B and compared with published correlations. In comparison Figure 4.14 (a) and (b), the Racieli correlations (Torre et al., 2021) and the simulation results of a model A were good prediction. Racieli correlations were modified by L_R and α , a fixed diameter according to the bending angle. However, Yoon correlation was investigated at all angles for the L_R constant. Therefore, the present CFD results of a model B at all angles presented similar performance with Yoon correlation (Yoon et al., 2017). From this study, the difference geometric designs have a quite higher difference in Nu and f although the bending angles are same. The correlations showed a differences values with simulation results of this work because of the differences in the computational

models. Therefore, there are future plans to conduct a study that will specifically focus on optimizing the channel structure in zigzag channel Printed Circuit Heat Exchangers (PCHEs).

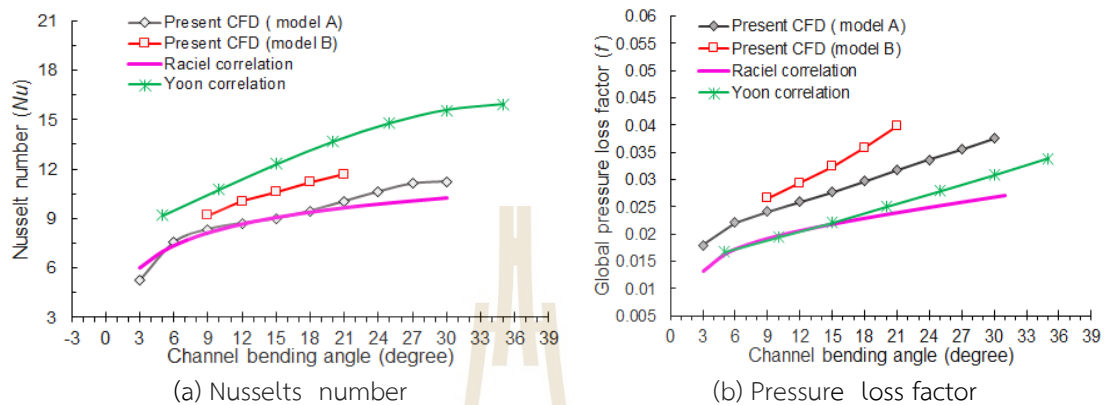


Figure 4.14 Results based on channel curvature length (L_R) at $Re=1500$.

4.5 Overview of The Bending Number Effect On PCHE in Zigzag Channels

Previous studies have analyzed the impact of bending angles on internal flow and heat transfer characteristics. The expectation was for a significant increase in heat transfer rates along the zigzag channel. However, the observed greater separation flow resulting from increased bending angles led to heightened disturbances and pressure loss within the channel. This phenomenon can be attributed to a decrease in the heat transfer rate due to flow separation and dead zones, consequently reducing the effective heat transfer area (Aye et al., 2023). Hence, the structural parameters of zigzag channels in PCHEs play a crucial role in determining thermal-hydraulic performance. Optimal structural parameters of the zigzag channel are crucial for enhancing the heat transfer process and minimizing pressure drop. Dimensionless numbers, which incorporate the primary geometric features of zigzag channels and represent their bending level, overcome the aforementioned problems.

Common structural parameters of zigzag channels encompass channel diameter (D), bending angle (α), wavy amplitude (x), and pitch length (P_l). As shown in

Figure, the bending number is defined as the ratio of the wave length to the width of the zigzag channel at the corner y , expressed as (S. Liu et al., 2022):

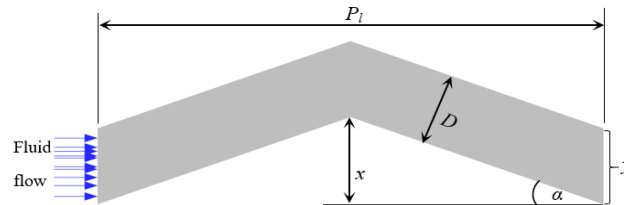


Figure 4.15 Common structural parameters of a zigzag channel.

$$\beta = \frac{x}{y} \quad (4.9)$$

Here,

$$x = \frac{P_l}{2} \times \tan(\alpha), \quad y = \frac{D}{\cos(\alpha)} \quad (4.10)$$

$$\beta = \frac{P_l \sin(\alpha)}{2D} \quad (4.11)$$

The bending number serves as a measure of the channel's bending effect on flow conditions, with a critical value set at 1. This study specifically investigates the impact of varying channel diameter on PCHE performance within a defined bending angle range. The established relationships highlight that when the amplitude (x) exceeds the diameter (D) and β is greater than 1, some fluid diverges around the corner. Conversely, when x is less than D and β is less than 1, some fluid passes through the channel. The current research was analyzed using the newly generated Bending number. A compilation of β values from various investigations was presented in Table 4.1. Interestingly, it demonstrated that some showed better results with β_{best} values above 1, whereas others showed higher performance when β_{best} is below 1. The observed variety highlights the intricate nature of the correlation between zigzag channel performance and bending number. Further investigation is necessary to achieve a thorough comprehension and resolution of these disparate results. The

reference geometry for this study was based on the zigzag Printed Circuit Heat Exchanger (PCHE) channel, as utilized in previous research (Aye et al., 2023). Table 4.2 and Figure 4.16 give the study range for the dimensions of the PCHE geometry.

Table 4.1 Different bending number studies for zigzag channel PCHEs.

Ref	D , mm	P_t , mm	α	β	β_{best}
(Saeed & Kim, 2017)	1.8	7.24 -13.028	50°-65°	1.54 - 3.28	1.97
	(cold side) 1.9 (hot side)	9 -16.19	57.75° -70.51°	1.99 - 4.02	2.51
(Pan et al., 2016; Pan et al., 2020)	1.8	26	15° - 45°	1.87 - 5.11	1.87
	(cold side) 1.8 (hot side)	26	15° - 45°	1.87 - 5.11	1.87
(Zhao, Zhou, et al., 2019b)	1.5	20	5° - 45°	0.58 - 4.71	0.58-1.16
(Jin et al., 2022a)	2	20	45°-82.5°	3.54 - 4.96	3.54
	2	10-25	45°	1.77 - 4.42	1.77
	2	10-25	52.5°	1.98 - 4.96	1.98
	2	10-25	60°	2.17 - 5.41	2.17
	2	10-25	67.5°	2.31 - 24.52	2.31
	2	10-25	75°	2.41 - 24.79	2.41
	2	10-25	82.5°	2.48 - 6.2	2.48
	(H. Liu et al., 2022)	1.51	24.6	15° - 45°	2.11 - 5.76
(cold side) 1.8 (hot side)	24.6	15° - 45°	1.77 - 4.83	1.77	
(Lin Yuan-Sheng, 2019)	2.4	16	10° - 30°	0.58 - 1.67	1.14
(Zhang et al., 2019)	1.8	6.12-10.67	35° - 90°	0.98-2.96	2.43 2.1

Table 4.2 The PCHE geometry dimension on both sides.

Parameter	Value
Channel angle, α	$3^\circ, 6^\circ, 9^\circ, 12^\circ, 15^\circ, 18^\circ, 21^\circ, 24^\circ, 27^\circ, 30^\circ$
The width between channel and side wall, w	0.25 mm
Thickness between two channel, t	0.6 mm
Channel pitch length, P_c	24.6 mm
Number of curved corners	16
Bend curvature radius, r_b	4 mm
Channel diameter, D	2-5 mm

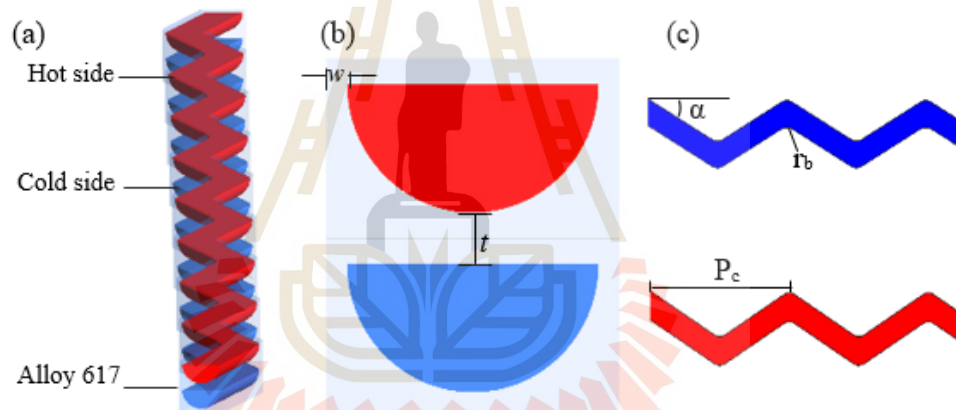


Figure 4.16 Schematic of PCHE geometry, (a) the zigzag channel unit, (b) the cross-section unit, and (c) the pitch of the zigzag channel with the inserted curvature at the corners.

Figure 4.17 illustrates the parameters used for analyzing the bending level of zigzag channel PCHE. The study focused on the use of supercritical helium as the working fluid, with Reynolds numbers based on the flow conditions ranging from 1000 to 2000.

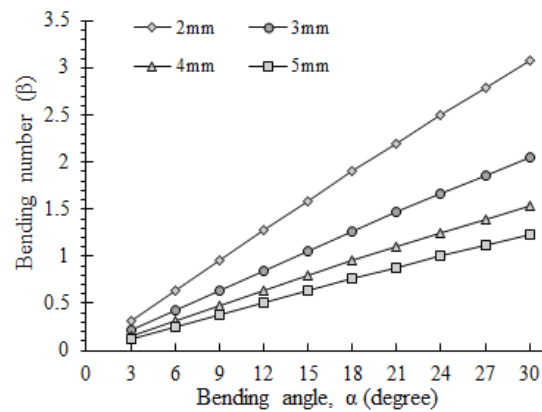


Figure 4.17 Bending number at various bending angles and channel sizes.

4.6 Impact of Bending Number Variations on Zigzag Channel Flow and Heat Transfer Distribution

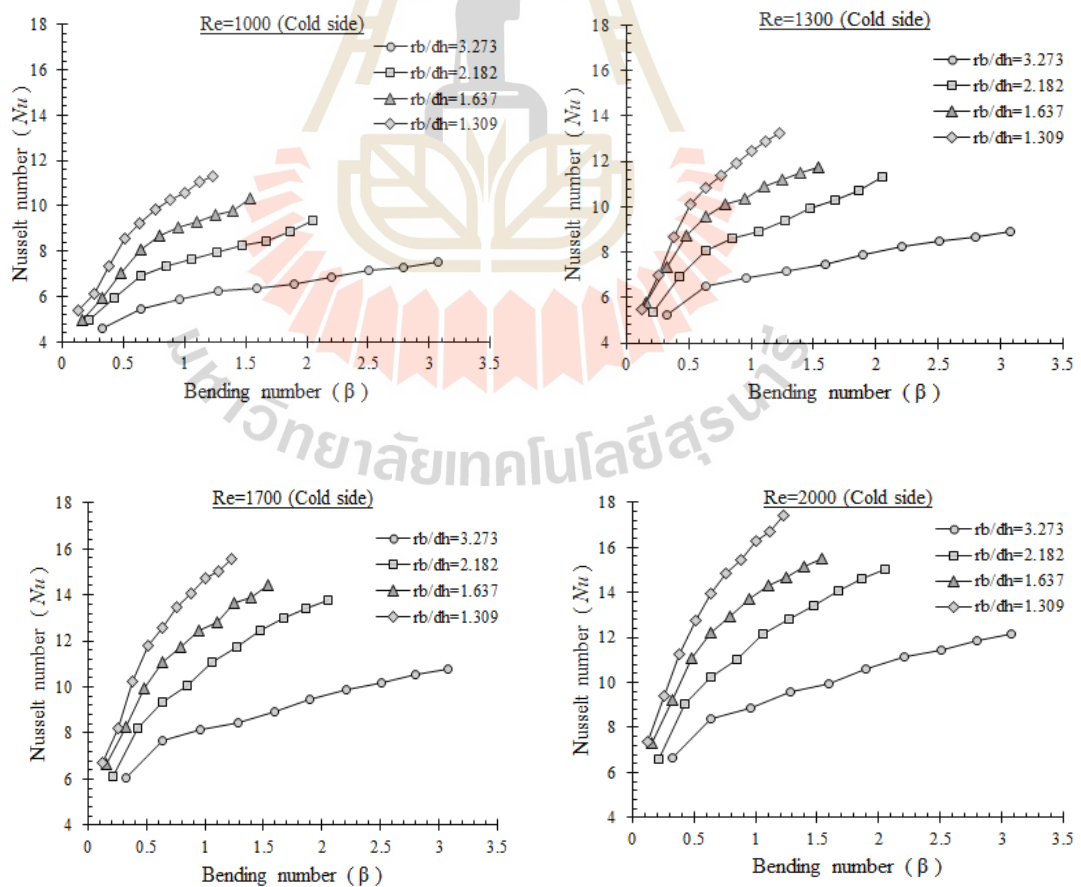


Figure 4.18 Nusselt number at various bending number (cold side).

The Nusselt number is a key parameter in heat transfer analysis, providing insights into the convective heat transfer characteristics of channelized systems. Figure 4.18 and 4.19 represents the Nusselt numbers on both cold and hot side for different zigzag channel configurations under the inlet same Reynolds number. The trend shows that the Nusselt number increases with decreasing the ratio bend radius to hydraulic diameter (r_b/d_h), indicating enhanced convective heat transfer as the channel size expands. This aligns with expectations, as larger channels typically facilitate greater fluid mixing and heat exchange. In addition, the channel bending number influences

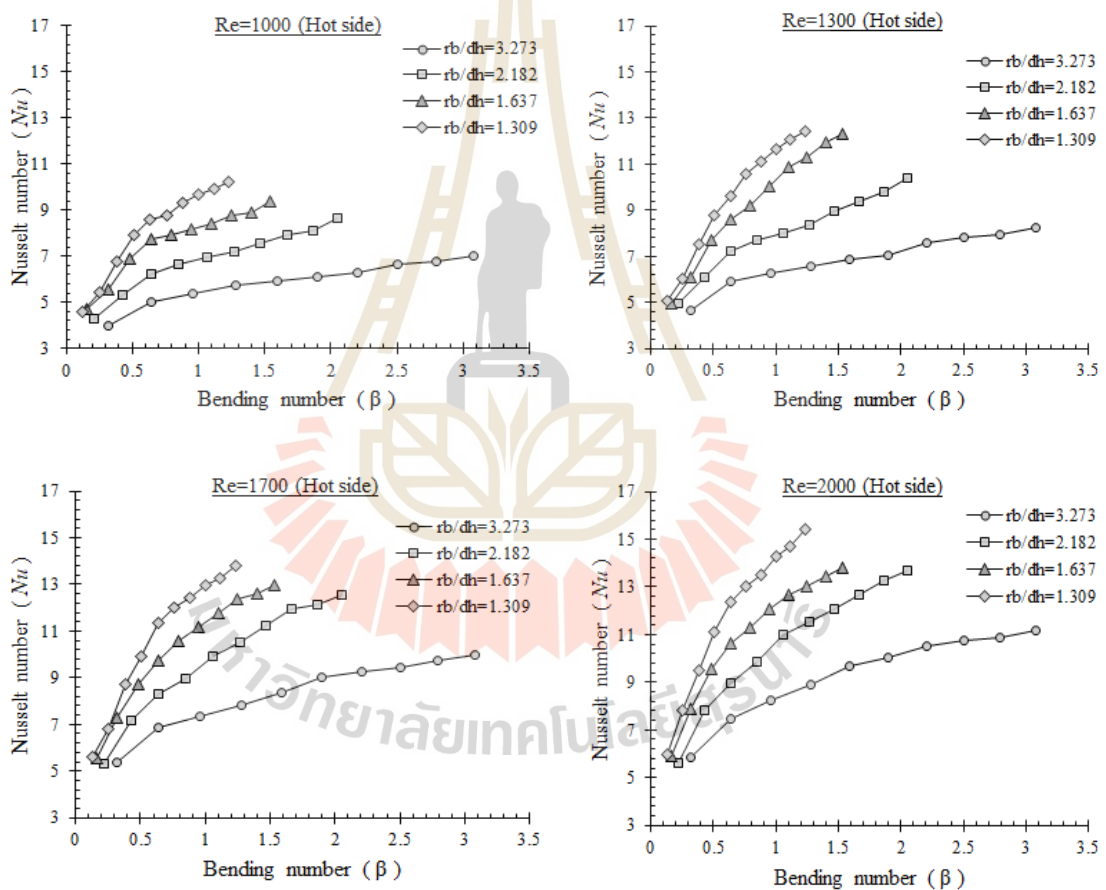


Figure 4.19 Nusselt number at various bending number (hot side).

the Nusselt number. The Nusselt numbers significantly rise below $\beta = 1$ and increase steadily after $\beta = 1$. The curvature effects are minimal at low β , leading to a more streamlined flow without significant secondary flows or disturbances. This condition

allows for a more uniform and efficient convective heat transfer process, resulting in a steep rise in heat transfer efficiency. In contrast, at higher bending numbers (above 1), the increased curvature effects lead to more pronounced secondary flows, causing disturbances in the primary flow. These disturbances can create regions of recirculation and flow separation, which can reduce the overall heat transfer efficiency due to inconsistent temperature gradients and disrupted flow paths. Moreover, it is observed that higher Reynolds numbers enhance fluid mixing and promote convective heat transfer, leading to increased Nusselt numbers and improved heat transfer efficiency.

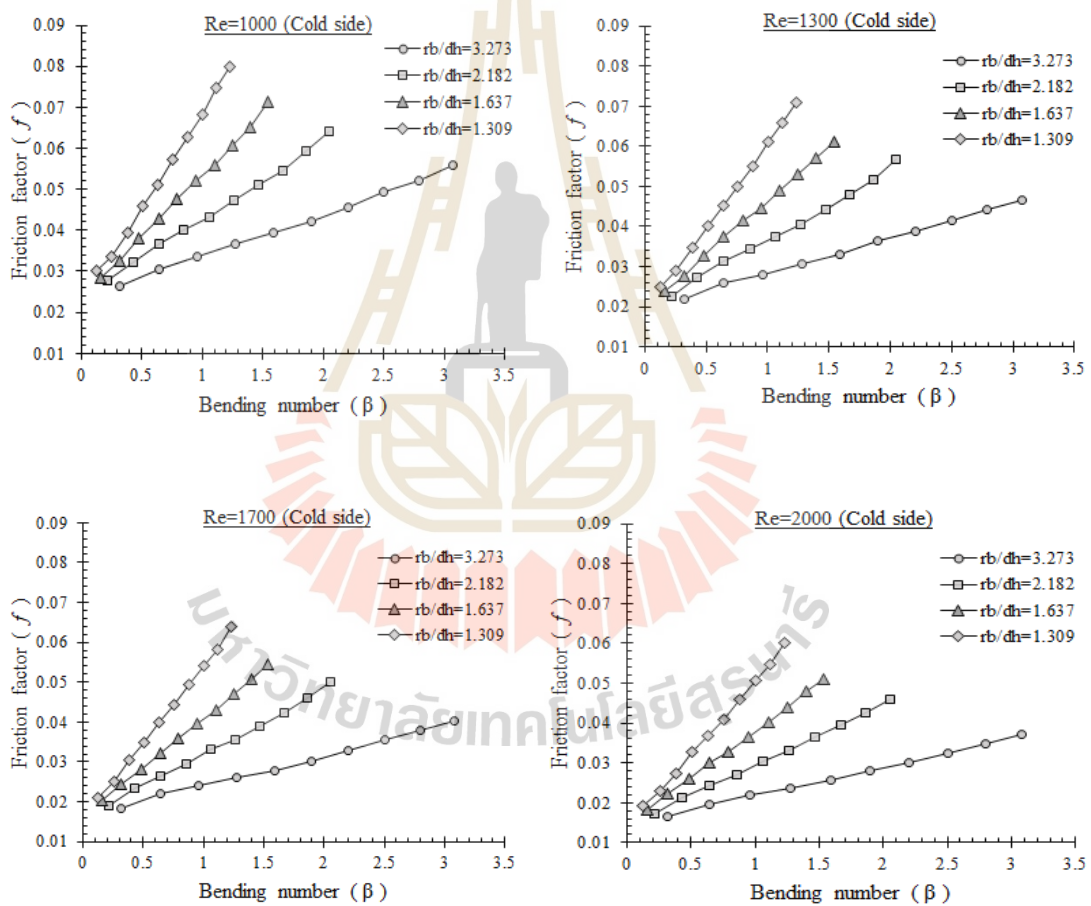


Figure 4.20 Friction factor at various bending number (cold side).

The friction factor is a crucial parameter in PCHE performance analysis, influencing pressure drop, flow resistance, and energy consumption in channelized systems. Figure 4.20 and 4.21 show the friction factor of various zigzag channel configurations. It is found that low r_b/d_h increase friction factors. At low r_b/d_h ratios where the flow tends to be more laminar and orderly, adhering closely to the channel walls. This adherence increases the shear forces between the fluid layers and the channel walls, leading to a higher friction factor. In contrast, low bending numbers (low β) decrease friction factors primarily by minimizing curvature effects, reducing secondary flow development, maintaining thinner boundary layers, and lowering pressure drops across the bends. These factors collectively contribute to smoother, more efficient fluid flow with reduced frictional losses in the channel.

The Fanning friction coefficient is observed as the Reynolds number increases. This coefficient demonstrates an inverse relationship with the Reynolds number, indicating that as flow velocity increases, friction decreases. In addition, a larger Fanning friction coefficient was found on the cold side than on the hot side, owing to the distinct physical properties of the supercritical fluids. Cold flow has a much higher density and viscosity than hot flow, resulting in increased frictional resistance.

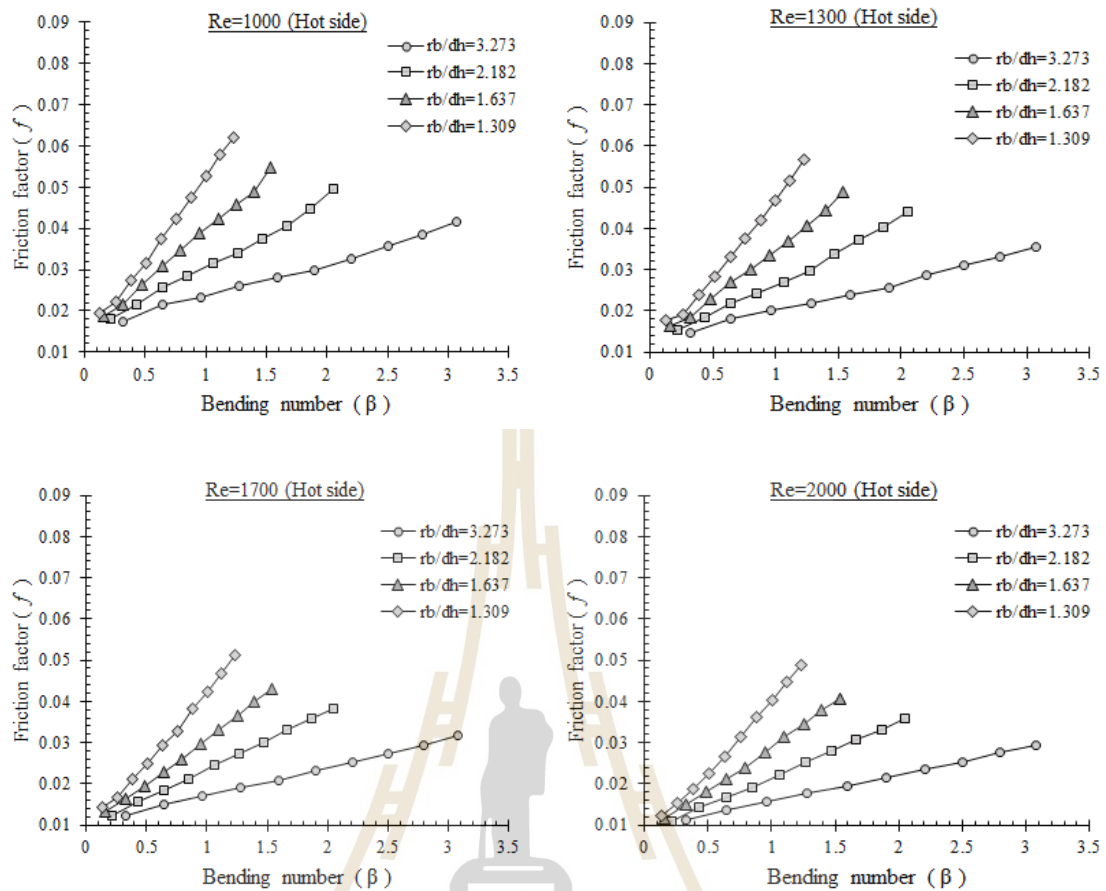


Figure 4.21 Friction factor at various bending number (hot side).

It is important to consider the appropriate criterion when evaluating heat transfer performance in different scenarios. The commonly used criterion, Nu/f , allows for a direct comparison of heat transfer coefficient (Nu) and friction factor (f) between different flow lengths and heat transfer area. It is suitable for comparing heat transfer enhancement relative to the pressure drop in systems with varying lengths (Pan et al., 2020; Wang et al., 2021). On the other hand, the criterion $Nu/f^{1/3}$ is more appropriate when comparing heat transfer performance for systems with the same length and heat transfer area (Zhao, Zhou, et al., 2019a). In this study, zigzag channels with various bending angle parameters. It can achieve a greater heat transfer rate. Increasing the bending angle enhances overall heat transfer, primarily due to the increased flow length and heat transfer area. To fully understand the enhanced heat transfer, it is

essential to consider the effects of the increment in heat transfer area. Therefore, thermal hydraulic performance is evaluated by the ratio Nu/f .

Figure 4.22 reveals notable differences in heat transfer efficiency across various zigzag channel configurations. Generally, higher Reynolds numbers correspond to higher Nu/f ratios, indicating improved heat transfer performance per unit of pressure drop. The impact of bending number on Nu/f ratios may vary with Reynolds number, reflecting changes in flow behavior and heat transfer mechanisms.

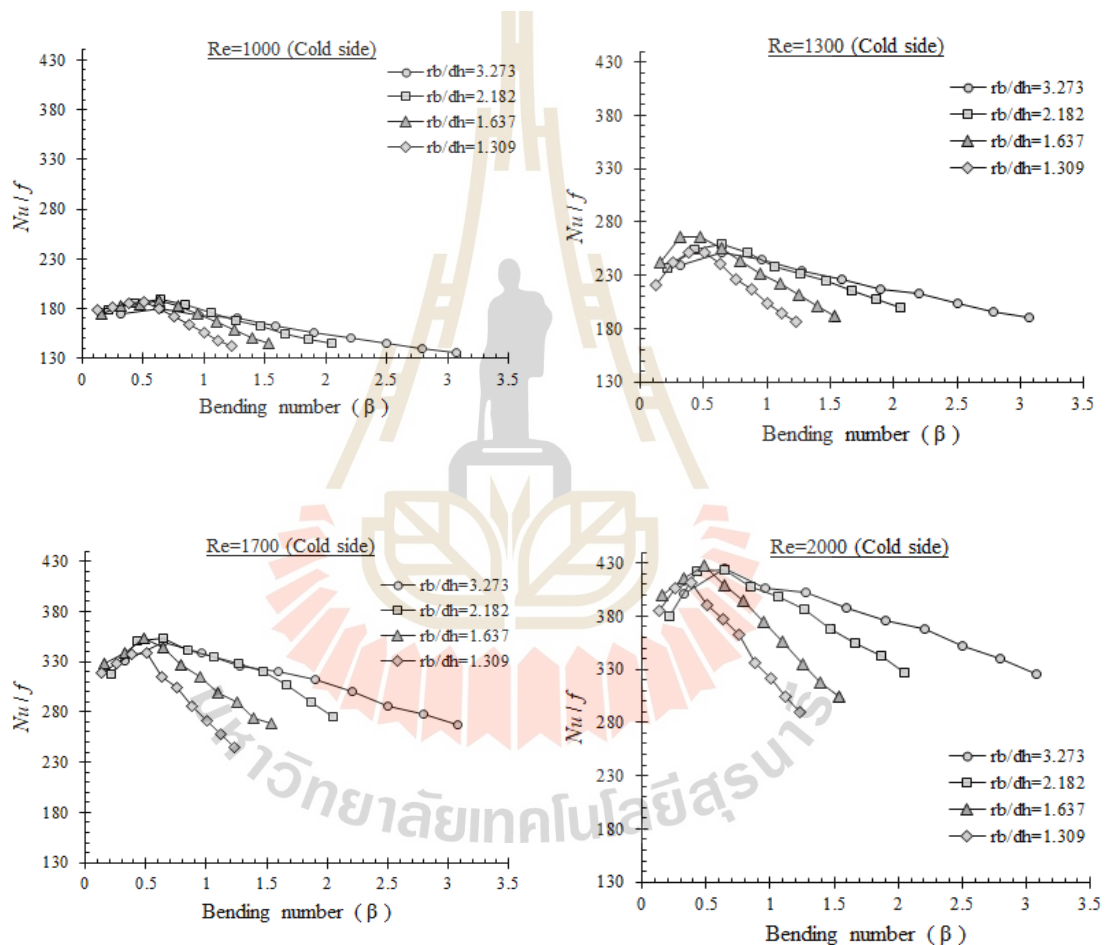


Figure 4.22 Nu/f at various bending number.

The β values ranging from 0.12 to 0.64 consistently show relatively higher Nu/f ratios compared to other numbers for most cases. At lower β , there is an initial increase in Nusselt numbers. The friction factor does not increase proportionally with the heat transfer rate, leading to a higher Nu/f ratio in the initial range of bending number. This

suggests efficient heat transfer relative to the pressure drop at lower number. As the β increases, Nusselt numbers continue to rise steadily, reflecting further improvement in heat transfer due to increased turbulence and mixing. The friction factor starts to increase more significantly, reducing the Nu/f ratio gradually. This indicates that while heat transfer continues to improve, the pressure drop becomes more substantial. The best thermal-hydraulic performance, characterized by the Nusselt number to friction factor ratio (Nu/f), is observed at β values of 0.64 for r_b/d_h ratios ranging from 1.637 to 3.273. For $r_b/d_h = 1.309$, the best performance is observed at β values of 0.4 for high Reynolds numbers (Re) and 0.5 for low Re . At high Re (turbulent flow), a β of 0.4 optimizes the thermal-hydraulic performance by providing sufficient disruption without excessive friction losses. At low Re (laminar flow), a β of 0.5 effectively enhances heat transfer by disrupting the smooth flow, with the increase in friction losses being manageable. This balance ensures the best thermal-hydraulic performance (Nu/f) across different flow conditions. The thermal-hydraulic performance (Nu/f) in zigzag channels is influenced by both the r_b/d_h ratio and the bending angle (β). Channels with appropriate r_b/d_h ratios and β values can optimize heat transfer efficiency by maximizing surface area and promoting effective mixing, while minimizing friction losses. Understanding and controlling these parameters are crucial in designing zigzag channels for various applications where heat transfer efficiency is critical.

4.7 Analysis of Local Performance with Different Bending Number

From the Nu/f ratio, β values around 0.4 to 0.64 consistently show relatively higher Nu/f ratios compared to other numbers for most cases. Therefore, these number would be ideal candidates for further local analysis. Focusing on these near-optimal β values allows for a more targeted investigation into the mechanisms driving enhanced thermal-hydraulic performance. The r_b/d_h ratio of 2.182 was chosen to analyze near-optimal β values for local flow characteristics. This approach provides valuable insights for the design and optimization of zigzag channel heat exchangers.

From Figure 23(a), it is observed that the higher β generally yields higher heat transfer compared to the lower β . Increased bending numbers (β) promote more effective heat transfer, due to the creation of secondary flows and enhanced fluid

mixing. Variations in heat transfer along the flow direction are influenced by factors such as flow velocity, turbulence, and thermal gradients. These factors induced by the channel's geometric complexity.

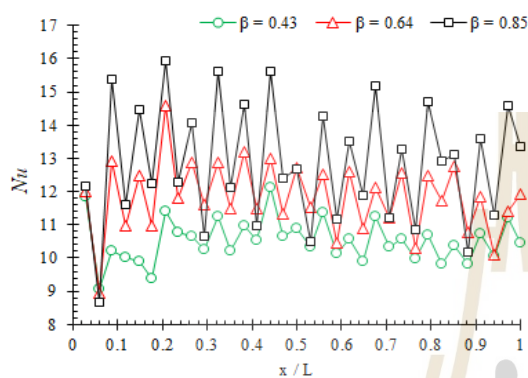
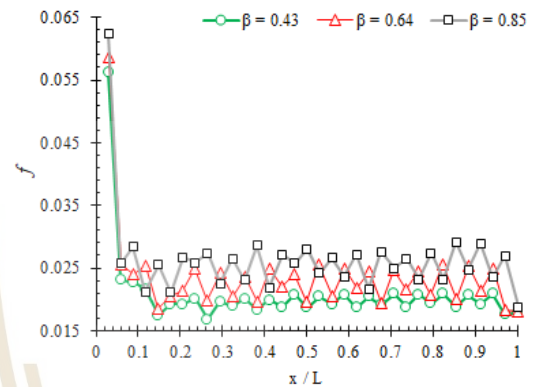
(a) Nusselt number (Nu)(b) Friction factor (f)

Figure 4.23 Distribution of Nu and f along the flow direction for various β .

The analysis of the friction factor, as shown in Figure 4.23(b), indicates that higher bending numbers (β) lead to increased friction factors. This is primarily due to the curvature associated with larger β values, which causes the flow to deviate from a smooth trajectory as shown in Figure 4.24. Such deviations create disturbances in the flow, including the formation of vortices and eddies, which result in additional frictional losses. These disturbances significantly affect the velocity and pressure distribution within the channel, causing fluid particles to encounter greater resistance as they move through these turbulent regions. Consequently, this increased resistance contributes to higher frictional losses along the length of the channel.

Figure 4.25 represents the local thermal hydraulic performance, illustrating how the bending number in channel designs significantly influences system performance through the Nu/F ratio. At $\beta = 0.64$, the Nu/F ratio is maximized, promoting effective turbulence and efficient heat transfer. In contrast, at $\beta = 0.43$, the ratio is low to moderate due to laminar flow conditions. Additionally, at $\beta = 0.85$, the ratio decreases because of flow separation and increased pressure losses, leading to unstable flow and reduced thermal hydraulic performance. Therefore, optimizing the bending

number is essential for balancing heat transfer efficiency and pressure drop in zigzag channel PCHes.

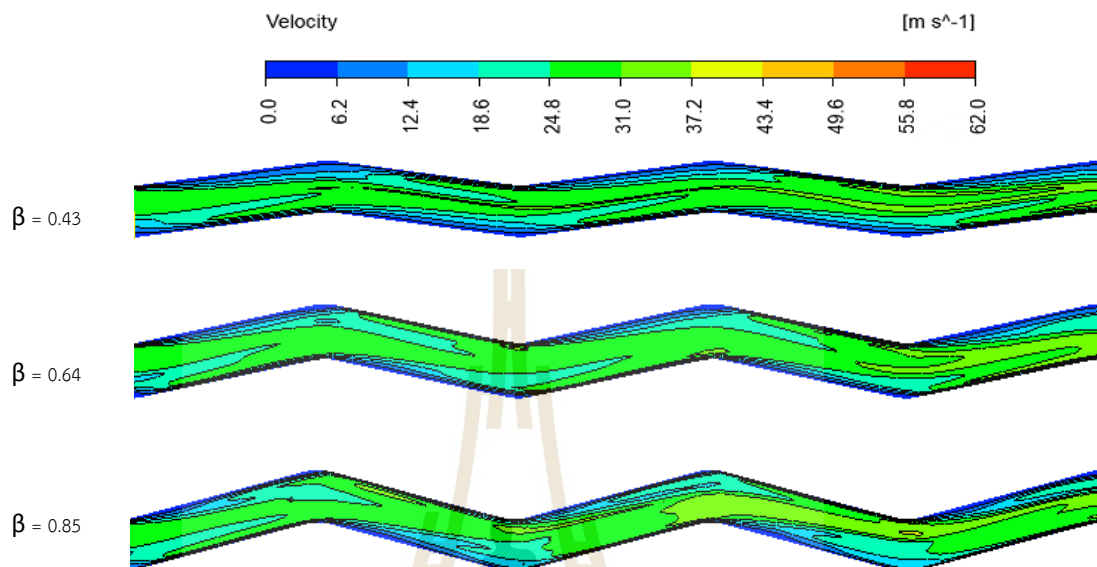


Figure 4.24 Velocity distribution along the flow direction for the various bending number (plane location: center of the semicircular channel).

4.8 Development of Nusselt Number and Friction Factor Correlation

Despite having the same hydraulic diameter on both sides in Printed Circuit Heat Exchangers (PCHes), the pressure factors and heat transfer can differ for the hot and cold sides. This discrepancy can be attributed to the distinct geometrical features and flow dynamics within the channels. Pressure factors and heat transfer are crucial in determining the efficiency of a PCHE. The empirical equations were calculated by various geometrical parameters such as hydraulic diameters, angles of the zigzag pattern, pitch of channel length, bend radius and bending number.

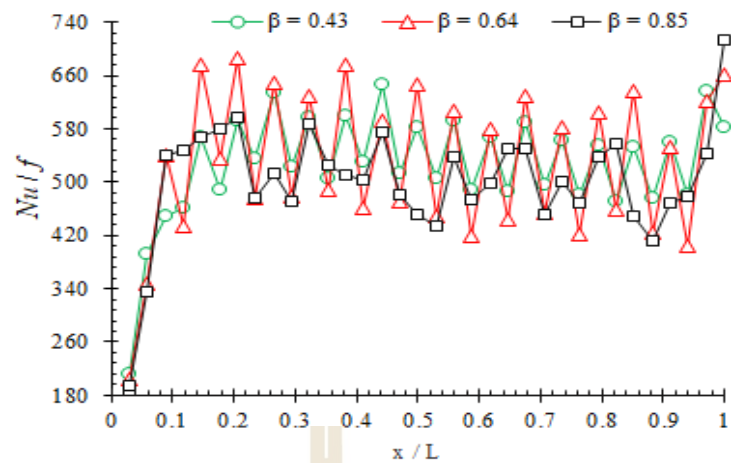


Figure 4.25 Distribution of Nu/f along the flow direction for various β .

4.8.1 Development of Nusselt number Correlation

In zigzag channels, fully-developed laminar flow is not achieved, leading to a Nusselt number that does not stabilize at a constant value, even under laminar periodic conditions. Instead, Nusselt numbers are mainly influenced by the zigzag channel geometries increase with higher Reynolds numbers. Therefore, the Nusselt number correlations were structured as (Torre et al., 2021):

$$Nu = C_1 \times Re + C_2 \quad (4.12)$$

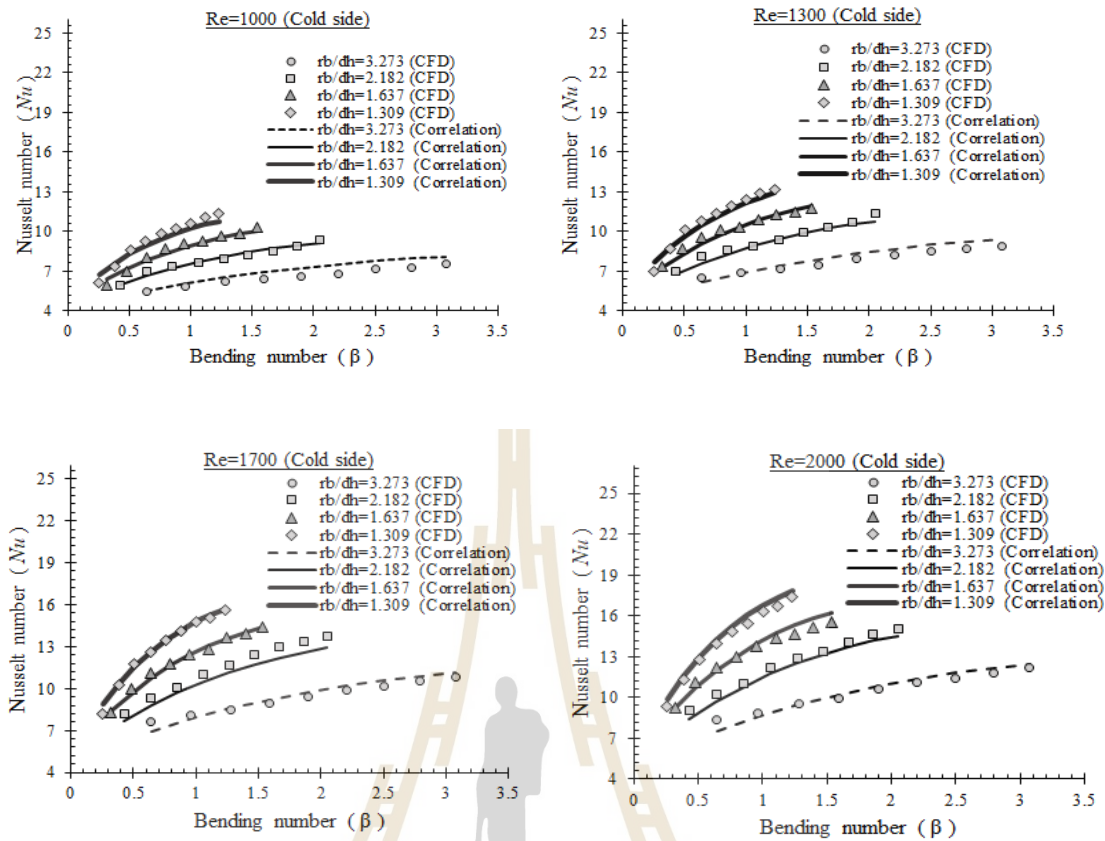


Figure 4.26 Correlation and CFD (Nu - β) data comparison (cold side).

The Nusselt number depends solely on the Reynolds number and geometric parameters because the Prandtl number does not change with helium temperature and pressure. The Prandtl number is the ratio of momentum diffusivity to thermal diffusivity. It is determined by the fluid's dynamic viscosity, specific heat, and thermal conductivity. The dependency of the Nusselt number correlation on the Prandtl number is not necessary, as the Prandtl number of helium remains nearly constant around 0.66 (Kim et al., 2009; Manglik & Bergles, 1995; Torre et al., 2021). The model coefficients can be presented as follow:

$$C_1 = F(\alpha, d_h, r_b, \beta) \cong K_1 \times f_1(\alpha) \times f_2(r_b / d_h) \times f_3(\beta) \quad (4.13)$$

$$C_2 = F(\alpha, d_h, r_b, \beta) \cong K_2 \times f_4(\alpha) \times f_5(r_b / d_h) \times f_6(\beta) \quad (4.14)$$

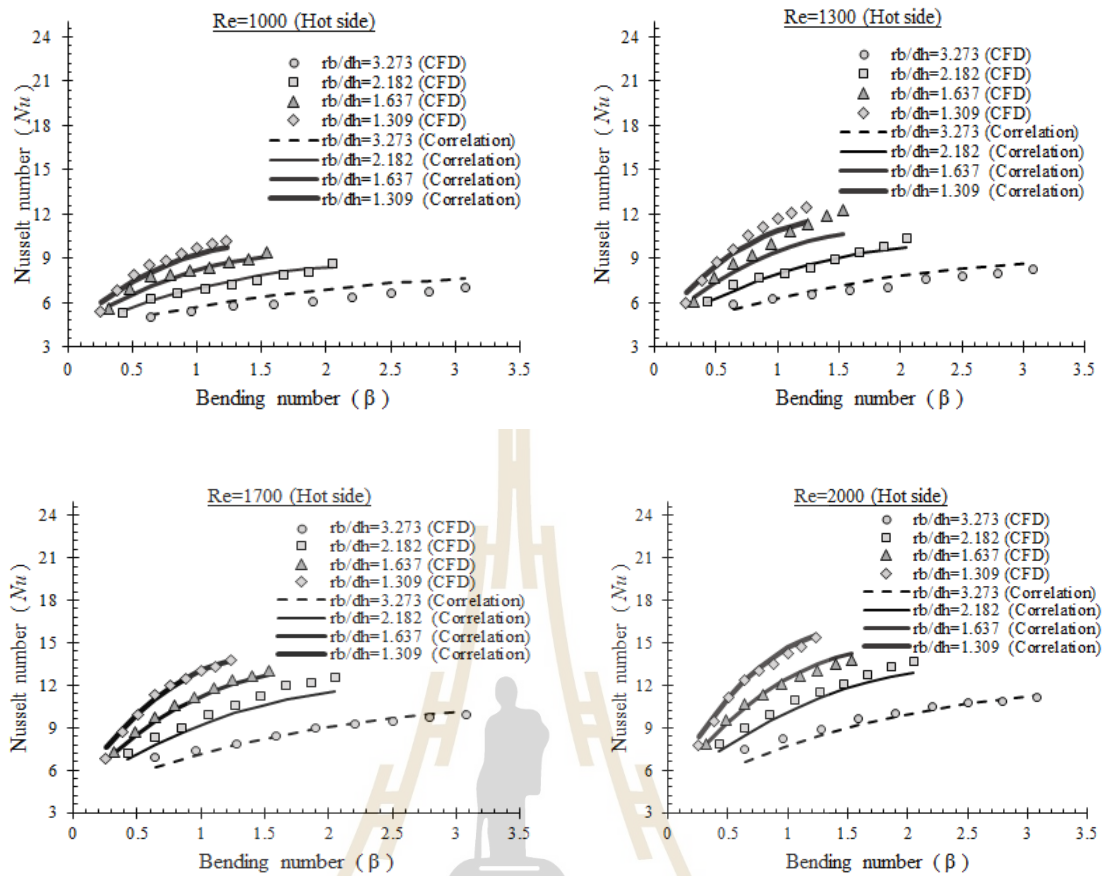
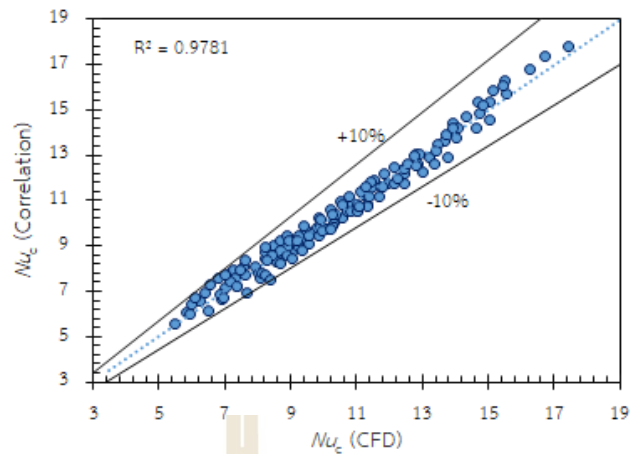


Figure 4.27 Correlation and CFD (Nu - β) data comparison (hot side).

The dimensionless functions f_1 - f_6 are dependent on specific parameters. Each function determines how a corresponding dimensionless group influences the Nusselt number. The interior-point algorithm was employed to calculate the coefficients for a model that predicts values based on several input parameters. This method ensures robust and efficient optimization of the model parameters, achieving the best fit for the given data while accommodating nonlinearities and constraints. The Nusselt number correlation was developed and is expressed by Eq. (4.15) and Eq. (4.16).

(a) cold side



(b) hot side

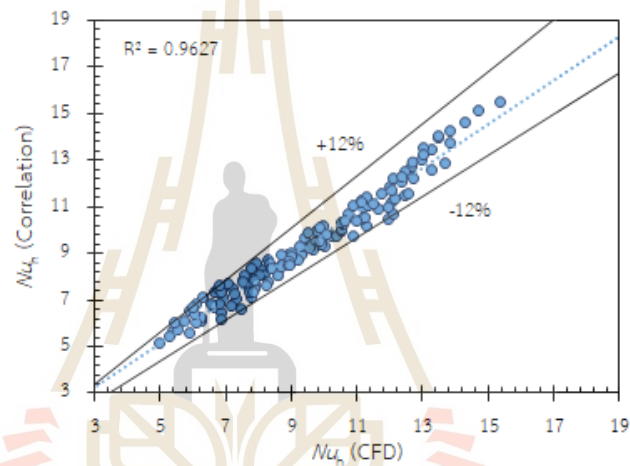


Figure 4.28 Friction factor comparison between correlations and CFD data.

Figures 4.26 and 4.27 present a comparative analysis of the Nusselt number (Nu) and bending number (β) derived from both correlation equations and Computational Fluid Dynamics (CFD) simulations. The comparison reveals that the correlation equations closely match the CFD simulation results, with a relative deviation of $\pm 10\%$ for the cold sides and $\pm 12\%$ for the hot sides. The linear regression model developed, as shown in Figure 4.28, further supports this analysis. The R-squared values for the model are 0.9781 for the cold side and 0.9627 for the hot side. These high R-squared values indicate a strong relationship between the CFD and correlation data, suggesting that the independent variables used in the model are effective predictors of the dependent variables.

$$Nu_c = 0.0016 \beta^{3.428} \alpha^{-2.836} \left(r_b / d_h \right)^{-3.9484} Re + 3.816 \alpha^{0.0285} \quad (4.15)$$

$$Nu_h = 0.0006 \beta^{4.8547} \alpha^{-4.17} \left(r_b / d_h \right)^{-5.355} Re + 4.1355 \alpha^{0.05745} \quad (4.16)$$

$$1000 \leq Re \leq 2000, 6^\circ \times \frac{\pi}{180} \leq \alpha \leq 30^\circ \times \frac{\pi}{180}, 1.309 \leq \frac{r_b}{d_h} \leq 3.273, 0.257 \leq \beta \leq 3.075$$

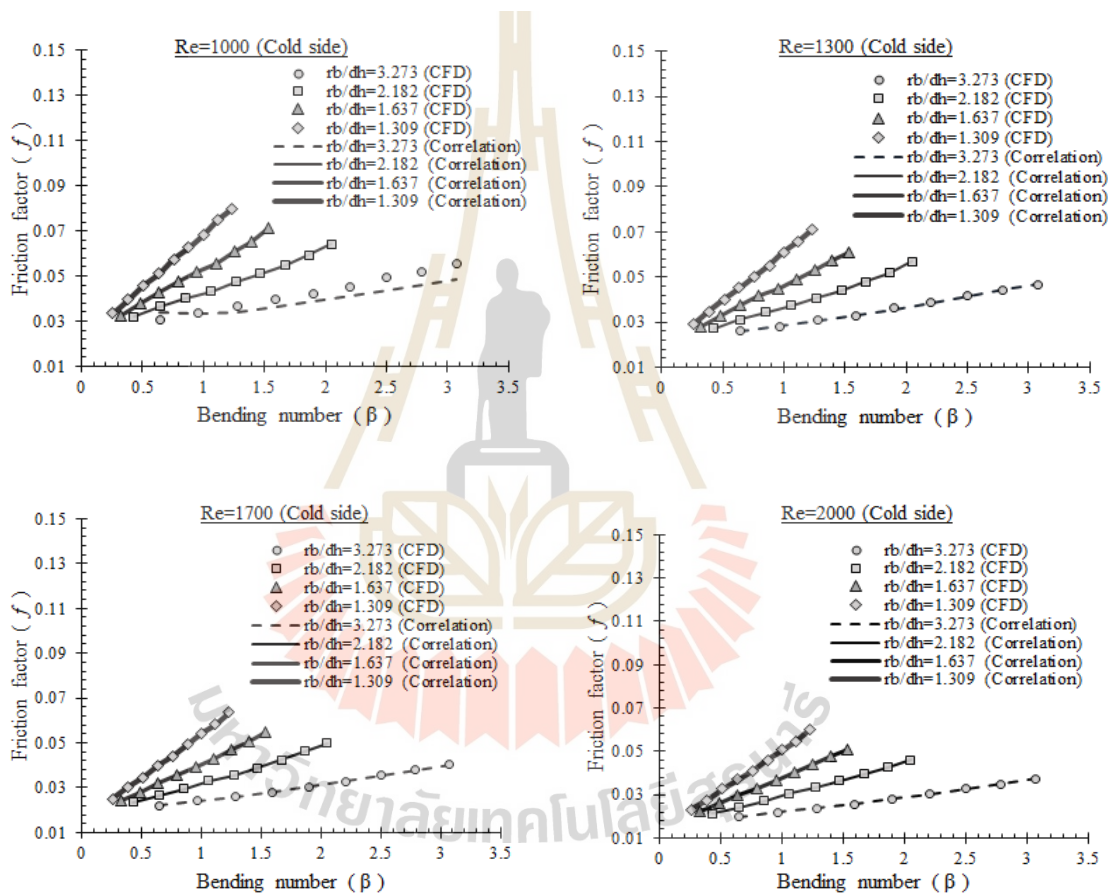


Figure 4.29 Correlation and CFD ($f-\beta$) data comparison (cold side).

4.8.2 Development of Fanning Friction Factor Correlation

The variation of friction losses with the Reynolds number in the laminar regime can be described as proposed by researchers (Kim et al., 2009; Torre et al., 2021; Yoon et al., 2017), following the form $f \times Re = C_1 \times Re + C_2$. The friction factor

correlations were derived using a procedure similar to that used for the Nusselt number correlations. The Nusselt number correlation was developed and is expressed by Eq. (4.17) and Eq. (4.18).

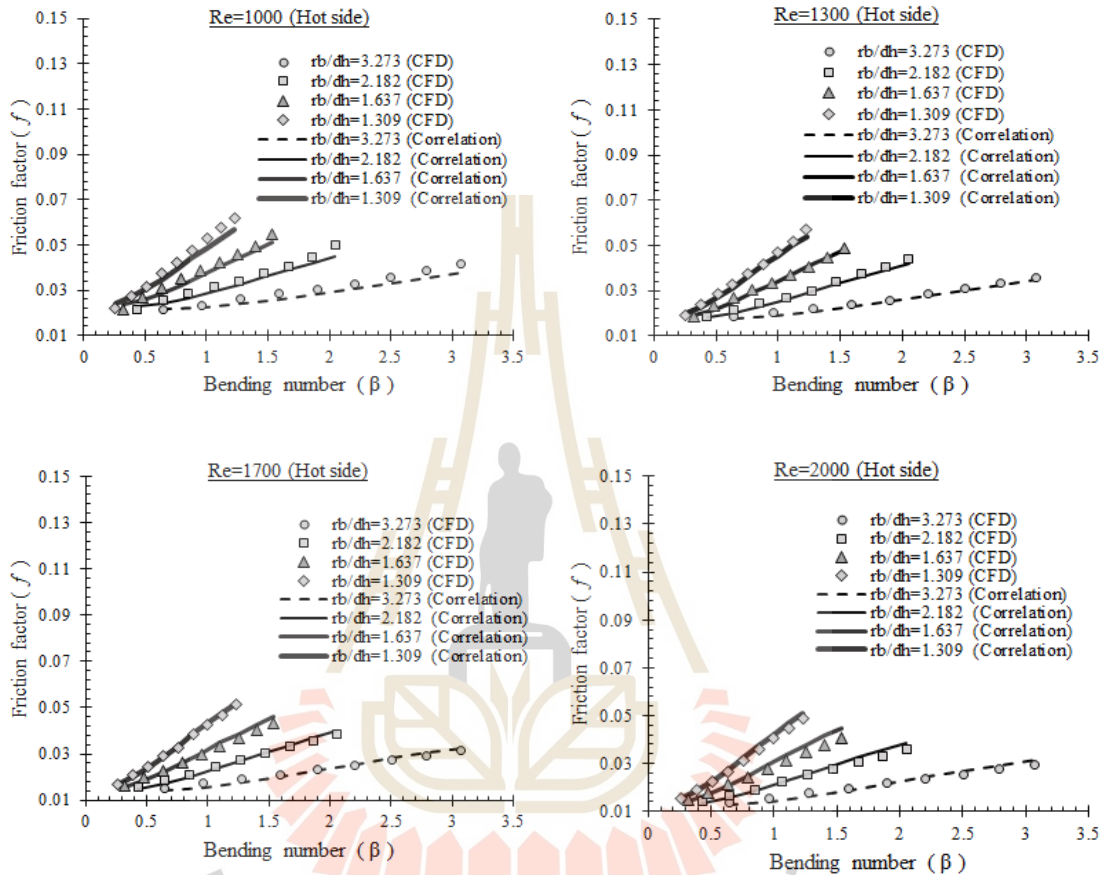


Figure 4.30 Correlation and CFD (f - β) data comparison (hot side).

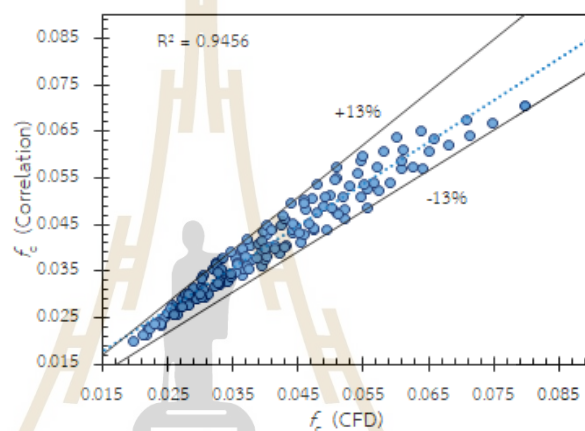
$$f_c = \alpha^{-4.4808} \left(0.0052\beta^{5.7553} \left(\frac{r_b}{d_h} \right)^{-6.289} + \frac{9.98715\alpha^{4.01913}}{Re} \right) \quad (4.17)$$

$$f_h = \alpha^{-4.6965} \left(0.0037\beta^{6.1318} \left(\frac{r_b}{d_h} \right)^{-6.7405} + \frac{9.9989\alpha^{4.4265}}{Re} \right) \quad (4.18)$$

$$1000 \leq Re \leq 2000, 6^\circ \times \frac{\pi}{180} \leq \alpha \leq 30^\circ \times \frac{\pi}{180}, 1.309 \leq \frac{r_b}{d_h} \leq 3.273, 0.257 \leq \beta \leq 3.075$$

Figures 4.29 and 4.30 present a comparative analysis of the friction factor (f) and bending number (β) derived from both correlation equations and CFD data. The comparison reveals that the correlation equations closely match the CFD simulation results, with a relative deviation of $\pm 13\%$ for the cold sides and $\pm 10\%$ for the hot sides. From the linear regression analysis, the R-squared values for the model are 0.9456 for the cold side and 0.9269 for the hot side in Figure 4.31. These high R-squared values indicate a strong relationship between the CFD and correlation data.

(a) cold side



(b) hot side

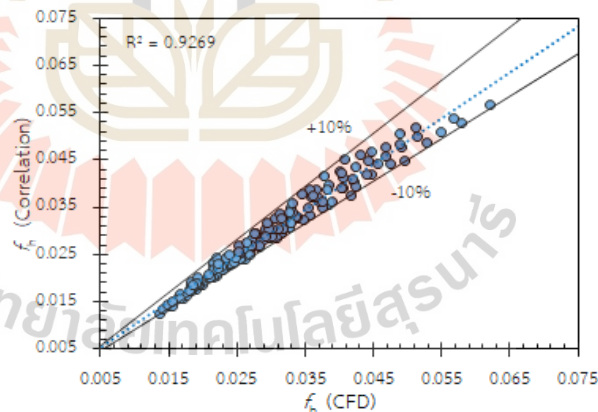


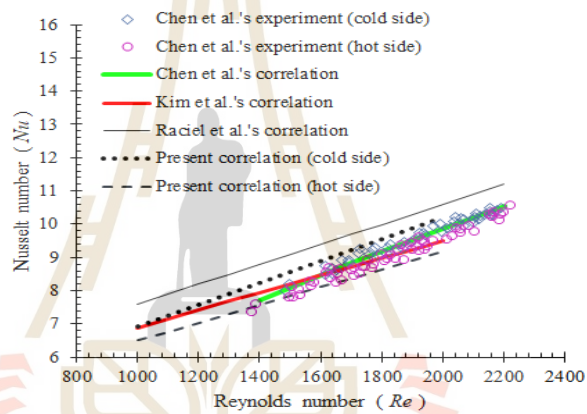
Figure 4.31 Friction factor comparison between correlations and CFD data.

4.8.3 Verification of Correlations for Friction Factor and Nusselt Number

To validate the correlations obtained for the Nusselt number and Fanning friction factor for zigzag channel geometries, comparisons were carried out between correlations (Chen et al., 2016; Kim & No, 2013) (Torre et al., 2021), experiments (Chen, Sun, & Christensen, 2019), and present correlation.

In figure 4.32a, the present Nusselt number correlation shows a maximum deviation of 5% when compared with both Chen et al.'s PCHE experimental and correlation data, and 5% when compared with Kim et al.'s correlation. The proposed correlation applies to a wider range of Reynolds numbers and gives accurate results throughout this range. It shows good accuracy. However, there is a maximum deviation of 10% on the cold side and 15% on the hot side compared to Racieli et al.'s correlation. These differences are caused over the range of geometric designs. Racieli et al.'s correlation consider the variation of the geometric features in CFD-based simulations.

(a) Nusselt number



(b) Friction factor

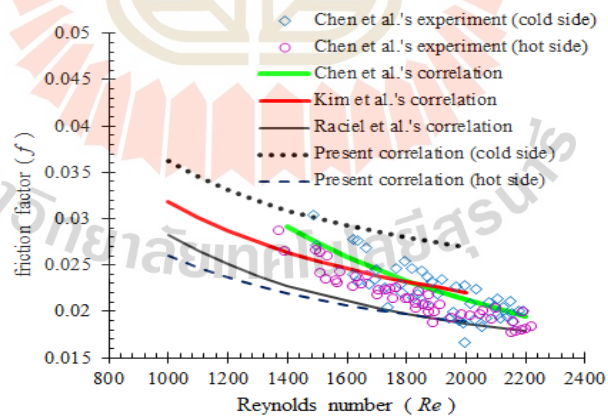


Figure 4.32 Comparison of Experimental Data and Correlations for f and Nu .

In figure 4.32b, the present friction factor correlation shows a maximum deviation of 20% on both cold side and hot side when compared with Chen et al.'s PCHE experimental and correlation data, and 15% on cold side and 20% on hot side

when compared with Kim et al.'s correlation. However, the present correlation overestimated about 28% on deviation cold side from the Racié correlation. The current CFD model focused on the core length of the zigzag channel, whereas the Racié CFD-based correlation considered both the entrance horizontal channel section and the zigzag channel core. Flow losses in the entrance section can lead to significant deviations in the friction factor predictions.

The proposed new correlation demonstrates effectiveness in predicting the flow and heat transfer characteristics of zigzag channel PCHes. However, the current correlation can be accurately predicted within an acceptable error margin using geometric parameters. The current correlation incorporates the effect of bending flow corresponding to bending number, new bending angle, the ratio of bend radius to hydraulic diameter and varying channel diameters. However, many researchers do not account for this effect in their studies. An important contribution was the development of more accurate correlations for calculating the Nusselt number and the Fanning friction factor in zigzag channels. These correlations were established as functions of geometric parameters and Reynolds number, enhancing predictive accuracy.

CHAPTER V

EVAPORATION PARAMETERS IN PRINTED CIRCUIT HEAT EXCHANGERS (PCHEs) FOR CRYOGENIC FLUID APPLICATION

Evaporation parameters in printed circuit heat exchangers (PCHEs) are critical for optimizing their performance in cryogenic fluid applications. PCHEs are highly efficient and compact, making them ideal for systems requiring precise thermal management, such as liquefied natural gas (LNG) processing and cooling systems. Key parameters include flow structural geometry, flow dynamics, pressure drops, and the thermal properties of cryogenic fluids. Understanding these factors is essential for enhancing the design, efficiency, and reliability of PCHEs in demanding cryogenic environments. This section focuses on the detailed analysis of these parameters to improve overall system performance.

5.1 Cross-Sectional Local Analysis of Two-Phase Flow in Printed Circuit Heat Exchangers During Cryogenic Fluid Evaporation

Cross-sectional local analysis of two-phase flow in printed circuit heat exchangers (PCHEs) is vital for understanding flow characteristics, heat transfer efficiency, and pressure drops. This analysis is essential for enhancing the design, efficiency, and reliability of PCHEs, especially in cryogenic applications. In this section, we examine phase transitions and flow behavior during the evaporation of cryogenic nitrogen, which provides insights necessary for optimizing PCHE performance in these demanding applications. In section 3.8.2, the validated model was used to simulate nitrogen evaporation flow patterns in PCHE minichannels as shown in Figure 3.8. The mesh structure uses as shown in Figure 3.9. The local analysis focused on the second case of a transient test. The inlet mass flowrate of the entire PCHE model, temperature, pressure, and heat source were 205.1 kg/hr, 102.85 K, 1.59 MPa, and 20.6 kW. In the simulation, the outlet pressure was set to zero, while the inlet was specified as a fully liquid condition. The diffusion-bonded core and scanning electron microscopy images

of the PCHE core, along with the two-phase nitrogen experimental setup and the design of the heat plates, are illustrated in Appendix A, Figures A.9 to A.11.

Cross-sectional views were taken at different vapor qualities to analyze the distribution of two-phase flow along the channel, as shown in Figure 5.1. Initially, the gas phase at the sharp corners emerged where the lower and upper surfaces of the channel intersected in the flow direction. Subsequently, it extended towards the middle of the channel surface. The liquid phase from the heated wall evaporated and transitioned into the gas phase. The observation revealed an increasing vapour presence along the upper channel and a decrease in liquid nitrogen content along the lower channel due to gravity effects.

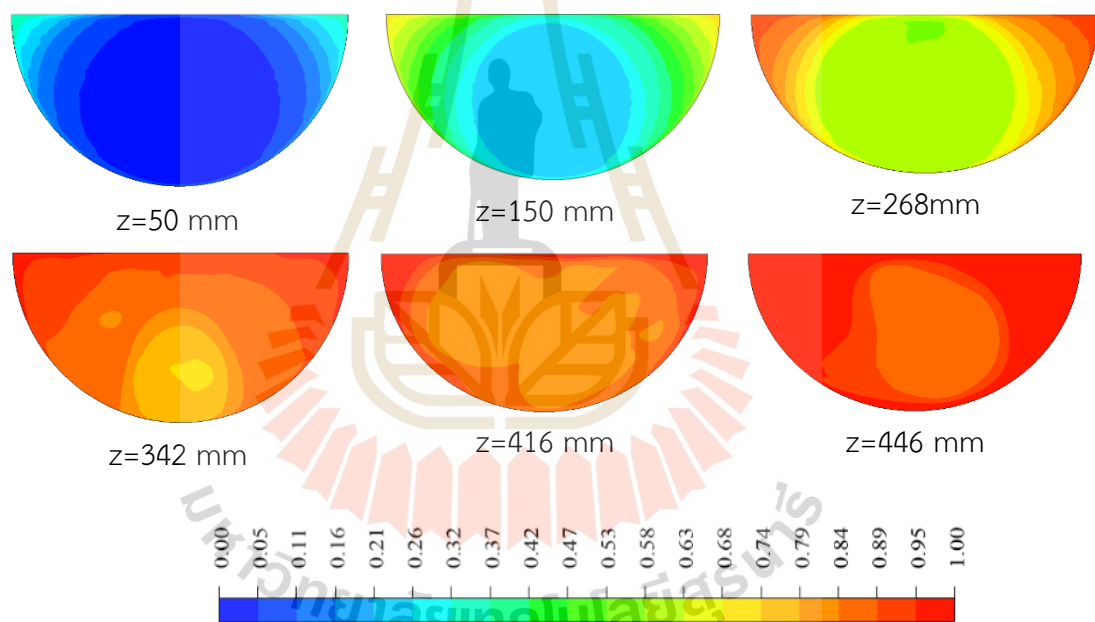


Figure 5.1 Illustrates vapour-phase distribution at different cross-sectional views (a number of 0 represents the liquid phase, while a number of 1 corresponds to the fully vapor phase).

Figure 5.2 illustrates the velocity vectors representing the vapour phase pattern within the cross-sections. Flow velocity was significantly low at the sharp corners, corresponding to the initial emergence of the vapour phase. The application of heat flux to the fluid from the upper and lower surfaces led to earlier vaporization near

these surfaces compared to the central region. The study revealed the emergence of multiple vortices near the phase transition interface. This occurrence was prompted by the rapid convection of nitrogen from the vapour to the liquid-vapour interface, a result of the preferential evaporation of nitrogen, which is not uniform. As a result, the liquid-vapour flow exhibited vortex flow, resulting in improved heat exchange efficiency. The interface tension between phases depends on their composition, resulting in attraction or repulsion. Particularly, the non-uniform evaporation rate drives movement from the side with high evaporation flux to that with low evaporation flux. This process reduced energy dissipation linked to the inherent fluid flow caused by evaporation. Over long distances, the vapour field undergoes substantial changes due to increased evaporation. Although the radial velocity component increases, vortices are still present. Due to strong convection, a wake region with a recirculation vortex becomes noticeable.

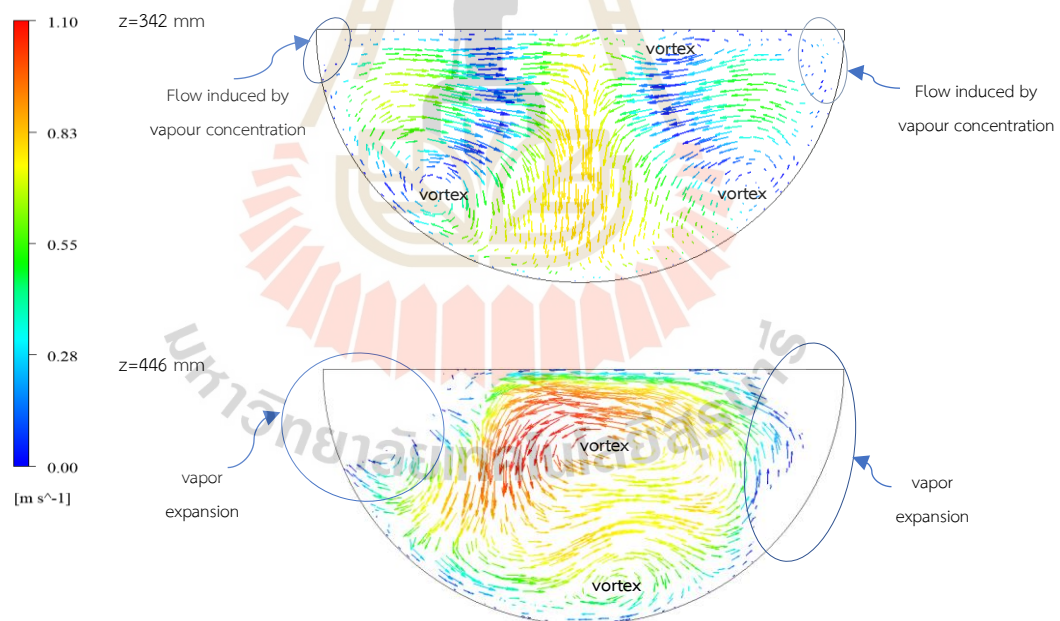


Figure 5.2 Behaviours velocity of a vapour phase pattern inside undergoing evaporation.

This study examines the interesting dynamics of evaporation processes, interpreting how and why flow patterns transition from symmetry to asymmetry. Initially, under uniform conditions, symmetric flow structures emerge due to consistent

droplet shapes and substrate properties at $z = 50\text{--}268$ mm in Figure 5.1. As the evaporation process progresses, it becomes influenced by external factors and property gradients, leading to the development of complex and asymmetric flow structures. These asymmetrical flow fields are, in part, attributed to non-uniform heat distribution, fluid property variations, and channel geometry effects, causing non-uniform evaporation rates and differences in evaporation mass flux, as shown in Figure 5.2. At $z = 342\text{--}446$ mm in Figure 5.1, the vapour-mediated interactions further contribute to the asymmetry by introducing concentration gradients within the liquid phase, leading to long-range attraction or repulsion forces and shifts in flow patterns. The introduction of a volatile liquid phase disrupts the existing symmetry, initiating significant changes in the vapour field dynamics and further accentuating the asymmetry. In essence, the complex interplay of external influences and vapour-mediated interactions throughout the evaporation process accounts for the transition from initial symmetry to asymmetry in flow patterns.

5.2 The Effect of Inlet Temperature and Pressure on Cryogenic Fluid Evaporation in Minichannels

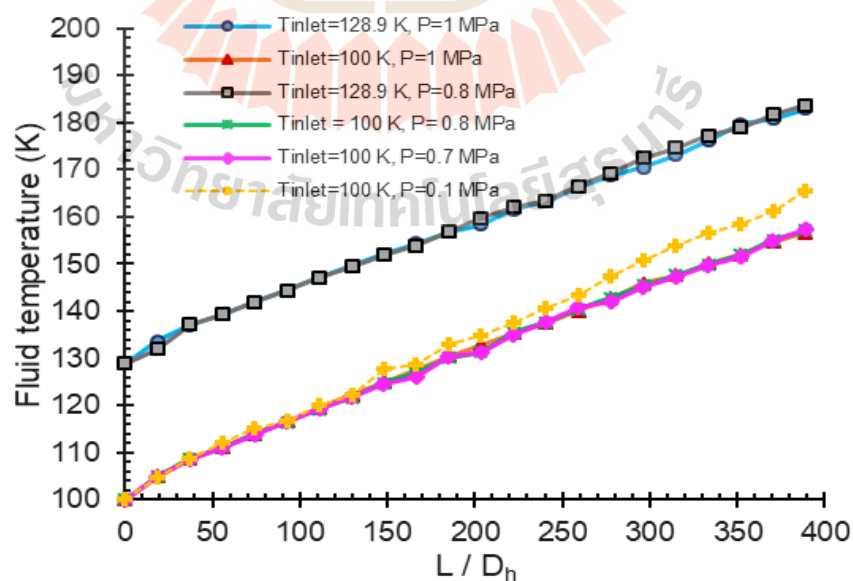


Figure 5.3 Effect of inlet temperature and pressure on temperature distribution.

Understanding the behavior of cryogenic fluid evaporation in minichannels is crucial for designing efficient cooling systems in cryogenics applications. The pressure effect on the evaporation process is influenced by the inlet temperature of the liquid. By analyzing the inlet temperature and pressure conditions and understanding the flow regimes, the design and performance of cryogenic fluid systems in minichannels can be significantly improved. This section studied the effect of pressure and inlet temperature on cryogenic fluid evaporation in minichannels. The validated model was applied in this cryogenic methane evaporation. The channel length was 210 mm and the methane was saturated liquid state at the inlet. The inlet temperatures (T_{inlet}) were 128.9 K and 100 K. The properties fluid pressures were 1 MPa, 0.8 MPa, 0.7 MPa, and 0.1 MPa. The inlet mass flux and heat source were $4.7,666 \times 10^{-5}$ kg/s and 20.953 kW/m². In the simulation, the outlet pressure was set to zero, while the inlet was specified as a fully liquid condition

5.2.1 Analysis of Evaporation Temperature Distribution in Minichannels

The temperature profiles provided in figure 5.3 offer valuable insights into the behavior of cryogenic fluid evaporation under different inlet temperatures and pressures. Lower inlet temperatures result in a more significant temperature rise along the channel. At an inlet temperature of 128.9 K, the temperature differential was approximately 53.96 K at 1 MPa and 54.77 K at 0.8 MPa. At an inlet temperature of 100 K, the temperature differential was approximately 56.6 K at 1 MPa, 57 K at 0.8 MPa and 0.7 MPa, and 65.44 K at 0.1 MPa. This suggests that fluids entering at a lower temperature have a higher capacity for heat absorption, leading to more effective cooling. Lower pressures (0.1 MPa) facilitate a greater temperature increase, indicating enhanced evaporation efficiency. At 0.1 MPa, the fluid temperature differential reaches higher than in other cases, reflecting better heat transfer performance. In addition, the temperature distribution is more uniform at higher pressures, while lower pressures exhibit steeper temperature gradients. This implies that managing the pressure can control the temperature profile along the channel for optimized performance.

5.2.2 Analysis of Evaporation Pressure Distribution in Minichannels

A consistent pressure drop is observed along the length of the minichannels for all conditions as shown in Figure 5.4. This pressure drop is due to the

frictional losses and phase change processes occurring within the channel. At lower pressures (0.1 MPa), the fluid starts at a higher initial pressure at the channel entry and has a more gradual pressure drop along the channel length compared to higher pressures. This indicates that while the starting pressure varies, the relative pressure loss due to friction and phase change is consistent across different pressures. The areas where intermediate peaks in the heat transfer coefficients occur often correspond to regions where the pressure gradient changes more rapidly. This suggests a strong correlation between local pressure changes and heat transfer enhancements, likely due to the changes in flow regimes. The correlation of heat transfer and flow regime discussed in the next section.

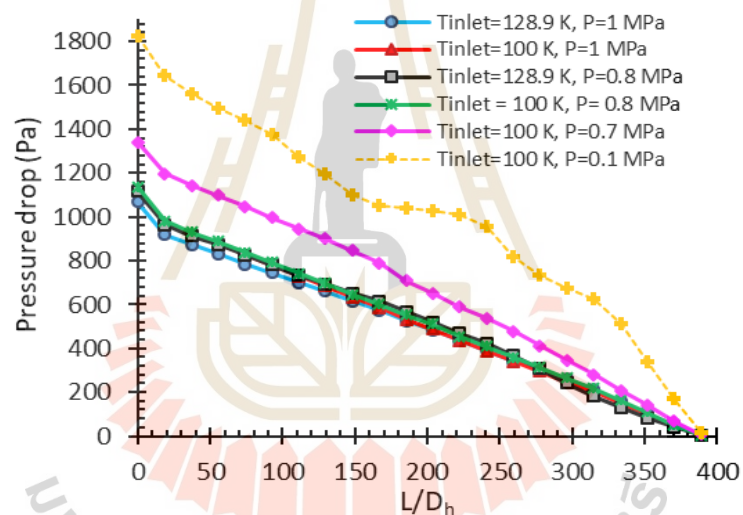


Figure 5.4 Effect of inlet temperature and pressure on pressure distribution.

Fluids entering at a lower temperature (100 K) initially experience higher energy states and dissipate more energy along the channel. Specifically, at 0.1 MPa, the fluid pressure significantly drops, showing significant energy dissipation and effective fluid phase change.

5.2.3 Evaporation Flow and Heat Transfer Mechanisms in Minichannels

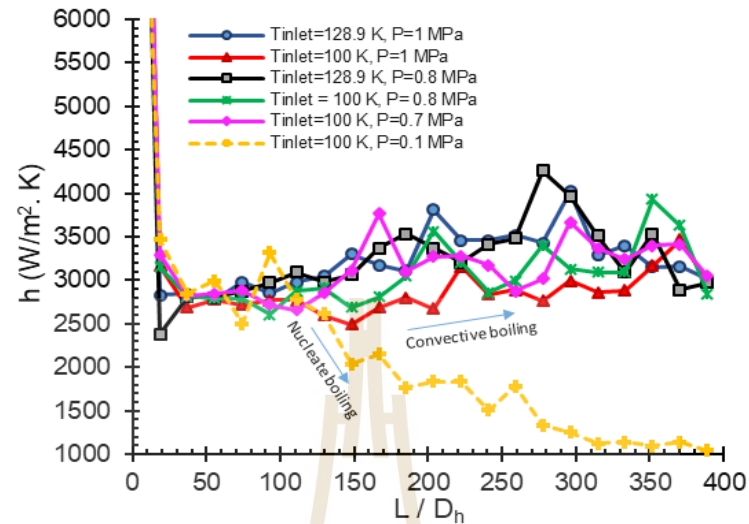


Figure 5.5 Effect of inlet temperature and pressure on heat transfer distribution.

As shown in the figure 5.5, the heat transfer coefficients along the length of the minichannels exhibited significant variation. Initially, the heat transfer coefficients generally decreased as the fluid progressed through the channel and started to evaporate. This trend is attributed to the decreasing thermal conductivity as the fluid transitions from the liquid to the vapor phase. Liquid phases have higher thermal conductivity compared to vapor phases, leading to reduced heat transfer efficiency as more vapor forms. Interestingly, there are intermediate peaks observed at various positions along the channel. These peaks likely correspond to regions where different flow patterns, such as bubbly, slug, or annular flows, dominate and enhance heat transfer. These flow regimes are characteristic of the conventional transcritical heating process, where the fluid transitions through various phases and flow structures, each with distinct heat transfer properties.

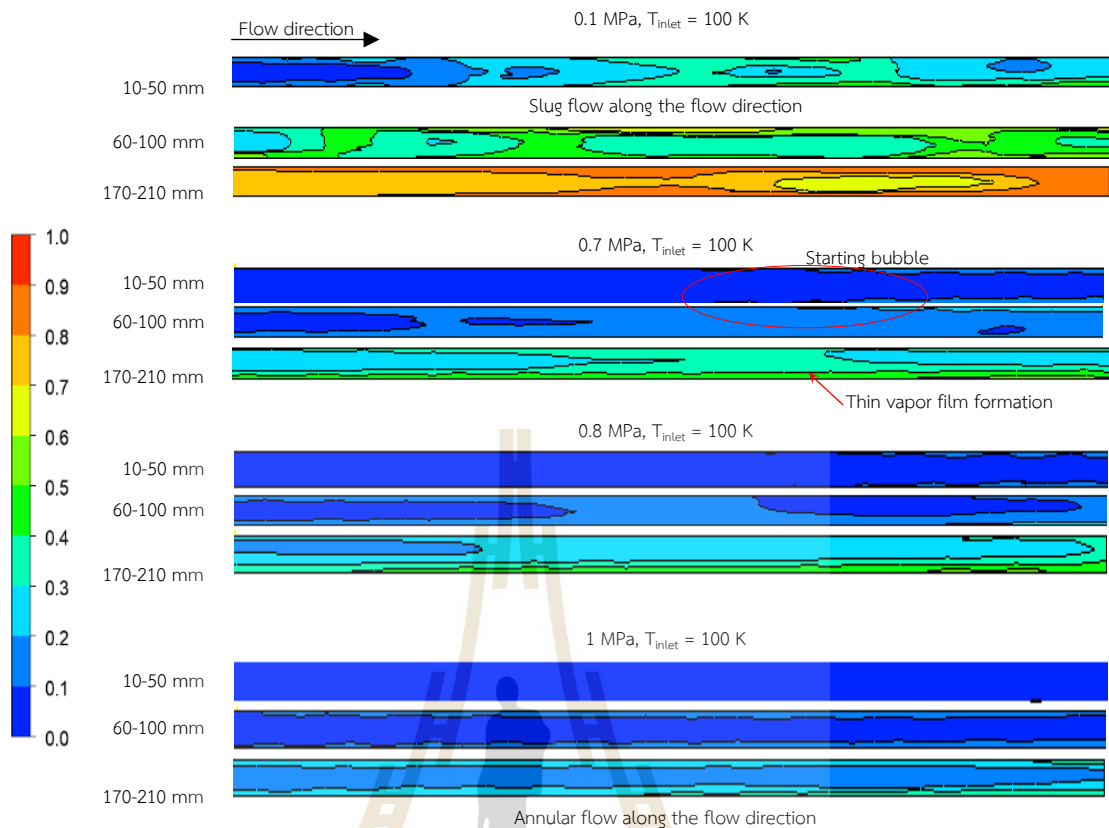


Figure 5.6 Flow patterns behavior with corresponding vapor quality at different pressure (a number of 0 represents the liquid phase, while a number of 1 corresponds to the fully vapor phase).

It was observed that the inlet temperature also influenced the heat transfer coefficients. Higher inlet temperatures (128.9 K) tended to produce higher initial heat transfer coefficients compared to lower inlet temperatures (100 K) in Figure 5.5. This is because a higher inlet temperature increases the initial thermal driving force, enhancing heat transfer. As the fluid absorbs heat and evaporates, the initial temperature difference plays a crucial role in determining the overall heat transfer rate.

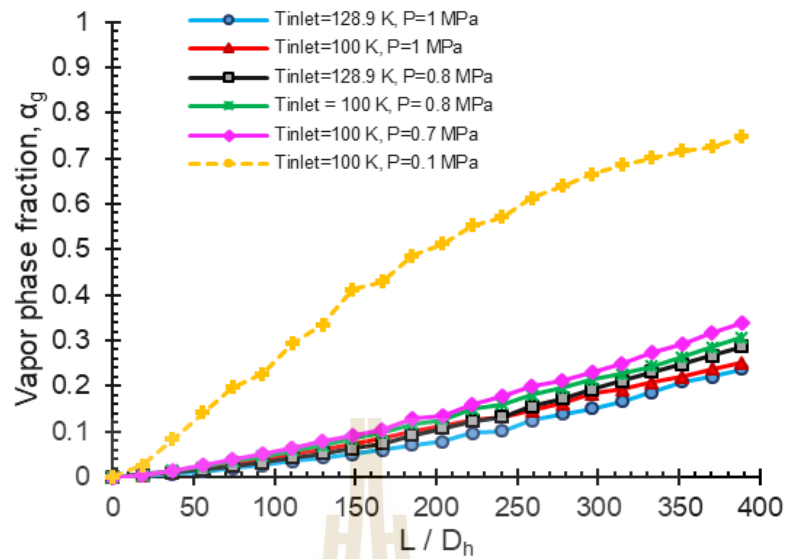


Figure 5.7 Vapor distribution of different inlet temperature and pressure.

In addition, the results showed that the heat transfer coefficient variation for transitional boiling flow along minichannels corresponded to two distinct heat transfer regimes. Figure 5.6 shows the flow of 0.1 MPa is obviously dominated by bubbly and slug flow modes, indicating the dominant nucleate boiling heat transfer regime. The heat transfer coefficient starts at the highest value and decreases monotonously along the channel as the gradual suppression of nucleate boiling occurs. At high inlet pressures (0.7–1 MPa), the heat transfer coefficient shows fluctuations but generally increases slightly along the flow direction. As shown in figure 5.6, annular flow dominates at high pressure, and the gas film occupies the area the area near the wall. The gradual thinning of the annular gas film increases the heat transfer coefficient along the channel.

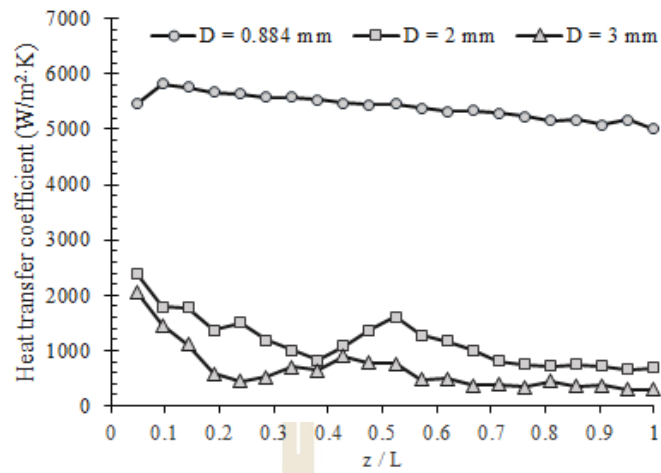


Figure 5.8 Impact of channel diameter on local evaporation heat transfer coefficient.

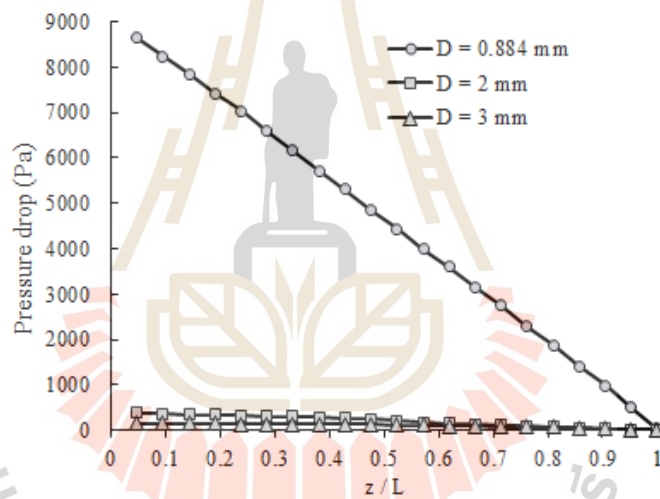


Figure 5.9 Impact of channel diameter on pressure distribution.

Figure 5.7 illustrates the distribution of vapor with varying pressure and inlet temperature. As the fluid progresses through the minichannels, the quality increases, indicating the gradual phase transition from liquid to vapor. Higher inlet temperatures (128.9 K) tend to result in a slower initial increase in vapor quality compared to lower inlet temperatures (100 K). This can be attributed to the higher thermal driving force at lower temperatures, which accelerates the phase transition process. Lower pressure conditions generally show a higher fluid quality at the same channel positions compared to higher pressure conditions. This is due to the lower

boiling point at reduced pressures, which promotes more rapid evaporation. However, at very low pressure (0.1 MPa), the heat transfer coefficient rapidly increases, suggesting an approach to complete evaporation. As shown in figures 5.5 and 5.6, the results of 0.1 MPa show a rapid decrease in heat transfer coefficients along the flow direction, likely due to a faster transition to vapor, which reduces the effective heat transfer area. The phase fraction data shows that lower pressures facilitate a more rapid phase change, leading to higher evaporation rates and earlier completion of the boiling process.

The intermediate peaks in heat transfer coefficients correspond to regions where the quality increases more rapidly. These peaks suggest the presence of different flow regimes that enhance heat transfer, such as slug or annular flows, which are effective in disrupting the thermal boundary layer and promoting phase change. Lower pressures and optimal inlet temperatures should be maintained to achieve higher quality and better heat transfer.

5.3 Effect of Channel Diameter on Evaporation

The effects of channel diameter from 0.884 mm to 3 mm on evaporation were explored at the inlet mass flow rate and heat source of $1.9,425 \times 10^{-4}$ kg/s and 18.523 kW/m². The inlet pressure was 0.1 MPa, and the saturation temperature was 100 K. In the simulation, the outlet pressure was set to zero, while the inlet was specified as a fully liquid condition

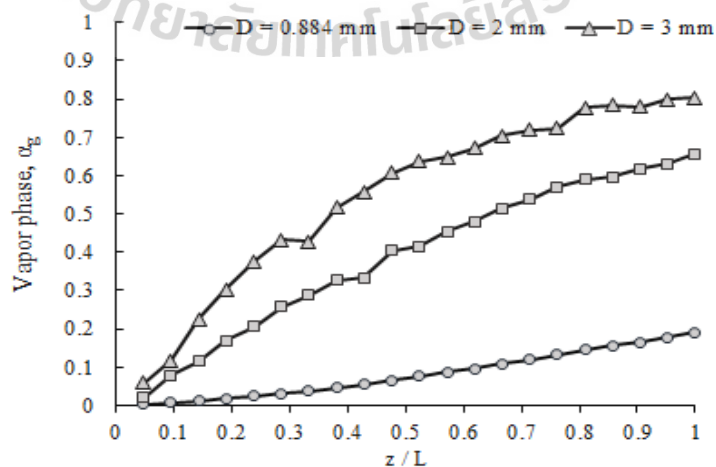


Figure 5.10 Impact of channel diameter on vapor phase.

Figure 5.8 shows the effects channel diameters on local evaporation heat transfer coefficient. The channel with a diameter of 0.884 mm exhibited the highest heat transfer coefficients due to its high heat transfer surface area to fluid volume ratio, and promoting effective thermal exchange between the liquid and the wall. Moreover, it also results in higher pressure drops in figure 5.9, as the confined space leads to higher fluid velocities and increased frictional resistance. In contrast, larger diameter channels exhibit the lowest heat transfer coefficients and pressure drops. The larger diameters have a lower heat transfer surface area to fluid volume ratio, which reduces heat transfer efficiency. The increased cross-sectional area leads to lower fluid velocities, which diminishes turbulence and mixing. Consequently, heat transfer is less effective. Additionally, the larger diameter supports higher vapor phases and complex flow patterns, further reducing heat transfer performance.

Figure 5.10 and figure 5.11 illustrate the vapor distribution and flow pattern. The annular vapor film flow pattern is observed at $D=0.884$ mm, with a central liquid core surrounded by a thin vapor film. It reduces vapor accumulation within the tube. This configuration ensures efficient evaporation and heat transfer while limiting the formation of large vapor bubbles. Additionally, the high pressure drops further aids in suppressing excessive vapor generation, contributing to a lower vapor phase and more stable flow conditions. The diameter channel $D=2$ mm supports bubbly and slug flow patterns and a significant vapor phase due to its smaller diameter, which enhances fluid velocity and mixing. This increased velocity and mixing lead to effective nucleation and growth of bubbles. The resulting turbulent conditions cause frequent interactions between the liquid and vapor phases, maintaining a substantial vapor presence and promoting the formation of bubbly and slug flow patterns. In contrast, the diameter channel $D=3$ mm has a larger cross-sectional area, leading to lower fluid velocities and reduced mixing. This larger diameter permits more extensive vapor formation, resulting in higher vapor phases. The flow pattern shifts from chunk flow, with large vapor bubbles or liquid chunks, to annular flow, where a thin liquid film forms around the walls with a central vapor core. This transition, combined with

reduced mixing and less efficient heat transfer, often causes dry out at the exit, where the liquid film may no longer absorb heat effectively.

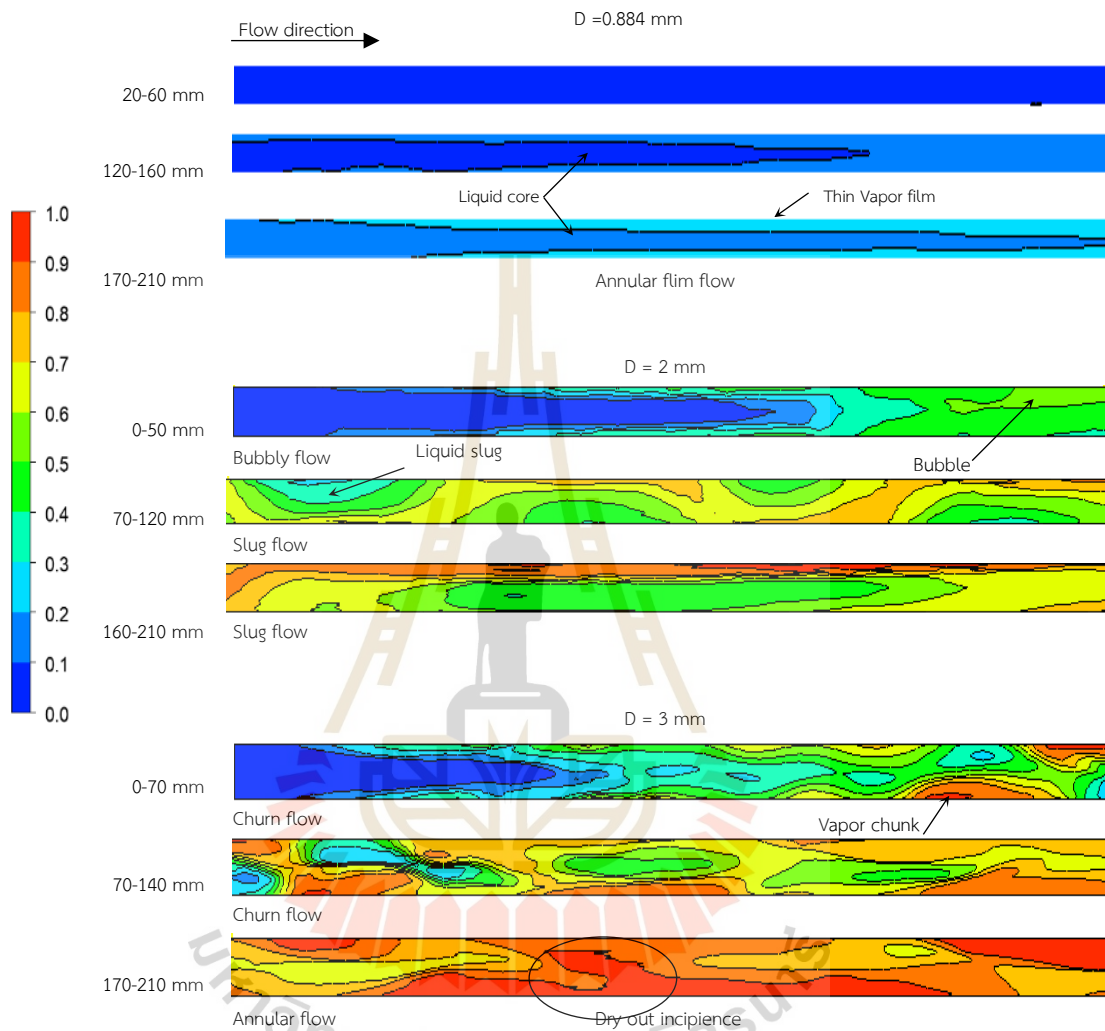


Figure 5.11 Flow patterns behavior with corresponding vapor quality at different channel diameter (a number of 0 represents the liquid phase, while a number of 1 corresponds to the fully vapor phase).

5.4 Effect of Channel Shape on Evaporation

From the analysis of channel diameters, it is clear that channel shape is crucial in evaporation as it directly influences heat transfer efficiency and fluid dynamics. Therefore, the zigzag channel and straight channel was analyzed for completed evaporation. The analysis was conducted using a channel diameter of 3 mm, with the

optimal bending angle of 6° for a zigzag channel. The geometric parameters were applied based on previous research (Aye et al., 2023). In the simulation, the outlet pressure was set to zero, while the inlet was specified as a fully liquid condition. At the inlet, the mass flow rate and heat source were set to 1.9425×10^{-4} kg/s and 18.523 kW/m², respectively. The inlet pressure was 0.1 MPa, and the saturation temperature was 100 K.

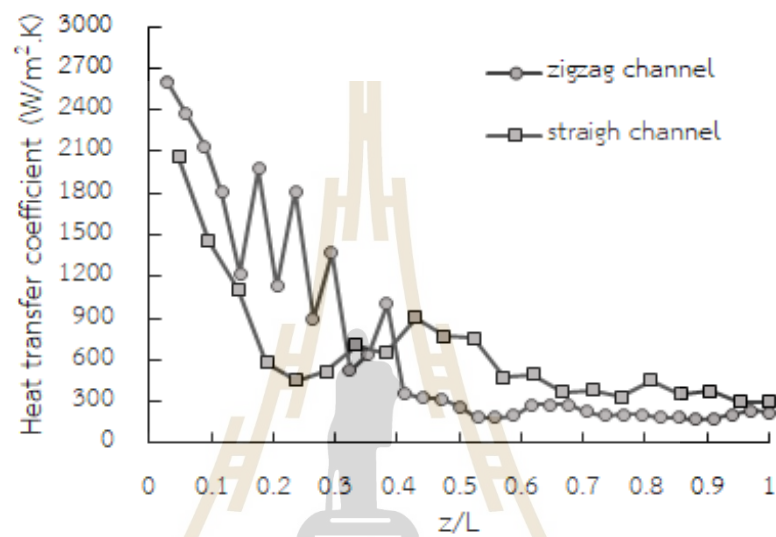


Figure 5.12 Impact of channel shape on evaporation heat transfer coefficient.

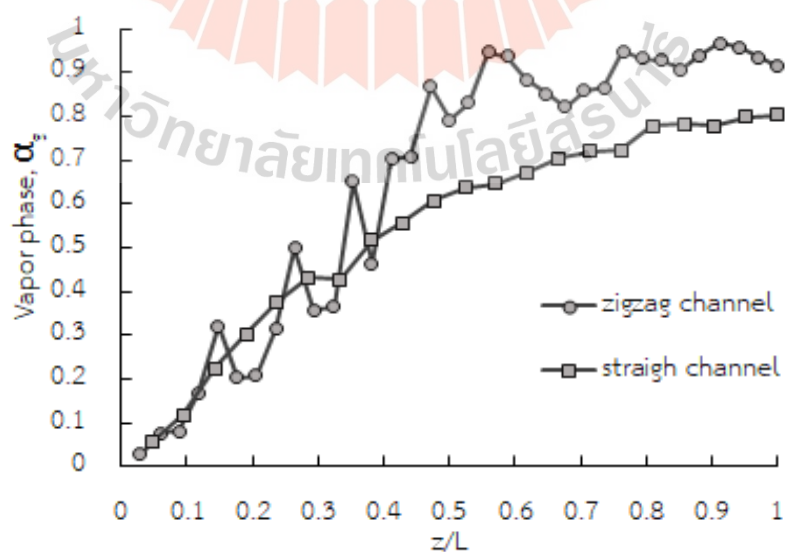


Figure 5.13 Impact of channel shape on vapor phase.

Figure 5.12 shows the variation of the heat transfer coefficient along the length of both the straight and zigzag channels. It is observed that both channels show high heat transfer coefficients at the beginning. The zigzag channel has a higher initial peak compared to the straight channel, indicating a more intense heat transfer near the entrance. The zigzag channel exhibits significant fluctuations in the heat transfer coefficient along its length, while the straight channel shows a more gradual decrease with smaller fluctuations. The higher initial peak and subsequent fluctuations in the zigzag channel suggest a more complex flow and potentially enhanced mixing from the bend, leading to better overall heat transfer performance compared to the straight channel.

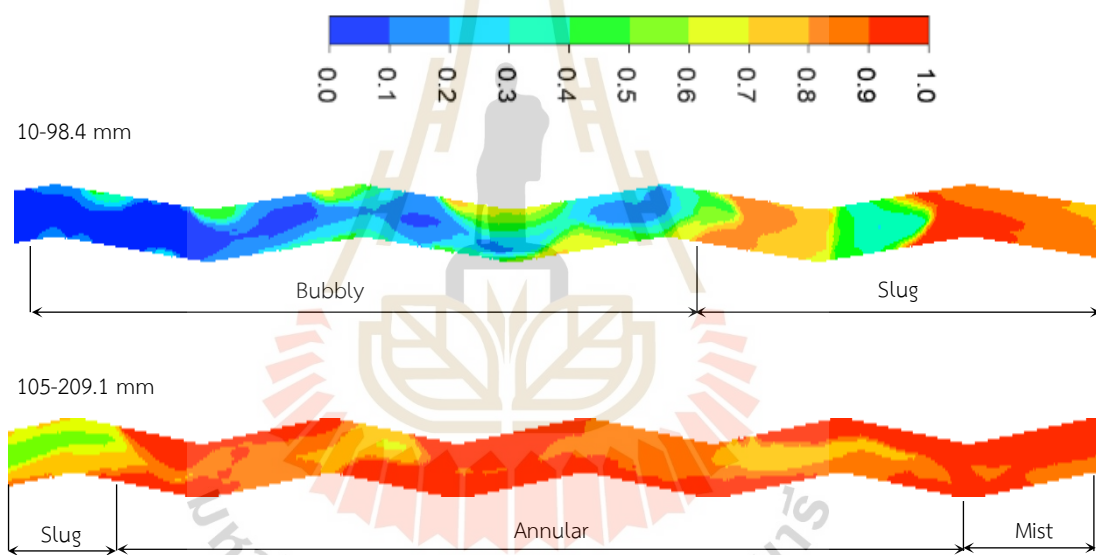
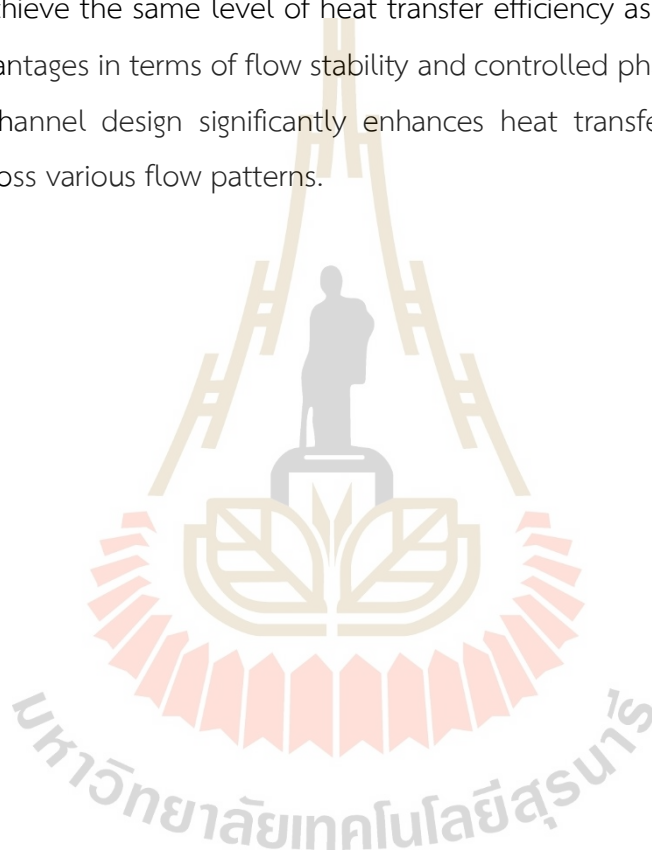


Figure 5.14 Different flow pattern in zigzag channel with corresponding vapor quality (a number of 0 represents the liquid phase, while a number of 1 corresponds to the fully vapor phase).

As shown in figure 5.13, the vapor phase fraction for the straight channel increases more gradually along along the flow. The zigzag channel shows a more rapid increase in α_g early on, indicating faster phase change processes. The final vapor phase fraction is slightly higher in the zigzag channel, suggesting a more efficient phase change process overall.

Figure 5.14 shows schematics of axial variations of flow pattern along a zigzag channel. Flow patterns were found to be similar for nuclear flow characteristics. The zigzag channel continuously disrupts the flow, enhancing turbulence and mixing, which improves heat transfer in all flow patterns. However, the flow patterns of straight channel in figure 5.11 typically differ from those in a zigzag channel due to the absence of bends that induce additional turbulence and mixing. The straight channel design offers more stable and controlled flow patterns compared to the zigzag channel. While it may not achieve the same level of heat transfer efficiency as the zigzag channel, it provides advantages in terms of flow stability and controlled phase change processes. The zigzag channel design significantly enhances heat transfer and phase change efficiency across various flow patterns.



CHAPTER VI

CONCLUSION AND RECOMMENDATION

6.1 Conclusion

This study explored the optimization of zigzag channel configurations and evaporation parameters within minichannel PCHEs, a critical aspect for enhancing thermal and hydraulic performance in cryogenic applications. The key findings and major conclusions of the current research are summarized as follows:

(1) Bending Angles: Increasing the bending angle generally improved heat exchanger effectiveness across various Reynolds numbers. Specifically, 6° and 9° bending angles yielded the best heat transfer performance, with the 6° angle showing notable improvements in high-flow conditions. The bending angle influenced flow characteristics such as velocity distribution and boundary layer behavior, which enhanced heat transfer through improved fluid mixing and core displacement.

(2) Dimensionless Bending Number (β): The introduction of the dimensionless bending number (β) provided a new metric for evaluating zigzag channel performance. Optimal performance was observed at β values around 0.5. Correlations for friction and Nusselt numbers were developed for β values ranging from 0.257 to 3.075, with Fanning friction factor predictions within $\pm 13\%$ for cold side channels and $\pm 10\%$ for hot side channels. Nusselt number correlations had maximum relative errors of $\pm 10\%$ for cold side channels and $\pm 12\%$ for hot side channels.

(3) Methane Evaporation: The study assessed methane evaporation in PCHE minichannels with semicircular diameters of 0.884 mm and lengths of 210 mm, focusing on varying inlet cryogenic temperatures (100–128.9 K) and pressures (0.1 to 1 MPa). Pressure significantly impacted methane evaporation, with nucleate boiling dominating at 0.1 MPa and convective boiling occurring at higher pressures (0.7 to 1 MPa). Optimal cooling efficiency was achieved with low inlet temperatures (100 K) and low

(4) pressure (0.1 MPa), resulting in a temperature difference of 65.4 K. This study also evaluated the effect of semicircular channel diameter (0.884 mm – 3mm), finding that larger diameters improved vapor fraction and heat transfer. Additionally, the zigzag channel design was more effective than straight channels in enhancing heat transfer and phase change efficiency.

6.2 Recommendation

The thermal-hydraulic performance of a minichannels PCHE plays a crucial role in liquefaction and vaporization processes within the energy sector and diverse industrial applications, serving as a pivotal component in the secure treatment of cryogenic fluids. Computational fluid dynamics (CFD) simulation will be needed to do systematic analysis for the development of thermal hydraulic performance PCHEs in cryogenic applications. Recommended future work can be summarized as follows:

(1) The current research is improved the performance of zigzag channel for the conditions with Reynolds number below 2000, a constant $Pr=0.66$, and a fixed channel pitch length. The performance functional forms of zigzag channel PCHEs are also necessary to discuss more, including high Re , variable Pr and β , and some importance of independent variables parameters.

(2) Design considerations should focus on maintaining lower inlet temperatures and pressures to optimize the cooling performance of methane cryogenic systems. For complete evaporation, the influence of multiple factors is required to consider such as bubble constraints, channel shape, and structural parameter effects. This multiple factors are a crucial role in the phase transition flow and heat transfer mechanisms, as well as various flow instabilities.

REFERENCES

- Anurjew, E., Hansjosten, E., Maikowske, S., Schygulla, U., & Brandner, J. J. (2011). Microstructure devices for water evaporation. *Applied Thermal Engineering*, 31(5), 602-609. <https://doi.org/10.1016/j.applthermaleng.2010.05.009>
- Argyropoulos, C. D., & Markatos, N. C. (2015). Recent advances on the numerical modelling of turbulent flows. *Applied Mathematical Modelling*, 39(2), 693-732. <https://doi.org/10.1016/j.apm.2014.07.001>
- Aye, N. N., Hemsuwan, W., Uangpairoj, P., & Thumthae, C. (2023). Numerical Investigation of Zigzag Bending-Angle Channel Effects on Thermal Hydraulic Performance of Printed Circuit Heat Exchanger. *Journal of Thermal Science*, 33(1), 56-69. <https://doi.org/10.1007/s11630-023-1911-y>
- Baek, S., Lee, C., & Jeong, S. (2014). Investigation of two-phase heat transfer coefficients of argon–freon cryogenic mixed refrigerants. *Cryogenics*, 64, 29-39. <https://doi.org/10.1016/j.cryogenics.2014.09.004>
- Biro, F. (2021). WorldEnergyOutlook2021. www.iea.org/weo.
- Brackbill, J. U., Kothe, D. B., & Zemach, C. (1992). A continuum method for modeling surface tension. *Journal of Computational Physics*, 100, 335–354.
- Cai, W.-H., Li, Y., Li, Q., Wang, Y., & Chen, J. (2022). Numerical investigation on thermal–hydraulic performance of supercritical LNG in a Zigzag mini-channel of printed circuit heat exchanger. *Applied Thermal Engineering*, 214. <https://doi.org/10.1016/j.applthermaleng.2022.118760>
- Cengel, Y. A., & Ghajar, A. J. (2020). *Heat and mass transfer fundamentals and applications*.
- Chen, M., Sun, X., & Christensen, R. N. (2015). Fabrication and testing of a high-temperature printed circuit heat exchanger. *16th International Topical Meeting on Nuclear Reactor Thermal Hydraulics (NURETH-16)*.

- Chen, M., Sun, X., & Christensen, R. N. (2019). Thermal-hydraulic performance of printed circuit heat exchangers with zigzag flow channels. *International Journal of Heat and Mass Transfer*, *130*, 356-367. <https://doi.org/10.1016/j.ijheatmasstransfer.2018.10.031>
- Chen, M., Sun, X., Christensen, R. N., Skavdahl, I., Utgikar, V., & Sabharwall, P. (2016). Pressure drop and heat transfer characteristics of a high-temperature printed circuit heat exchanger. *Applied Thermal Engineering*, *108*, 1409-1417. <https://doi.org/10.1016/j.applthermaleng.2016.07.149>
- Cheng, K., Zhou, J., Zhang, H., Huai, X., & Guo, J. (2020). Experimental investigation of thermal-hydraulic characteristics of a printed circuit heat exchanger used as a pre-cooler for the supercritical CO₂ Brayton cycle. *Applied Thermal Engineering*, *171*. <https://doi.org/10.1016/j.applthermaleng.2020.115116>
- Chu, W.-x., Li, X.-h., Ma, T., Chen, Y.-t., & Wang, Q.-w. (2017). Experimental investigation on SCO₂-water heat transfer characteristics in a printed circuit heat exchanger with straight channels. *International Journal of Heat and Mass Transfer*, *113*, 184-194. <https://doi.org/10.1016/j.ijheatmasstransfer.2017.05.059>
- Cong, T., Wang, Z., Zhang, R., Wang, B., & Zhu, Y. (2021). Thermal-hydraulic performance of a PCHE with sodium and sCO₂ as working fluids. *Annals of Nuclear Energy*, *157*. <https://doi.org/10.1016/j.anucene.2021.108210>
- Da Riva, E., Del Col, D., Garimella, S. V., & Cavallini, A. (2012). The importance of turbulence during condensation in a horizontal circular minichannel. *International Journal of Heat and Mass Transfer*, *55*(13-14), 3470-3481. <https://doi.org/10.1016/j.ijheatmasstransfer.2012.02.026>
- Ebadian, M. A., & Lin, C. X. (2011). A Review of High-Heat-Flux Heat Removal Technologies. *Journal of Heat Transfer*, *133*(11). <https://doi.org/10.1115/1.4004340>
- Goto, T., Jige, D., Inoue, N., & Sagawa, K. (2023). Condensation flow visualization, heat transfer, and pressure drop in printed circuit heat exchangers with straight and wavy microchannels. *International Journal of Refrigeration*, *152*, 234-240. <https://doi.org/10.1016/j.ijrefrig.2023.05.002>

- Han, C.-L., Ren, J.-J., Wang, Y.-Q., Dong, W.-P., & Bi, M.-S. (2017). Experimental investigation on fluid flow and heat transfer characteristics of a submerged combustion vaporizer. *Applied Thermal Engineering*, 113, 529-536. <https://doi.org/10.1016/j.applthermaleng.2016.11.075>
- Hasanpour, B., Irandoost, M. S., Hassani, M., & Kouhikamali, R. (2018). Numerical investigation of saturated upward flow boiling of water in a vertical tube using VOF model: effect of different boundary conditions. *Heat and Mass Transfer*, 54(7), 1925-1936. <https://doi.org/10.1007/s00231-018-2289-3>
- Hesselgreaves, J. E. (2001). *Compact heat exchangers: selection, design and operation*.
- Hong, H., Yeom, E., Ji, H. S., Kim, H. D., & Kim, K. C. (2017). Characteristics of pulsatile flows in curved stenosed channels. *PLoS One*, 12(10), e0186300. <https://doi.org/10.1371/journal.pone.0186300>
- Hu, H., Li, J., Xie, Y., & Chen, Y. (2021). Experimental investigation on heat transfer characteristics of flow boiling in zigzag channels of printed circuit heat exchangers. *International Journal of Heat and Mass Transfer*, 165. <https://doi.org/10.1016/j.ijheatmasstransfer.2020.120712>
- Hu, H., Li, Y., & Li, J. (2023). Experimental investigation on flow boiling characteristics in zigzag channels under different sloshing conditions. *Applied Thermal Engineering*, 230. <https://doi.org/10.1016/j.applthermaleng.2023.120780>
- Huang, C., Cai, W., Wang, Y., Liu, Y., Li, Q., & Li, B. (2019). Review on the characteristics of flow and heat transfer in printed circuit heat exchangers. *Applied Thermal Engineering*, 153, 190-205. <https://doi.org/10.1016/j.applthermaleng.2019.02.131>
- Jin, F., Chen, D., Hu, L., Huang, Y., & Bu, S. (2022a). Optimization of zigzag parameters in printed circuit heat exchanger for supercritical CO₂ Brayton cycle based on multi-objective genetic algorithm. *Energy Conversion and Management*, 270. <https://doi.org/10.1016/j.enconman.2022.116243>
- Jin, F., Chen, D., Hu, L., Huang, Y., & Bu, S. (2022b). Study on thermal-hydraulic characteristics of CO₂-water printed circuit heat exchanger with different structural parameters. *Thermal Science and Engineering Progress*, 34. <https://doi.org/10.1016/j.tsep.2022.101430>

- Khan, M. S., Lee, S., Hasan, M., & Lee, M. (2014). Process knowledge based opportunistic optimization of the N₂-CO₂ expander cycle for the economic development of stranded offshore fields. *Journal of Natural Gas Science and Engineering*, *18*, 263-273. <https://doi.org/10.1016/j.jngse.2014.03.004>
- Khan, M. Z. U., Younis, M. Y., Akram, N., Akbar, B., Rajput, U. A., Bhutta, R. A.,...Zahid, F. B. (2021). Investigation of heat transfer in wavy and dual wavy micro-channel heat sink using alumina nanoparticles. *Case Studies in Thermal Engineering*, *28*. <https://doi.org/10.1016/j.csite.2021.101515>
- Kim, D. E., Kim, M. H., Cha, J. E., & Kim, S. O. (2008). Numerical investigation on thermal-hydraulic performance of new printed circuit heat exchanger model. *Nuclear Engineering and Design*, *238*(12), 3269-3276. <https://doi.org/10.1016/j.nucengdes.2008.08.002>
- Kim, I. H., & No, H. C. (2011). Thermal hydraulic performance analysis of a printed circuit heat exchanger using a helium-water test loop and numerical simulations. *Applied Thermal Engineering*, *31*(17-18), 4064-4073. <https://doi.org/10.1016/j.applthermaleng.2011.08.012>
- Kim, I. H., & No, H. C. (2013). Thermal-hydraulic physical models for a Printed Circuit Heat Exchanger covering He, He-CO₂ mixture, and water fluids using experimental data and CFD. *Experimental Thermal and Fluid Science*, *48*, 213-221. <https://doi.org/10.1016/j.expthermflusci.2013.03.003>
- Kim, I. H., No, H. C., Lee, J. I., & Jeon, B. G. (2009). Thermal hydraulic performance analysis of the printed circuit heat exchanger using a helium test facility and CFD simulations. *Nuclear Engineering and Design*, *239*(11), 2399-2408. <https://doi.org/10.1016/j.nucengdes.2009.07.005>
- Kim, S.-M., & Mudawar, I. (2014). Review of databases and predictive methods for heat transfer in condensing and boiling mini/micro-channel flows. *International Journal of Heat and Mass Transfer*, *77*, 627-652. <https://doi.org/10.1016/j.ijheatmasstransfer.2014.05.036>

- Kim, T. H., Kwon, J. G., Yoon, S. H., Park, H. S., Kim, M. H., & Cha, J. E. (2015). Numerical analysis of air-foil shaped fin performance in printed circuit heat exchanger in a supercritical carbon dioxide power cycle. *Nuclear Engineering and Design*, *288*, 110-118. <https://doi.org/10.1016/j.nucengdes.2015.03.013>
- Koku, O., Perry, S., & Kim, J.-K. (2014). Techno-economic evaluation for the heat integration of vaporisation cold energy in natural gas processing. *Applied Energy*, *114*, 250-261. <https://doi.org/10.1016/j.apenergy.2013.09.066>
- Lee, S.-M., & Kim, K.-Y. (2012). Optimization of zigzag flow channels of a printed circuit heat exchanger for nuclear power plant application. *Journal of Nuclear Science and Technology*, *49*(3), 343-351. <https://doi.org/10.1080/00223131.2012.660012>
- Lee, S.-M., & Kim, K.-Y. (2013). Comparative study on performance of a zigzag printed circuit heat exchanger with various channel shapes and configurations. *Heat and Mass Transfer*, *49*(7), 1021-1028. <https://doi.org/10.1007/s00231-013-1149-4>
- Lee, S. Y., Park, B. G., & Chung, J. T. (2017). Numerical studies on thermal hydraulic performance of zigzag-type printed circuit heat exchanger with inserted straight channels. *Applied Thermal Engineering*, *123*, 1434-1443. <https://doi.org/10.1016/j.applthermaleng.2017.05.198>
- Li, S., Wang, B., Dong, J., & Jiang, Y. (2017). Thermodynamic analysis on the process of regasification of LNG and its application in the cold warehouse. *Thermal Science and Engineering Progress*, *4*, 1-10. <https://doi.org/10.1016/j.tsep.2017.08.001>
- Li, S., Zhao, Z., Zhang, Y., Xu, H., & Zeng, W. (2020). Experimental and Numerical Analysis of Condensation Heat Transfer and Pressure Drop of Refrigerant R22 in Minichannels of a Printed Circuit Heat Exchanger. *Energies*, *13*(24). <https://doi.org/10.3390/en13246589>
- Li, X.-h., Deng, T.-r., Ma, T., Ke, H.-b., & Wang, Q.-w. (2019). A new evaluation method for overall heat transfer performance of supercritical carbon dioxide in a printed circuit heat exchanger. *Energy Conversion and Management*, *193*, 99-105. <https://doi.org/10.1016/j.enconman.2019.04.061>

- Liang, S., Zhang, L., Cui, Z., & Ma, X. (2022). Investigation of spontaneous capillary flow and heat transfer characteristics in parallel microchannels based on phase-field model. *Thermal Science and Engineering Progress*, 36. <https://doi.org/10.1016/j.tsep.2022.101517>
- Lin Yuan-Sheng, J. Q., Xie Yong-Hui. (2019). Numerical investigation on thermal performance and flow characteristics of Z and S shape printed circuit heat exchanger using S-CO₂. *Thermal Science and Engineering Progress*, 23(3), 757-764. <https://doi.org/10.2298/TSCI180620090L>
- Liu, H., Zhang, Y., Yu, P., Xue, J., Zhang, L., & Che, D. (2022). Numerical Investigation on Thermal-Hydraulic Performance of a Printed Circuit Heat Exchanger for Liquid Air Energy Storage System. *Energies*, 15(17). <https://doi.org/10.3390/en15176347>
- Liu, S., Jiao, W., & Wang, H. (2016). Three-dimensional numerical analysis of the coupled heat transfer performance of LNG ambient air vaporizer. *Renewable Energy*, 87, 1105-1112. <https://doi.org/10.1016/j.renene.2015.08.037>
- Liu, S., Liu, M., Liu, R., Guo, R., Huang, Y., Zhu, X.,...Tang, J. (2022). Thermal-hydraulic performance of zigzag channels with Bending number below unity for printed circuit heat exchanger. *Applied Thermal Engineering*, 215. <https://doi.org/10.1016/j.applthermaleng.2022.118989>
- Liu, T.-L., Fu, B.-R., & Pan, C. (2012). Boiling two-phase flow and efficiency of co- and counter-current microchannel heat exchangers with gas heating. *International Journal of Heat and Mass Transfer*, 55(21-22), 6130-6141.
- Manglik, R. M., & Bergles, A. E. (1995). Heat Transfer and Pressure Drop Correlations for the Rectangular Offset Strip Fin Compact Heat Exchanger. *Experimental Thermal and Fluid Science*, 10, 171-180.
- McKeon, B. J., Swanson, C. J., Zagarola, M. V., Donnelly, R. J., & Smits, A. J. (2004). Friction factors for smooth pipe flow. *Journal of Fluid Mechanics*, 511, 41-44. <https://doi.org/10.1017/s0022112004009796>
- Meshram, A., Jaiswal, A. K., Khivsara, S. D., Ortega, J. D., Ho, C., Bapat, R., & Dutta, P. (2016). Modeling and analysis of a printed circuit heat exchanger for supercritical CO₂ power cycle applications. *Applied Thermal Engineering*, 109, 861-870. <https://doi.org/10.1016/j.applthermaleng.2016.05.033>

- Mohammed, H. I., Giddings, D., & Walker, G. S. (2019). CFD multiphase modelling of the acetone condensation and evaporation process in a horizontal circular tube. *International Journal of Heat and Mass Transfer*, *134*, 1159-1170. <https://doi.org/10.1016/j.ijheatmasstransfer.2019.02.062>
- Mylavarapu, S. K. (2011). *Design, Fabrication, Performance Testing, and Modeling of Diffusion Bonded Compact Heat Exchangers in a High-Temperature Helium Test Facility* [The Ohio State University].
- Mylavarapu, S. K., Sun, X., Glosup, R. E., & Christensen, R. N. (2014). Thermal hydraulic performance testing of printed circuit heat exchangers in a high-temperature helium test facility. *Applied Thermal Engineering*, *65*(1-2), 605-614. <https://doi.org/10.1016/j.applthermaleng.2014.01.025>
- Nemati, K., Gao, T., Murray, B. T., & Sammakia, B. (2015). *Experimental characterization of the rear door fans and heat exchanger of a fully-enclosed, hybrid-cooled server cabinet* 2015 31st Thermal Measurement, Modeling & Management Symposium (SEMI-THERM),
- Nikuradse, J. (November 1950). *National advisory committee for aeronautics, Technical memorandum 1292 laws of flow in rough pipes.*
- NIST. (2023). National Institute of Standards and Technology <https://webbook.nist.gov/chemistry/fluid/>.
- Pan, J., Li, R., Lv, T., Wu, G., & Deng, Z. (2016). Thermal performance calculation and analysis of heat transfer tube in super open rack vaporizer. *Applied Thermal Engineering*, *93*, 27-35. <https://doi.org/10.1016/j.applthermaleng.2015.09.047>
- Pan, J., Wang, J., Tang, L., Bai, J., Li, R., Lu, Y., & Wu, G. (2020). Numerical investigation on thermal-hydraulic performance of a printed circuit LNG vaporizer. *Applied Thermal Engineering*, *165*. <https://doi.org/10.1016/j.applthermaleng.2019.114447>
- Peng, Z.-R., Zheng, Q.-Y., Chen, J., Yu, S.-C., & Zhang, X.-R. (2020). Numerical investigation on heat transfer and pressure drop characteristics of coupling transcritical flow and two-phase flow in a printed circuit heat exchanger. *International Journal of Heat and Mass Transfer*, *153*. <https://doi.org/10.1016/j.ijheatmasstransfer.2020.119557>

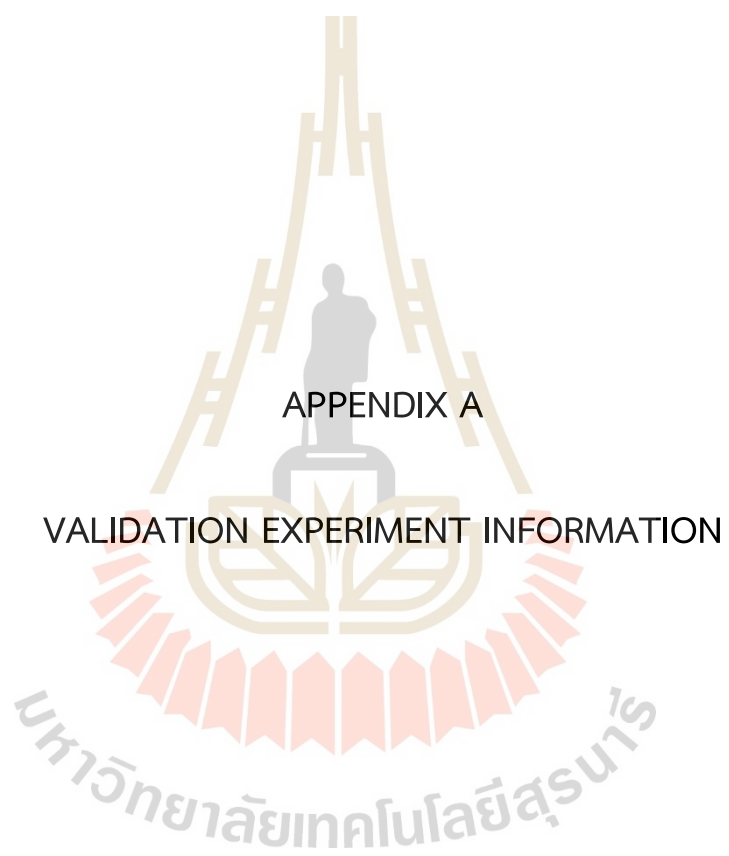
- Pospíšila, J., Charvát, P., Arsenyeva, O., Klimeš, L., Špiláček, M., & Klemeš, J. J. (2019). Energy demand of liquefaction and regasification of natural gas and the potential of LNG for operative thermal energy storage. *Renewable and Sustainable Energy Reviews*, 99, 1–15. <https://doi.org/10.1016/j.rser.2018.09.027>
- Ray, S., & Das, G. (2020). Heat transfer processes in industrial scale. In *Process Equipment and Plant Design* (pp. 19-48). <https://doi.org/10.1016/b978-0-12-814885-3.00002-6>
- Reay, D. A. (2002). Compact heat exchangers, enhancement and heat pumps. *International Journal of Refrigeration*, 25, 460-470.
- Saeed, M., Berrouk, A. S., Salman Siddiqui, M., & Ali Awais, A. (2020). Effect of printed circuit heat exchanger's different designs on the performance of supercritical carbon dioxide Brayton cycle. *Applied Thermal Engineering*, 179. <https://doi.org/10.1016/j.applthermaleng.2020.115758>
- Saeed, M., & Kim, M.-H. (2017). Thermal and hydraulic performance of SCO₂ PCHE with different fin configurations. *Applied Thermal Engineering*, 127, 975-985. <https://doi.org/10.1016/j.applthermaleng.2017.08.113>
- Sarmiento, A. P. C., Milanez, F. H., & Mantelli, M. B. H. (2021). Theoretical models for compact printed circuit heat exchangers with straight semicircular channels. *Applied Thermal Engineering*, 184. <https://doi.org/10.1016/j.applthermaleng.2020.115435>
- Shi, H.-Y., Li, M.-J., Wang, W.-Q., Qiu, Y., & Tao, W.-Q. (2020). Heat transfer and friction of molten salt and supercritical CO₂ flowing in an airfoil channel of a printed circuit heat exchanger. *International Journal of Heat and Mass Transfer*, 150. <https://doi.org/10.1016/j.ijheatmasstransfer.2019.119006>
- Shi, H., Di Miceli Raimondi, N., Fletcher, D. F., Cabassud, M., & Gourdon, C. (2019). Numerical study of heat transfer in square millimetric zigzag channels in the laminar flow regime. *Chemical Engineering and Processing - Process Intensification*, 144. <https://doi.org/10.1016/j.cep.2019.107624>

- Shin, J.-H., & Yoon, S. H. (2020). Thermal and hydraulic performance of a printed circuit heat exchanger using two-phase nitrogen. *Applied Thermal Engineering*, 168. <https://doi.org/10.1016/j.applthermaleng.2019.114802>
- Smithson, C. (2023). *Natural Gas Composition*
- Song, M., Zhengyong, J., Chaobin, D., Yuyan, J., Jun, S., & Xiaoyan, L. (2022). Mathematical modeling investigation on flow boiling and high efficiency heat dissipation of two rectangular radial microchannel heat exchangers. *International Journal of Heat and Mass Transfer*, 190. <https://doi.org/10.1016/j.ijheatmasstransfer.2022.122736>
- Southall, D., & Dewson, S. J. (2010). Innovative compact heat exchangers. *Proceedings of ICAPP '10*.
- SpecialMetals. (2005). INCONEL alloy 617. <https://www.specialmetals.com/documents/technical-bulletins/inconel/inconel-alloy-617.pdf>.
- Tang, L.-H., Yang, B.-H., Pan, J., & Sundén, B. (2021). Thermal Performance Analysis in a Zigzag Channel Printed Circuit Heat Exchanger under Different Conditions. *Heat Transfer Engineering*, 43(7), 567-583. <https://doi.org/10.1080/01457632.2021.1896832>
- Tang, L., Yuan, S., Malin, M., & Parameswaran, S. (2017). Secondary vortex-based analysis of flow characteristics and pressure drop in helically coiled pipe. *Advances in Mechanical Engineering*, 9(4). <https://doi.org/10.1177/1687814017700059>
- Torre, R. d. l., François, J.-L., & Lin, C.-X. (2021). Optimization and heat transfer correlations development of zigzag channel printed circuit heat exchangers with helium fluids at high temperature. *International Journal of Thermal Sciences*, 160. <https://doi.org/10.1016/j.ijthermalsci.2020.106645>
- Torre, R. d. l., François, J.-L., & Lin, C.-X. (2023). Design analysis of a printed circuit heat exchanger for HTGR using a 3D finite elements model. *Nuclear Engineering and Design*, 407. <https://doi.org/10.1016/j.nucengdes.2023.112270>

- Wang, J., Shi, H., Zeng, M., Ma, T., & Wang, Q. (2021). Investigations on thermal–hydraulic performance and entropy generation characteristics of sinusoidal channeled printed circuit LNG vaporizer. *Clean Technologies and Environmental Policy*, 24(1), 95-108. <https://doi.org/10.1007/s10098-021-02084-1>
- Wang, J., Yan, X.-p., Boersma, B. J., Lu, M.-j., & Liu, X. (2023). Numerical investigation on the Thermal-hydraulic performance of the modified channel supercritical CO₂ printed circuit heat exchanger. *Applied Thermal Engineering*, 221. <https://doi.org/10.1016/j.applthermaleng.2022.119678>
- Wang, J., Zhuang, N., Hu, C., Wang, Y., Zhang, Q., Zeng, M.,...Ma, T. (2022). Investigation on flow distribution of supercritical natural gas in a printed circuit heat exchanger. *Cleaner Energy Systems*, 2. <https://doi.org/10.1016/j.cles.2022.100004>
- Wang, L., Chen, M., Shi, S., & Che, D. F. (2017). Multi-objective Optimization of a Printed Circuit Heat Exchanger Design. *Proceedings of the 17th International Topical Meeting on Nuclear Reactor Thermal Hydraulics*.
- Wang, W., & Wu, F. (2017). Exergy destruction analysis of heat exchanger in waste heat recovery system in Kroll process. *International Journal of Exergy*, 22, No.1.
- Xie, L., Zhuang, D., Li, Z., & Ding, G. (2022). Technical Characteristics and Development Trend of Printed Circuit Heat Exchanger Applied in Floating Liquefied Natural Gas. *Frontiers in Energy Research*, 10. <https://doi.org/10.3389/fenrg.2022.885607>
- Yang, Y., Li, H., Yao, M., Gao, W., Zhang, Y., & Zhang, L. (2019). Investigation on the effects of narrowed channel cross-sections on the heat transfer performance of a wavy-channeled PCHE. *International Journal of Heat and Mass Transfer*, 135, 33-43. <https://doi.org/10.1016/j.ijheatmasstransfer.2019.01.044>
- Yih, J., & Wang, H. (2020). Experimental characterization of thermal-hydraulic performance of a microchannel heat exchanger for waste heat recovery. *Energy Conversion and Management*, 204. <https://doi.org/10.1016/j.enconman.2019.112309>

- Yoo, J. W., Nam, C. W., & Yoon, S. H. (2022). Experimental study of propane condensation heat transfer and pressure drop in semicircular channel printed circuit heat exchanger. *International Journal of Heat and Mass Transfer*, 182. <https://doi.org/10.1016/j.ijheatmasstransfer.2021.121939>
- Yoon, S.-J., O'Brien, J., Chen, M., Sabharwall, P., & Sun, X. (2017). Development and validation of Nusselt number and friction factor correlations for laminar flow in semi-circular zigzag channel of printed circuit heat exchanger. *Applied Thermal Engineering*, 123, 1327-1344. <https://doi.org/10.1016/j.applthermaleng.2017.05.135>
- Yoon, S.-J., Sabharwall, P., & Kim, E.-S. (2013). Analytical Study on Thermal and Mechanical Design of Printed Circuit Heat Exchanger. *Idaho National Laboratory Idaho Falls, Idaho 83415*.
- Yoon, S.-J., Sabharwall, P., & Kim, E.-S. (2014). Numerical study on crossflow printed circuit heat exchanger for advanced small modular reactors. *International Journal of Heat and Mass Transfer*, 70, 250-263. <https://doi.org/10.1016/j.ijheatmasstransfer.2013.10.079>
- Zeng, C., Song, Y., Zhou, X., Zhang, F., Chao, M., Jiao, M.,...Gu, H. (2022). Optimization of the thermal-hydraulic performance of zigzag-type microchannel heat exchangers using asymmetric geometry. *Applied Thermal Engineering*, 217. <https://doi.org/10.1016/j.applthermaleng.2022.119216>
- Zhang, H., Guo, J., Huai, X., Cheng, K., & Cui, X. (2019). Studies on the thermal-hydraulic performance of zigzag channel with supercritical pressure CO₂. *The Journal of Supercritical Fluids*, 148, 104-115. <https://doi.org/10.1016/j.supflu.2019.03.003>
- Zhao, Z., Chen, X., Zhang, X., Ma, X., & Yang, S. (2019). Experimental and numerical study on thermal-hydraulic performance of printed circuit heat exchanger for liquefied gas vaporization. *Energy Science & Engineering*, 8(2), 426-440. <https://doi.org/10.1002/ese3.525>
- Zhao, Z., Zhang, Y., Chen, X., Ma, X., Yang, S., & Li, S. (2019). A numerical study on condensation flow and heat transfer of refrigerant in minichannels of printed circuit heat exchanger. *International Journal of Refrigeration*, 102, 96-111. <https://doi.org/10.1016/j.ijrefrig.2019.03.016>

- Zhao, Z., Zhang, Y., Chen, X., Ma, X., Yang, S., & Li, S. (2020). Experimental and numerical investigation of thermal-hydraulic performance of supercritical nitrogen in airfoil fin printed circuit heat exchanger. *Applied Thermal Engineering*, 168. <https://doi.org/10.1016/j.applthermaleng.2019.114829>
- Zhao, Z., Zhou, Y., Ma, X., Chen, X., Li, S., & Yang, S. (2019a). Effect of Different Zigzag Channel Shapes of PCHes on Heat Transfer Performance of Supercritical LNG. *Energies*, 12(11). <https://doi.org/10.3390/en12112085>
- Zhao, Z., Zhou, Y., Ma, X., Chen, X., Li, S., & Yang, S. (2019b). Numerical Study on Thermal Hydraulic Performance of Supercritical LNG in Zigzag-Type Channel PCHes. *Energies*, 12(3). <https://doi.org/10.3390/en12030548>
- Zhou, X., Zhang, S., Li, X., Zuo, J., Wei, J., & Wang, H. (2024). Numerical study on thermal-hydraulic performance of hydrocarbon fuel under trans-critical states and supercritical CO₂ in a zigzag printed circuit heat exchanger. *Applied Thermal Engineering*, 236. <https://doi.org/10.1016/j.applthermaleng.2023.121496>
- Zohuri, B. (2018). *Physics of Cryogenics*. <https://doi.org/https://doi.org/10.1016/C2017-0-01796-2>



APPENDIX A

VALIDATION EXPERIMENT INFORMATION

1. NACA straight circular channel experiment

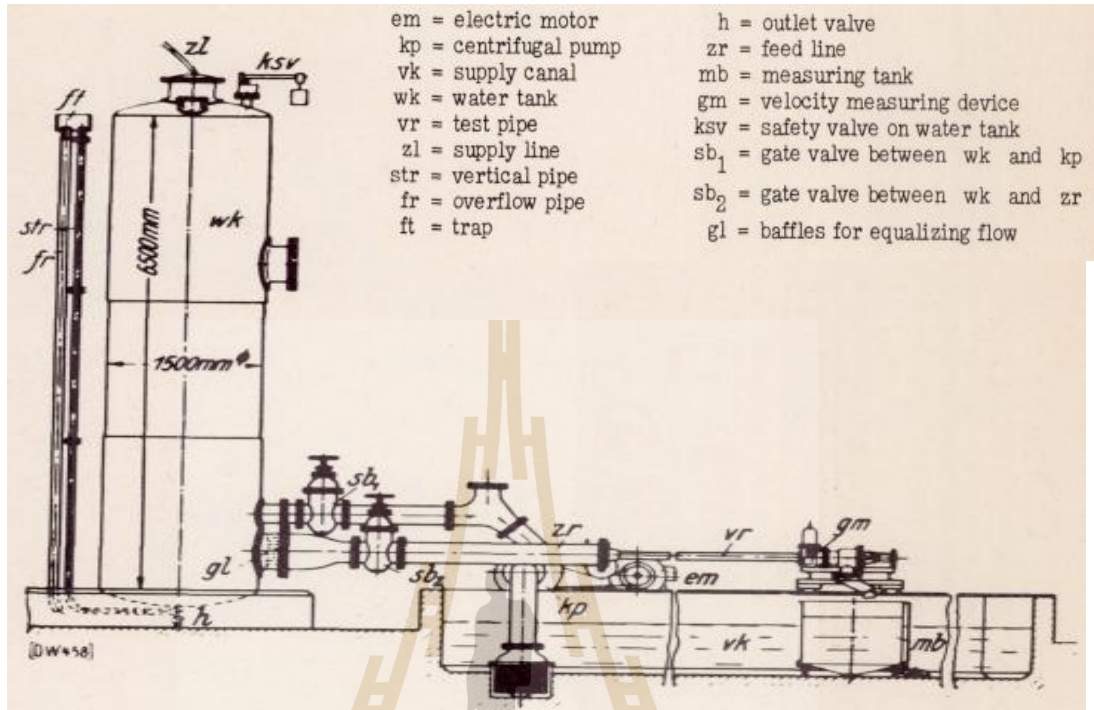


Figure A.1 NACA straight-channel test apparatus (Nikuradse, November 1950).

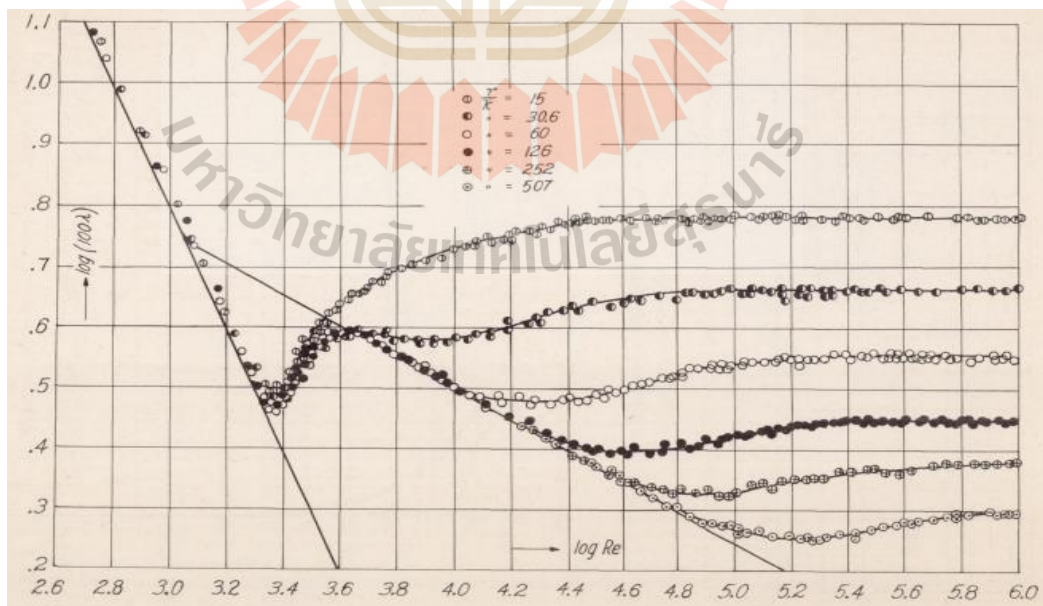


Figure A.2 Relation between $\log(100\lambda)$ and $\log Re$ where r/k = relative roughness, λ = resistance factor (Nikuradse, November 1950).

2. Mylavarapu et al.'s straight semicircular channel PCHE experiment

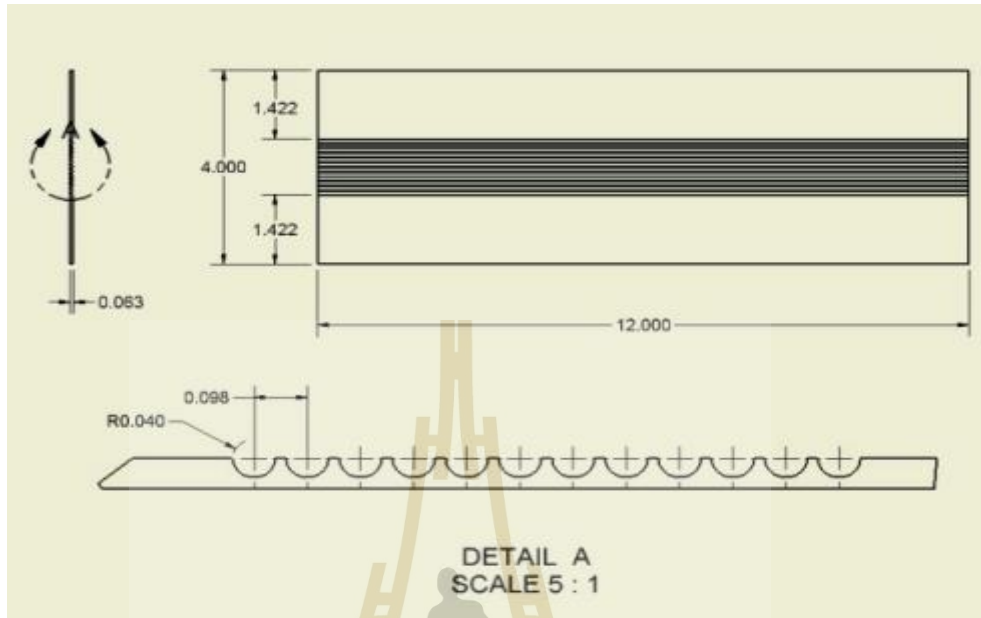


Figure A.3 Geometry of the straight semicircular channel (cold side) plate used in the PCHE design (all dimensions in inches) (Mylavarapu, 2011).

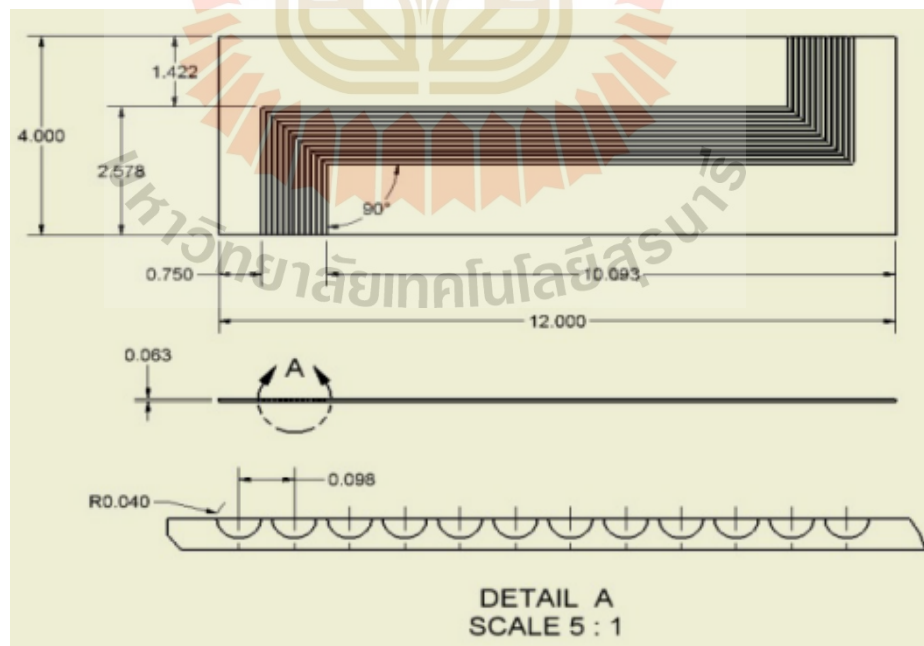


Figure A.4 Geometry of the straight semicircular channel (hot side) plate used in the PCHE design, (all dimensions in inches) (Mylavarapu, 2011)

3. I. H. Kim et al.'s zigzag channel PCHE experiment

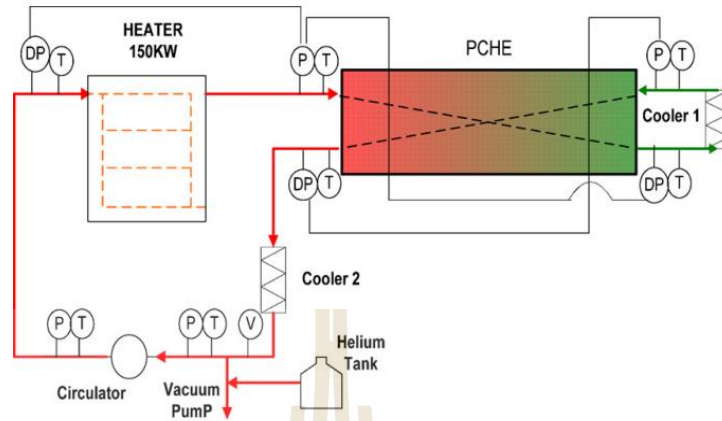


Figure A.5 KAIST helium test loop (Kim et al., 2009).



Figure A.6 The angle of a zigzag channel in PCHE (Kim et al., 2009).

4. Chen et al.'s zigzag channel PCHE experiment

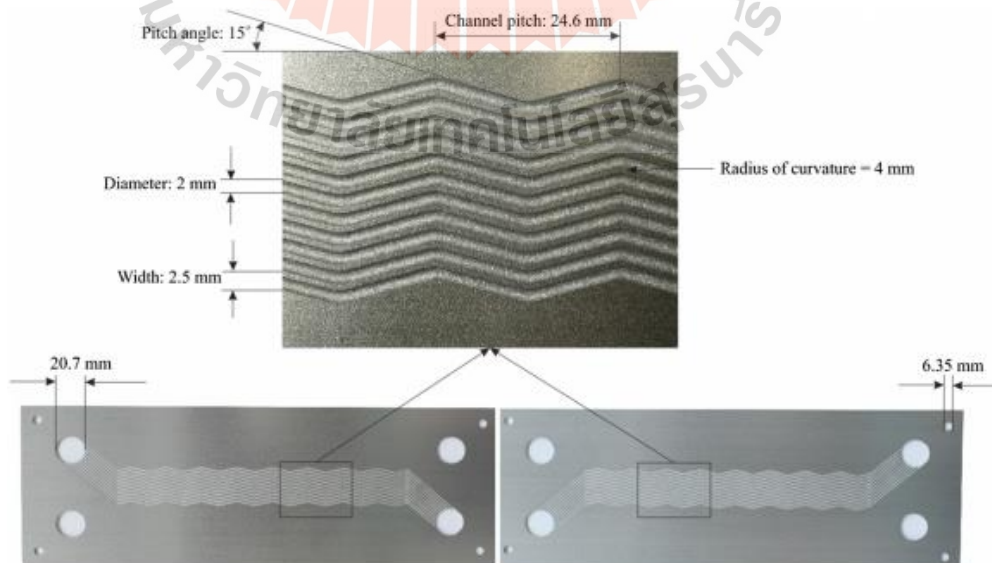


Figure A.7 Images of a section of a hot-side or cold-side plate (Chen et al., 2019).

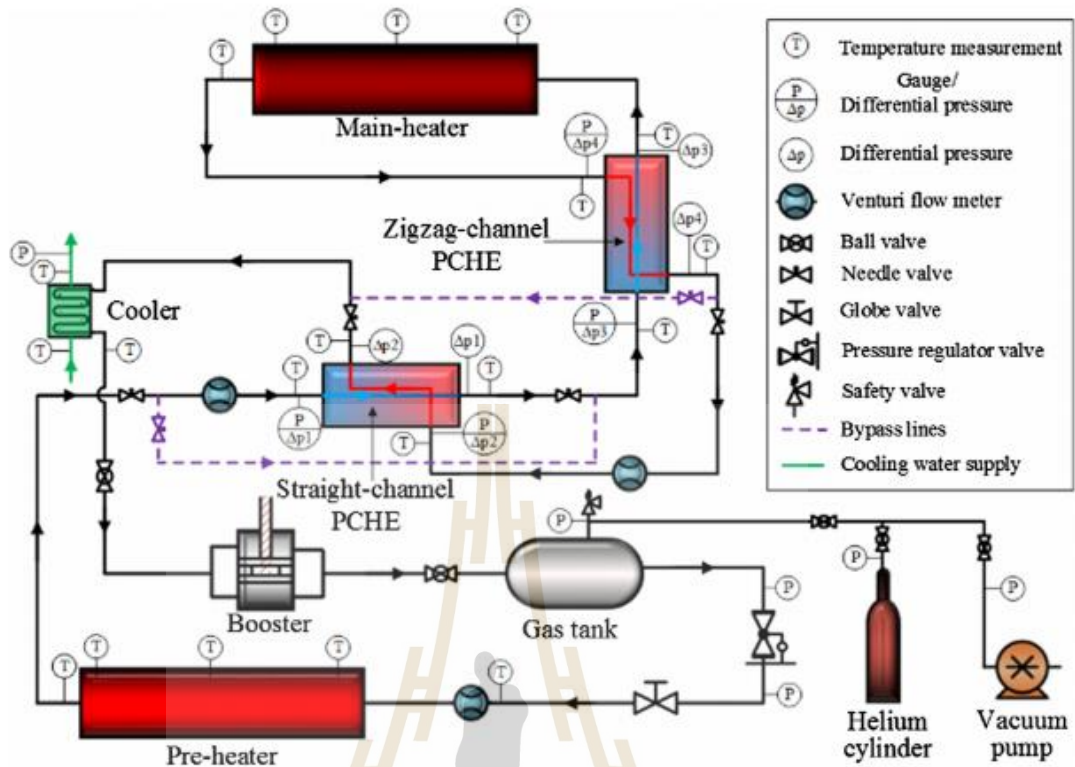


Figure A.8 Layout of the high-temperature helium test facility (Chen et al., 2019).

5. Two-phase nitrogen experiment in the straight semicircular channel PCHE

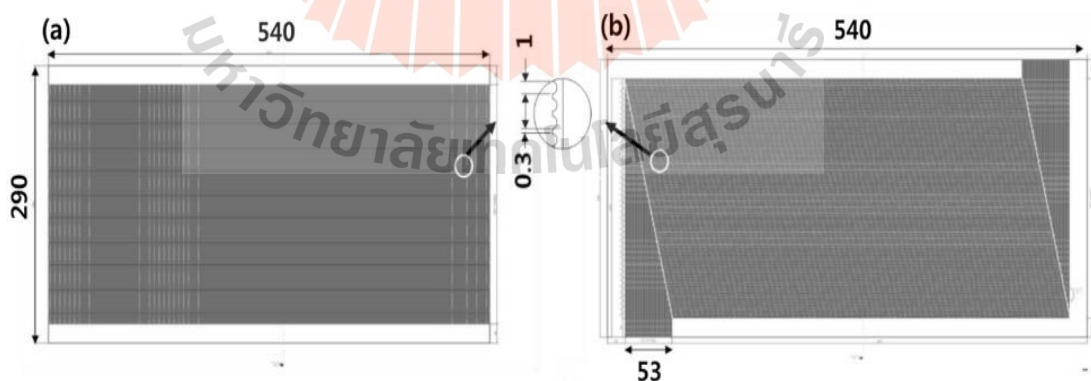


Figure A.9 Design of the heat plates: (a) straight channel design for low pressure used on the hot side, and (b) 'N'-type design for high pressure used on the cold side (numbers are in mm) (Shin & Yoon, 2020).

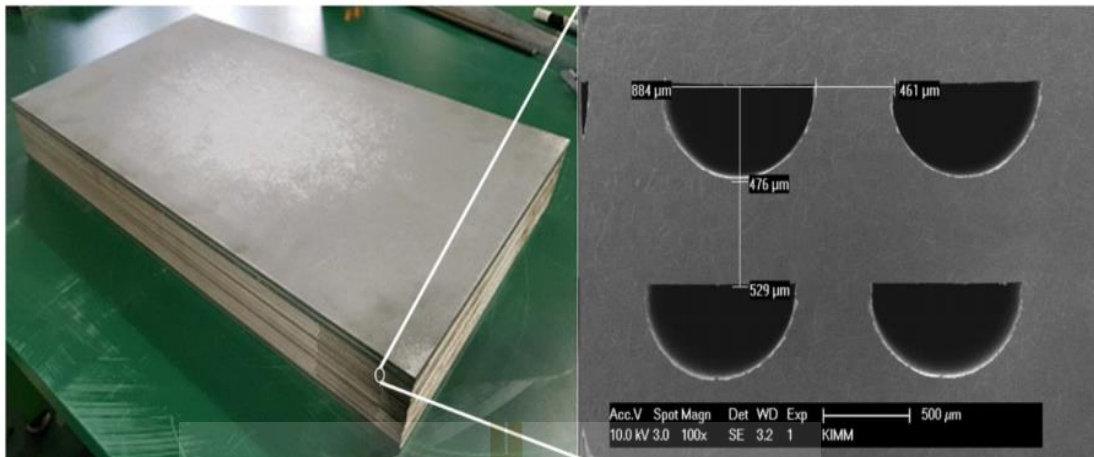


Figure A.10 Diffusion bonded core and scanning electron microscopy image of the cross-section of the PCHE core (Shin & Yoon, 2020).

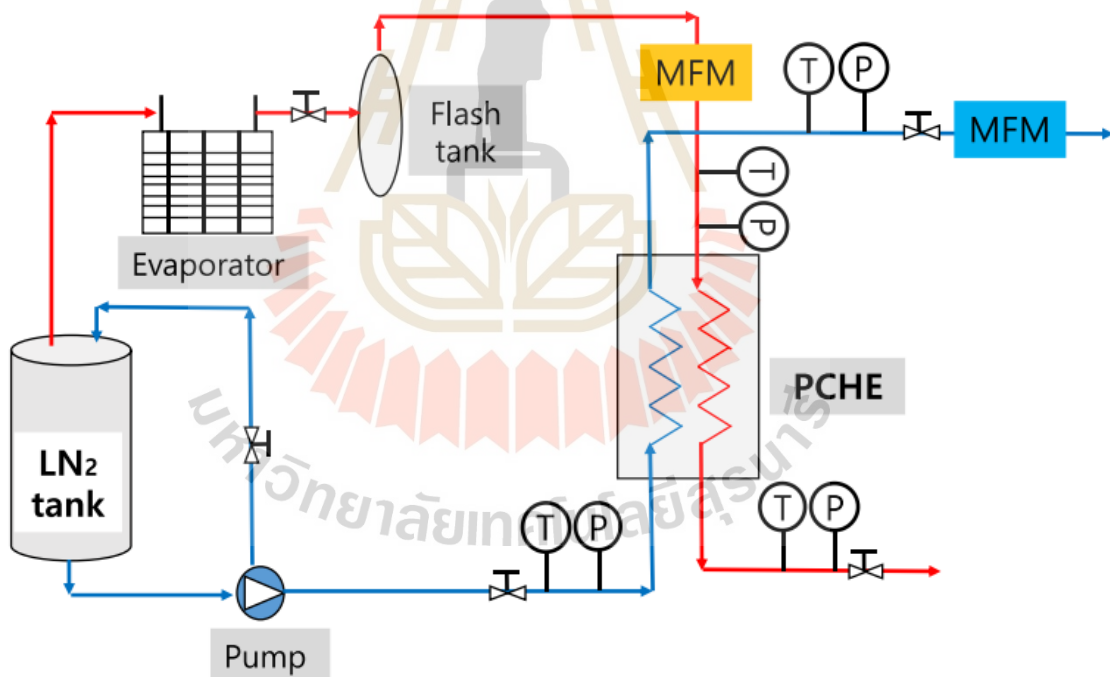
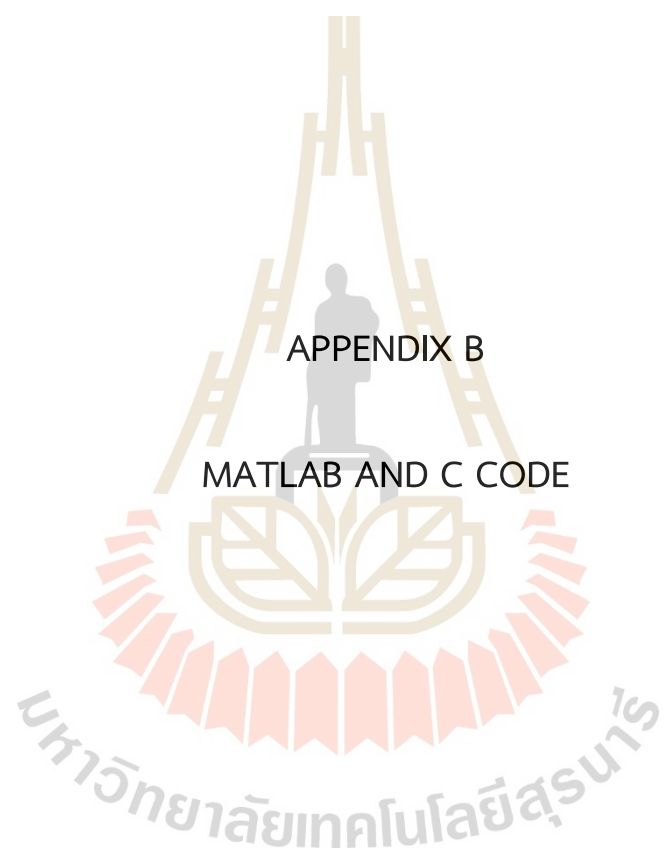


Figure A.11 Schematic of the two-phase nitrogen experimental set-up (Shin & Yoon, 2020).



APPENDIX B

MATLAB AND C CODE

Matlab Code for Nonlinear Regression

% Define the equation

```
fun = @(A, Re, p) (A(1) * Re.^A(2) * 0.66^A(3) * p.^A(4) + 15.78) ./ Re;
```

% Given data

```
Re = [477.6285708 682.3265298 818.7918357 1091.722448 1228.187754 1364.65306];
```

```
f = [0.034031009 0.027171356 0.024289158 0.020185535 0.018653694  
0.01799412];
```

```
p = 0.157079633;
```

% Set the initial guess for A1, A2, A3, A4, A5

```
A0 = [1, 1, 1, 0.1];
```

% Define the lower and upper bounds for A1, A2, A3, A4, A5

```
lb = [0, 0, 0]; % Lower bounds
```

```
ub = [Inf, 2000, 0.523598776]; % Upper bounds
```

% Set optimization options

```
options = optimoptions('fmincon', 'MaxFunctionEvaluations', 1e04, 'TolFun', 1e-06);
```

% Perform nonlinear regression with constraints

```
A = fmincon(@(A) norm(fun(A, Re, p) - f), A0, [], [], [], [], lb, ub, [], options);
```

% Extract the optimized constants

```
A1 = A(1);
```

```
A2 = A(2);
```

```
A3 = A(3);
```

```
A4 = A(4);
```

```
% Calculate the predicted values of Nu using the optimized constants
predicted_Nu = fun(A, Re, p);

% Calculate the residuals
residuals = f - predicted_Nu;

% Calculate the total sum of squares
total_sum_squares = sum((f - mean(f)).^2);

% Calculate the residual sum of squares
residual_sum_squares = sum(residuals.^2);

% Calculate the number of predictors
num_predictors = numel(A) - 1; % Exclude the intercept term

% Calculate the number of observations
num_observations = numel(f);

% Calculate the R-squared value
r_squared = 1 - (residual_sum_squares / total_sum_squares);

% Calculate the adjusted R-squared value
adjusted_r_squared = 1 - ((1 - r_squared) * (num_observations - 1) /
(num_observations - num_predictors - 1));

% Display the optimized constants
disp(['A1: ', num2str(A1)]);
disp(['A2: ', num2str(A2)]);
disp(['A3: ', num2str(A3)]);
disp(['A4: ', num2str(A4)]);
```

```
% Display the R-squared and adjusted R-squared values
disp(['R-squared: ', num2str(r_squared)]);
disp(['Adjusted R-squared: ', num2str(adjusted_r_squared)]);
```

```
% Plot the actual data
scatter(Re, f, 'b', 'Marker', 'o');
hold on;
```

```
% Plot the predicted data
scatter(Re, predicted_Nu, 'r', 'Marker', 'x');
```

```
% Add labels and legend
xlabel('Re');
ylabel('f');
legend('Actual', 'Predicted');
```

```
% Add a title
title('Regression Analysis');
```

```
% Show the plot
hold off;
```

Matlab Code for Interior-point method

```
% Read the data from the Excel file
data = readtable('data3-No3.xlsx');
```

```
% Extract data into variables
Re = data.Re;
beta = data.beta;
bending_angle = data.bending_angle;
f = data.values;
```

```

rb_Dh = data.rb_Dh;

% Check for NaN values in the data and remove them
validIdx = ~isnan(Re) & ~isnan(beta) & ~isnan(bending_angle) & ~isnan(f) &
~isnan(rb_Dh);
Re = Re(validIdx);
beta = beta(validIdx);
bending_angle = bending_angle(validIdx);
f = f(validIdx);
rb_Dh = rb_Dh(validIdx);

% Define the model function based on the provided formulation
modelfun = @(C, x) (C(1) * x(:,1) .* x(:,2).^C(2) .* x(:,3).^C(3) .* (x(:,4)).^C(4) + C(5) *
x(:,3).^C(6))./x(:,1);

% Custom objective function for optimization
objFun = @(C) sum((f - modelfun(C, [Re, beta, bending_angle, rb_Dh])).^2);

% Initial parameter estimates [C1, C2, C3, C4, C5, C6]
C0 = [0.0611, 0.0775, 0.3872, -0.2972, 0.0053, 0.0000]; % Example initial guesses
based on your previous results

% Define the bounds for the parameters
lb = [-Inf, -10, -10, -10, -10, -Inf]; % Lower bounds for [C1, C2, C3, C4, C5, C6]
ub = [Inf, 10, 10, 10, 10, Inf];      % Upper bounds for [C1, C2, C3, C4, C5, C6]

% Set up the optimization options for fmincon
options = optimoptions('fmincon', 'Algorithm', 'interior-point',
'MaxFunctionEvaluations', 10000, 'Display', 'iter', 'OptimalityTolerance', 1e-8);

% Ensure valid initial guess and bounds

```

```

validInitialGuess = all(isfinite(modelfun(C0, [Re, beta, bending_angle, rb_Dh])));
if ~validInitialGuess
    error('Invalid initial guess: initial parameter estimates lead to undefined values.');
```

end

```

% Use fmincon for optimization
[C_opt, ~, exitflag, output] = fmincon(@(C) objFun(C), C0, [], [], [], [], lb, ub, [], options);

% Check if the optimized parameters lead to valid outputs
if ~all(isfinite(modelfun(C_opt, [Re, beta, bending_angle, rb_Dh])))
    error('Optimization failed: optimized parameters lead to undefined values.');
```

end

```

% Display the optimized parameters
disp('Optimized parameters:');
disp(['C1: ', num2str(C_opt(1))]);
disp(['C2: ', num2str(C_opt(2))]);
disp(['C3: ', num2str(C_opt(3))]);
disp(['C4: ', num2str(C_opt(4))]);
disp(['C5: ', num2str(C_opt(5))]);
disp(['C6: ', num2str(C_opt(6))]);

% Display exit flag and output details
disp('Exit flag:');
disp(exitflag);
disp('Optimization output:');
disp(output);

% Use optimized parameters to predict values
predicted_values = modelfun(C_opt, [Re, beta, bending_angle, rb_Dh]);
```

```

% Calculate R-squared value
SSres = sum((f - predicted_values).^2);
SStot = sum((f - mean(f)).^2);
R_squared = 1 - SSres / SStot;

% Display R-squared value
disp(['R-squared value: ', num2str(R_squared)]);

% Plot the observed vs. predicted values
figure;
scatter(f, predicted_values, 'filled');
hold on;
plot(f, f, 'r--'); % Identity line
xlabel('Observed Values');
ylabel('Predicted Values');
title(['Observed vs. Predicted Values (R^2 = ' num2str(R_squared) ')]);
legend('Predicted vs. Observed', 'Identity Line', 'Location', 'northwest');
grid on;
hold off;

% Plot the residuals
figure;
residuals = f - predicted_values;
scatter(predicted_values, residuals, 'filled');
xlabel('Predicted Values');
ylabel('Residuals');
title('Residuals vs. Predicted Values');
grid on;

% Calculate relative error
relative_error = (f - predicted_values) .* 100 ./ f;

```

```

% Display summary statistics of relative error
mean_relative_error = mean(relative_error);
median_relative_error = median(relative_error);
max_relative_error = max(relative_error);
min_relative_error = min(relative_error);

disp('Summary statistics of relative error:');
disp(['Mean Relative Error: ', num2str(mean_relative_error)]);
disp(['Median Relative Error: ', num2str(median_relative_error)]);
disp(['Max Relative Error: ', num2str(max_relative_error)]);
disp(['Min Relative Error: ', num2str(min_relative_error)]);

% Plot relative error
figure;
scatter(f, relative_error, 'filled');
xlabel('Observed Values');
ylabel('Relative Error');
title('Relative Error vs. Observed Values');
grid on;

% Perform K-fold cross-validation
k = 5; % Number of folds
cv = cvpartition(size(Re, 1), 'KFold', k);
mse = zeros(k, 1);
for i = 1:k
    trainIdx = cv.training(i);
    testIdx = cv.test(i);
    % Update data for the current fold
    Re_train = Re(trainIdx);
    beta_train = beta(trainIdx);
    bending_angle_train = bending_angle(trainIdx);

```

```

rb_Dh_train = rb_Dh(trainIdx);
values_train = f(trainIdx);

% Re-optimize parameters on the training set
[C_temp, ~, ~, ~] = fmincon(@(C) objFun(C), C_opt, [], [], [], [], lb, ub, [], options);

% Predict values on the test set
predicted_values_test = modelfun(C_temp, [Re(testIdx), beta(testIdx),
bending_angle(testIdx), rb_Dh(testIdx)]);

% Compute Mean Squared Error for this fold
mse(i) = mean((f(testIdx) - predicted_values_test).^2);
end
disp(['Cross-validated MSE: ', num2str(mean(mse))]);

% Perform sensitivity analysis (example)
% Evaluate the model's response to changes in each parameter
delta = 1; % Perturbation size for sensitivity analysis
sensitivity = zeros(1, 6);
for j = 1:6
    C_temp = C_opt;
    C_temp(j) = C_opt(j) * (1 + delta);
    predicted_values_temp = modelfun(C_temp, [Re, beta, bending_angle, rb_Dh]);
    sensitivity(j) = mean(abs(predicted_values_temp - predicted_values));
end
disp('Sensitivity of the model parameters:');
disp(['Sensitivity to C1: ', num2str(sensitivity(1))]);
disp(['Sensitivity to C2: ', num2str(sensitivity(2))]);
disp(['Sensitivity to C3: ', num2str(sensitivity(3))]);
disp(['Sensitivity to C4: ', num2str(sensitivity(4))]);
disp(['Sensitivity to C5: ', num2str(sensitivity(5))]);

```

```
disp(['Sensitivity to C6: ', num2str(sensitivity(6))]);
```

C Code for User Define Function (UDF)

```
#include "udf.h"
#include "sg_mphase.h"
#define T_SAT 108.6
#define LAT_HT 138682

DEFINE_SOURCE(vap_src, cell, pri_th, dS, eqn)
{
  Thread *mix_th, *sec_th;
  real m_dot_v;
  mix_th = THREAD_SUPER_THREAD(pri_th);
  sec_th = THREAD_SUB_THREAD(mix_th, 1);
  /*m_dot_v=0.*/
  if(C_T(cell, mix_th)>=T_SAT)
  {
    m_dot_v = 0.1*C_VOF(cell, sec_th)*C_R(cell, sec_th)*fabs(C_T(cell, sec_th) -
    T_SAT)/T_SAT;

    dS[eqn] = 0.;
  }

  if(C_T(cell, mix_th)<=T_SAT)
  {
    m_dot_v = -0.1*C_VOF(cell, pri_th)*C_R(cell, pri_th)*fabs(T_SAT-
    C_T(cell,pri_th))/T_SAT;
    dS[eqn] = -0.1*C_R(cell, pri_th)*fabs(C_T(cell, pri_th) - T_SAT)/T_SAT;
  }
  return m_dot_v ;
}
```

```

}

DEFINE_SOURCE(liq_src, cell, sec_th, dS, eqn)
{
  Thread * mix_th, *pri_th;
  real m_dot_l;
  mix_th = THREAD_SUPER_THREAD(sec_th);
  pri_th = THREAD_SUB_THREAD(mix_th, 0);
  /*m_dot_l=0.*/
  if(C_T(cell, mix_th)>=T_SAT)
  {
    m_dot_l = -0.1*C_VOF(cell, sec_th)*C_R(cell, sec_th)*fabs(C_T(cell, sec_th) -
    T_SAT)/T_SAT;
    dS[eqn] = -0.1*C_R(cell, sec_th)*fabs(C_T(cell, sec_th) - T_SAT)/T_SAT;
  }
  if(C_T(cell, mix_th)<=T_SAT)
  {
    m_dot_l = 0.1*C_VOF(cell, pri_th)*C_R(cell, pri_th)*fabs(T_SAT-C_T(cell,pri_th))/T_SAT;
    dS[eqn] =0.;
  }

  return m_dot_l;
}

```

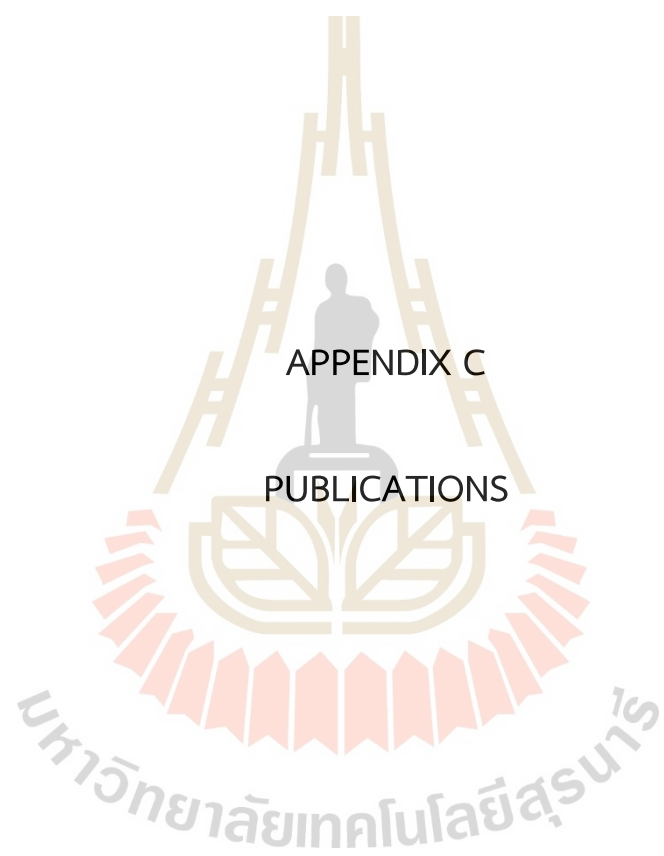
```

DEFINE_SOURCE(enrg_src, cell, mix_th, dS, eqn)
{
  Thread *pri_th, *sec_th;
  real m_dot;
  pri_th = THREAD_SUB_THREAD(mix_th, 0);
  sec_th = THREAD_SUB_THREAD(mix_th, 1);
  if(C_T(cell, mix_th)>=T_SAT)

```

```
{  
m_dot = -0.1*C_VOF(cell, sec_th)*C_R(cell, sec_th)*fabs(C_T(cell, sec_th) -  
T_SAT)/T_SAT;  
dS[eqn] = -0.1*C_VOF(cell, sec_th)*C_R(cell, sec_th)*LAT_HT/T_SAT;  
}  
  
if(C_T(cell, mix_th)<=T_SAT)  
{  
m_dot = 0.1*C_VOF(cell, pri_th)*C_R(cell, pri_th)*fabs(T_SAT-C_T(cell,pri_th))/T_SAT;  
dS[eqn] = 0.1*C_VOF(cell, pri_th)*C_R(cell, pri_th)*LAT_HT/T_SAT;  
}  
return LAT_HT*m_dot; }
```





List of Publications

ARTICALES IN JOURNALS

- Aye, N. N., Hemsuwan, W., Uangpairoj, P., & Thumthae, C. (2023). Numerical Investigation of Zigzag Bending-Angle Channel Effects on Thermal Hydraulic Performance of Printed Circuit Heat Exchanger. *Journal of Thermal Science*, 33(1), 56-69. doi:10.1007/s11630-023-1911-y.
- Aye, N. N., Thumthae, C., & Hemsuwan, W. . (2023). Numerical Study of Channel Structure Effects on Thermal Hydraulic Performance of Printed Circuit Heat Exchanger. *Journal of Research and Applications in Mechanical Engineering*, 11(2), JRAME-23. Retrieved from <https://ph01.tci-thaijo.org/index.php/jrame/article/view/251429>.

ARTICALES IN CONFERENCES

- Aye, N. N., Thumthae, C., (2020). CFD Study on the Flow Over a NREL S826 Airfoil using Turbulence Models. SUT International Virtual Conference on Science and Technology (SUT-IVCST 2020), 28th August, 2020, Suranaree University of Technology, Thailand.
- Aye, N. N., Thumthae, C., & Hemsuwan, W. . (2023). A Numerical Investigation of Evaporation Process in a Minichannel of Printed Circuit Heat Exchanger. The 13th TSME International Conference on Mechanical Engineering, 12th – 15th December 2023, Chiang Mai, Thailand

BIOGRAPHY

Miss Nyein Nyein Aye was born on October 10, 1989 in Yangon province, Myanmar. She graduated Bachelor degree of Mechanical Engineering at Mechanical Department, Technological University (Hmawbi), Myanmar, 2011. She received her Master's degree in Mechanical Engineering from Yangon Technological University, Myanmar, in 2017. In 2019, she received the Office of the Higher Education Commission of Thailand Scholarships (Year 2019) and Vithedbundit Scholarship, Institute of Engineering, Suranaree University of Technology (Thailand) for Ph.D. degree. She studied with the thesis title “Numerical study of printed circuit heat exchanger (PCHE) applying in cryogenic application” under the supervision of Assist. Prof. Dr. Chalothorn Thumthae.

